NONADIABATIC QUANTUM WAVE-PACKET DYNAMICS OF $Cl + H_2$ (HD) REACTION

A Thesis

Submitted for the Degree of

DOCTOR OF PHILOSOPHY

By

SUBHAS GHOSAL

SCHOOL OF CHEMISTRY

UNIVERSITY OF HYDERABAD

HYDERABAD - 500 046

INDIA

March 2007

Contents

Chapter 1

Introduction

Most of the discussions on chemical reaction dynamics starts with the Born-Oppenheimer (BO) adiabatic approximation. The large mass of a nucleus compared to that of an electron permits an approximate separation of the electronic and nuclear motion. This approximation, a classic work of Born and Oppenheimer [1] and later extended by Born and Huang [2], have laid the foundation for the modern theory of electronically adiabatic processes and the nonadiabatic coupling effects. Still today, many chemical process can be rationalized in terms of the nuclear dynamics on a single BO potential energy surface (PES) and without this approximation the introduction of nonadiabatic processes in quantum reaction dynamics will be fairly incomplete.

The examples of nonadiabatic processes are plenty in nature. For example, the isomerization processes of polyatomic molecules, radiationless relaxation of the excited electronic states, photoinduced unimolecular decay, etc. all are guided by nonadiabatic interactions [3]. Many photochemical reactions including some of the most basic processes in photosynthesis [4] and the initiation process of vision are also nonadiabatic in nature [5]. In nonadiabatic processes, the nuclear

dynamics involve more than one BO PES and they cannot be rationalized within the BO approximation. The BO approximation rests on few boundary conditions: (1) the electronic state of the system in question must be well separated from the rest of the states; (2) the rearrangement of the electron cloud should be gradual along with the change of nuclear positions; and (3) the velocities of the nuclei must be sufficiently small to permit the electrons to adjust completely to their motions. But for polyatomic molecules standard BO approximation often fails due to the availability of large number of energetically close-lying electronic states and many nuclear degrees of freedom [6]. In such situations, it is often necessary to monitor the nuclear motions simultaneously on more than one electronic PES.

A typical scenario in polyatomic molecules in this context is the coupling between nuclei and electrons, known as vibronic or electronic coupling. For close-lying electronic states often there is a conical intersection between the electronic states [7–12]. Conical intersections, also called as photochemical funnels [13, 14] serve as the "bottleneck" in many photophysical and photochemical transitions and provide pathways for ultrafast internal conversion dynamics. For open-shell systems, the spin of the unpaired electrons often leads to the so-called spin-orbit (SO) coupling (a weak magnetic interaction of the electronic spin with its orbital motion around the atomic nuclei) [15]. Due to this coupling, the spin degrees of freedom respond to the orbital angular momentum of the molecule and separate the energy of the spin-degenerate states [16]. Apart from this electronic and SO coupling, nonadiabatic effects due to the conically intersecting potential energy surfaces (PESs) represented by the Jahn-Teller (JT) active systems is also well known [17–20]. In this case, the symmetry-enforced electronic degeneracy becomes unstable for nonlinear configurations. Another subclass deals with the interaction between the degenerate and nondegenerate electronic states. These

are referred to as pseudo-Jahn-Teller (PJT) systems in the literature [10, 21–23]. Linear molecules are exceptions of the JT and PJT interactions but instabilities in their degenerate electronic states lead to Renner-Teller (RT) or glancing-type intersections [24, 25].

In an adiabatic electronic representation, the coupling between the electronic states is caused by the off-diagonal nonadiabatic coupling (NAC) elements of the nuclear kinetic energy operator. These NAC elements, which are the derivative of the electronic wavefunction with respect to the nuclear coordinates, are diverging in nature and become singular when two electronic states are degenerate [10]. As a result, both the electronic wavefunction and energy become discontinuous at the seam of CIs making the adiabatic representation unsuitable for dynamical calculations. In order to deal with this situation, one resorts to a diabatic electronic representations in which the coupling between the states are represented by non-singular off-diagonal elements fo the electronic Hamiltonian [26–28]. The NAC terms of the adiabatic representation are therefore transformed to smooth potential energy coupling in the diabatic representation [29]. Various approximate schemes have been proposed for this adiabatic-to-diabatic transformation [30–32]. One of them is through a suitable unitary transformation of the adiabatic electronic states defined in terms of the adiabatic-to-diabatic mixing angle [33]. However, the construction of the diabatic electronic states for a realistic molecular systems is still a challenging problem and different approximate mathematical schemes have been proposed to accomplish this [34].

One generally follows either a time-independent or a time-dependent quantum mechanical approach for the nuclear dynamical simulation. In time-independent method, the time-independent Schrödinger equation (TISE) is solved by representing the nuclear Hamiltonian in a suitable basis.In time-dependent approach,

an initial wave packet (WP) corresponding to the ground vibrational level is prepared which is subject to a Franck-Condon (FC) transition to the final electronic state(s), where it is propagated with the aid of time-dependent Schrödinger equation (TDSE) in an spectroscopic study. In a reactive scattering study, the initial WP is located in the reagent asymptote of the PES and propagated it by solving the TDSE. After the propagation, the dynamical observables are calculated. To calculate the eigenvalue spectrum the time autocorrelation function of the WP in the final electronic state(s) is calculated and Fourier transformed to the energy domain [35, 36]. The reaction attributes are obtained by calculating the reaction probabilities with the aid of a quantum flux operator [37]. the time autocorrelation function to the energy domain [35, 36]. The fingerprints of the ultrafast relaxation dynamics are extracted from the time behavior of the electronic populations and probability density of the nuclear wavefunction.

1.1 Halogen-Hydrogen reactions

The reaction between the halogen atoms (X = F, Cl, Br, I) and the hydrogen molecule, X (^2P) + H_2 → HX + H, have been of fundamental importance in the development of chemical kinetics and the reaction dynamics. In particular, F (^2P) + H_2 [38–52], and Cl (^2P) + H_2 [53–65] reactions and their isotopic variants have been studied extensively as benchmark systems in the processes of understanding the nonadiabatic coupling effects in chemical reaction dynamics. In contrast, the number of quantum dynamical calculations appeared for Br + H_2 [66–69] and I + H_2 systems [70] are far less. This may be because of the difficulty in calculating accurate PESs for these reactions due to more number of electrons and much heavier mass of Br and I atoms. A large number of quantum

scattering [38–45, 47] and quasiclassical trajectory [40, 46]calculation have been done on F(^2P) + H_2 reaction using the high-quality *ab initio* PESs [48] available for this system. These theoretical calculations have successfully reproduced the major features seen in the molecular-beam scattering studies carried out on the F(^2P) + H_2 (D_2 and HD) reaction [44, 49, 50], as well as the photodetachment experiment on FH_2^- [39, 51, 52]. Similarly, a large number of experimental and theoretical studies have been done on the Cl(^2P) + H_2 reactive system and its isotopic variants [53–65].

The reverse reaction, H + HX → H_2 + X, has also motivated a lot of experimental and theoretical studies [70]. Valentini and coworkers [70] have studied extensive state-to-state dynamics of these hydrogen abstraction reactions. Schatz and coworkers [71–73] have performed time-independent quantum scattering calculations to study the effect of electronic, Coriolis and SO coupling effects on the symmetric Cl(^2P) + HCl → ClH + Cl(^2P) exchange reaction. Apart form these studies, many reseach papers and reviews have appeared on the experimental and theoretical investigations of different halogen-hydrogen reactions [see for example Ref. [74] and references therein]. The Cl(^2P) + H_2 (HD) reaction dynamics is examined in the present thesis. Therefore, in the following we briefly outline the importance and the recent advances on this system.

1.1.1 Cl(^2P) + H_2 (HD) reactions

The simplest Cl atom reaction, Cl + H_2 (HD) → HCl (DCl) + H (D) has been a subject of research for over a century [53]. Way back in 1936, Eyring and coworkers [54] have studied the chlorine-hydrogen reactions as prototypical models to establish the transition state theory. Latter on Weston Jr. proposed the bimolecular reaction rate theory modeling the same reactions in 1979 [55]. Us-

ing a semiempirical PES combined with the trajectory calculations he found a reasonable agreement between the calculated rate constant and available experimental results. The study on the isotopic substitution of hydrogen in the Cl(^2P) + H_2 reaction has established the theory of kinetic isotopic effects [56]. Other than these theoretical applications, the reaction between chlorine and hydrogen forms an elementary step in the H_2-Cl_2 reaction system, important in atmospheric chemistry and photochemical air pollution.

In most of the previous dynamical calculations on the reaction cross sections and thermal rate constants [60, 61], it was assumed that the reaction occurs adiabatically on the single ground state of the Cl + H_2 system. But recent experimental results of Liu and coworkers [62,63] on the reactivity of the ground and excited SO states of Cl (^2P) unfolds the role of open-shell character of Cl atom and such a single-surface theoretical study appears to be inadequate. For a full-dimensional dynamical calculation we need to consider all the interacting electronic states which correlate with the Cl(^2P) + H_2 reagent asymptote, as well as the nonadiabatic couplings between them.

In absence of any coupling, the six asymptotic states of Cl(^2P) + H_2 are degenerate. With the approach of the H_2 molecule the degeneracy of the ^2P state of Cl atom is lifted and it splits into three doubly degenerate PESs [75]. Two electronic states ($1^2A'$ and $1^2A''$; $^2\Sigma$ and $^2\Pi$ in the linear geometry) correlate adiabatically to the ground-state Cl ($^2P_{3/2}$) while the third state ($2^2A'$; $^2\Pi$ in the linear geometry) correlates adiabatically with excited state Cl*($^2P_{1/2}$). Of these only the lowest, which corresponds to the lower state of A' symmetry in C_s geometry, correlates with the electronic ground state of the products [HCl ($X^1\Sigma^+$) + H (^2S)]. The PESs of the two other states (the higher state of A' symmetry and the unique state of A'' symmetry) correlate with the products in

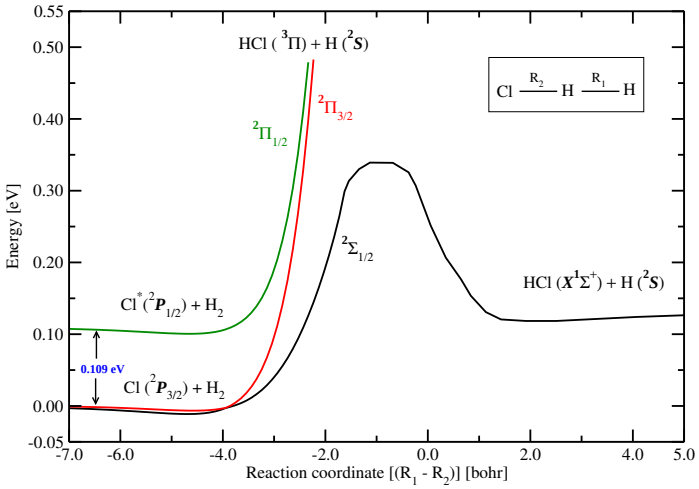

Figure 1.1: Schematic representation of the adiabatic potential energy surfaces [75] of the Cl(^2P) + H_2 system for the collinear arrangements of the three nuclei. Shown are the two SO states and their energetic splitting ~ 0.109 eV. The reagent and product asymptotes (see text) are also marked in the figure. The curves are labeled by the Hund's Case (a). The minimum of the van der Waals well in the reagent asymptote occurs at the T shaped arrangement of the nuclei.

the electronic excited state, HCl ($^3\Pi$) + H(^2S) [76–79]. This splitting has been schematically shown in Fig. 1.1. In this figure the adiabatic potential energies of the SO states of the Cl(^2P) + H_2 system is plotted along the collinear reaction path. The two states of $^2A'$ symmetry are strongly coupled and form a conical intersection in the entrance channel of the PESs [75]. The excited SO state of Cl atom ($^2P_{1/2}$), which lies 880 cm^{-1} (2.52 kcal/mol) above the ground SO state ($^2P_{3/2}$), is considerably high in energy and inaccessible at low and moderate collision energies. This excited SO state can yield products in their electronic ground state via nonadiabatic transitions (Born-Oppenheimer forbidden) to the $^2\Sigma_{1/2}$ electronic state [80]. According to the results of Liu and coworkers [62,63] the SO excited Cl*($^2P_{1/2}$) is more reactive than the SO ground state Cl ($^2P_{3/2}$). This is in apparent contradiction to conventional theoretical wisdom as the excited

state should have a higher energy barrier than the ground state [60,63,80,81]. For the chemically similar F + H_2 reaction, both theory [47] and experiment [51, 52] agree that the reactivity of the excited SO state is, at most, 10% of that of the ground state. But in case of Cl(^2P) + H_2 , where the SO coupling is about two times larger than that of F + H_2, nonadiabaticity might be more important to overcome the higher barrier hight of the reaction.

1.2 Potential Energy Surfaces of Cl(^2P) + H_2 reaction

For accurate quantum mechanical calculations availability of accurate PESs is very important. There has been a considerable progress towards the construction of the accurate global PESs for Cl(^2P) + H_2 (HD) over the years. Historically, the first semiempirical PES of the electronic ground state of the Cl(^2P) + H_2 system was constructed by Eyring and his coworkers [54]. It was later modified by Sato in 1955 [82] and was applied extensively. In 1973, Stern, Persky and Klein [83] produced three semiempirical PESs (called GSW surface) that yield good agreement with the experimental rate constants of the Cl(^2P) + H_2 abstraction reaction but were not satisfactory for the exchange reactions [84]. A more successful surface, called GQQ [84], based on some new *ab initio* data near the vicinity of the saddle point region, along with the previous semiempirical results of GSW surface [83], was developed by Schwenke *et al.* in 1989. Some exact three-dimensional quantum scattering calculations were performed on this surface [85, 86].

The best among all the semiempirical PESs known as G3 PES was presented by Allison *et al.* [87] in 1996. The G3 PES was developed by modifying the

GQQ bending potential in the Cl-H-H saddle point region by adding some *ab initio* data obtained by fourth-order Møller-Plesset perturbation theory (MP4). Detailed quasiclassical trajectory (QCT) [88], variational-transition-state-theory (VTST) [87] and quantum mechanical reactive scattering [89] calculations on G3 PES were found to be in excellent agreement with the experimental results. Despite a good success of the G3 PES in describing the Cl(^2P) + H_2 reaction dynamics [88], the recent theoretical studies of Skouteris and Manolopoulos [60] on this surface revealed two strong disagreements with the molecular beam results of Lai and Liu [62, 63]: (*i*) it failed to reproduce the preference of the DCl product over the HCl product for Cl + HD as observed in the experiment and (*ii*) the rotational excitation of the reagent H_2 has been found to hinder the reaction in contrast to the experimental results [60]. Motivated by these findings, Bian and Werner developed two (BW1 and BW2) three-dimensional PESs based on internally contracted multireference configuration interaction (MRCI) calculations [90]. The BW1 is the original *ab initio* PES without any modification. The BW2 includes some corrections to reproduce the dissociation energies of the diatomic fragments more accurately. The experimental product rotational distribution for HCl shows excellent agreement when compared with the exact quantum mechanical and quasiclassical trajectory calculations using BW PESs. Both the BW1 and BW2 PESs are obtained by diagonalizing only the electronic Hamiltonian, without the inclusion of the SO Hamiltonian [90]. Most recently, Capecchi and Werner (CW) [75] extended the calculation of Bian and Werner [90] including the relativistic SO coupling effects. This CW PES is used in the present study. We will discuss below a few important and relevant aspects of this PES.

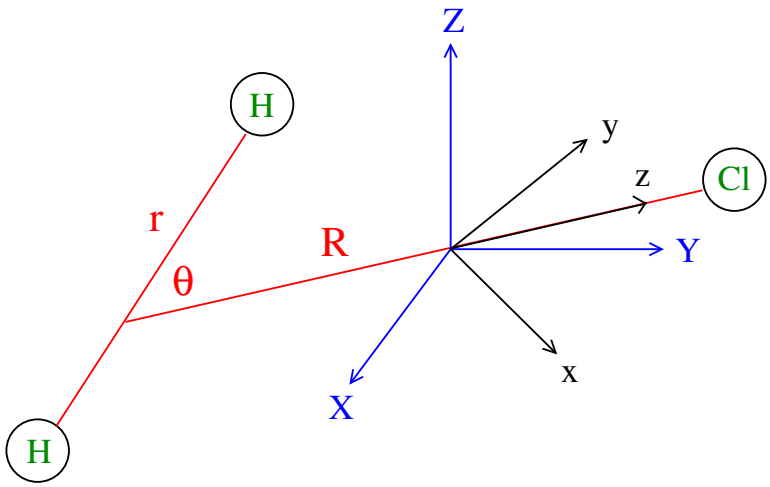

Figure 1.2: The center-of-mass coordinates for the Cl + H_2 collisions used in the space-fixed and the body-fixed frame are represented as XYZ (blue) and xyz (black) axes, respectively. The coordinate origin is the center of mass of the atom-diatom system.

1.2.1 Adiabatic and Diabatic representations of the PESs

In the following, we first describe the triatomic Cl + H_2 system in Jacobi coordinates (shown in Fig. 1.2), both in the space-fixed (SF) [91] and body-fixed (BF) [92] frames. $\vec{R}$ corresponds to the distance between Cl and the center of mass of H_2 and $\vec{r}$ corresponds to the internuclear distance of H_2. γ is the angle between $\vec{R}$ and $\vec{r}$ in the BF frame. We assume that, the vector R lies on the BF z-axis and y axis is perpendicular to the triatomic plane. The space-fixed (X, Y, Z) coordinate system is the usual laboratory frame, which is stationary and the orientation of its axis are fixed. On the other hand, the BF coordinate system is rigidly fixed in the body and its axes rotate during the course of time so as to maintain a fixed orientation relative to the particles making up the system [93].

To represent the PESs, we use the compact Cartesian notation, $|\Pi_x\rangle$, $|\Pi_y\rangle$ and $|\Sigma\rangle$ correlated with the P_x, P_y and P_z asymptotes of the Cl atom, respectively, in

collinear arrangement. The two adiabatic states of A' symmetry, to a very good approximation, correspond to a mixture of $|\Pi_x\rangle$ and $|\Sigma\rangle$ diabatic states.

$$\begin{aligned} |1A'\rangle &= |\Sigma\rangle\cos\theta + |\Pi_x\rangle\sin\theta \\ |2A'\rangle &= -|\Sigma\rangle\sin\theta + |\Pi_x\rangle\cos\theta \\ |1A''\rangle &= |\Pi_y\rangle \end{aligned}$$

$\theta \sim \theta(R, r, \gamma)$, the mixing angle, is a function of all three internal coordinates. Since, there is no coupling between the $|\Pi_y\rangle$ state of A'' symmetry with the $|\Pi_x\rangle$ and $|\Sigma\rangle$ states of A' symmetry, the adiabatic and diabatic states of A'' reflection symmetry becomes identical.

If SO coupling is taken into account, in addition to the three doubly degenerate PESs, there are five non-zero SO matrix elements in the adiabatic electronic representation [75]. In diabatic representation, however, two distinct SO matrix elements are sufficient. One of these (denoted as A) describes the splitting of the $^2\Pi$ state, and the other one (B) is the coupling of the $^2\Pi$ and $^2\Sigma$. Thus, the matrix elements of the electronic Hamiltonian in the 6×6 diabatic basis can be described in terms of three diagonal diabatic PESs, V_{xx}, V_{yy}, V_{zz}, as well as a fourth PES, V_{xz}, which is the coupling between the two states of A' symmetry and the two SO coupling matrix elements (A and B). The diabatic electronic states are expressed in terms of the adiabatic energies E_i in the following way [75]:

$$\begin{aligned} V_{zz} &= \langle\Sigma|\hat{H}|\Sigma\rangle = E_1\cos^2\theta + E_2\sin^2\theta \\ V_{xx} &= \langle\Pi_x|\hat{H}|\Pi_x\rangle = E_2\cos^2\theta + E_1\sin^2\theta \\ V_{yy} &= \langle\Pi_y|\hat{H}|\Pi_y\rangle = E_3 \\ V_{xz} &= \langle\Sigma|\hat{H}|\Pi\rangle = 1/2(E_1 - E_2)\sin 2\theta \end{aligned} \tag{1.1}$$

In this case also, for symmetry reasons the coupling potential vanishes for linear ($\gamma = 0$) and the T-shaped geometries ($\gamma = 90$), making the adiabatic and diabatic states identical for this two arrangements.

For the convenience of the expansion of the scattering wavefunctions in the dynamical calculations (described in details in Chapter 2), the PESs in diabatic Cartesian states are transformed to the signed-λ basis in terms of the projection of the electronic orbital angular momentum along $\vec{R}$: $V_\Sigma = V_{zz}$, $V_\Pi = (V_{xx} + V_{yy})/2$, $V_2 = (V_{yy}$ - $V_{xx})/2$ and $V_1 = V_{xz}/2^{1/2}$. In terms of the four diabatic PESs, the matrix of the interaction potential in the signed-λ basis is block diagonal in the spin projection quantum number and is given by

$$\hat{v} = \begin{pmatrix} & |\Sigma\rangle & |\overline{\Sigma}\rangle & |\Pi_1\rangle & |\overline{\Pi}_1\rangle & |\Pi_{-1}\rangle & |\overline{\Pi}_{-1}\rangle \\ |\Sigma\rangle & V_\Sigma & 0 & -V_1 & 0 & V_1 & 0 \\ |\overline{\Sigma}\rangle & 0 & V_\Sigma & 0 & -V_1 & 0 & V_1 \\ |\Pi_1\rangle & -V_1 & 0 & V_\Pi & 0 & V_2 & 0 \\ |\overline{\Pi}_1\rangle & 0 & -V_1 & 0 & V_\Pi & 0 & V_2 \\ |\Pi_{-1}\rangle & V_1 & 0 & V_2 & 0 & V_\Pi & 0 \\ |\overline{\Pi}_{-1}\rangle & 0 & V_1 & 0 & V_2 & 0 & V_\Pi \end{pmatrix} \tag{1.2}$$

The SO coupling matrix elements can be written as

$$A(R, r, \gamma) = i\langle \Pi_y | \mathcal{H}^{so} | \Pi_x \rangle, \quad B(R, r, \gamma) = \langle \overline{\Pi}_x | \mathcal{H}^{so} | \Sigma \rangle, \tag{1.3}$$

with $\lim_{R\to\infty} B = \lim_{R\to\infty} A$.

In terms of these two functions A and B the SO interaction potential matrix

can be written as:

$$\hat{V}^{so} = \begin{pmatrix} & |\Sigma\rangle & |\overline{\Sigma}\rangle & |\Pi_1\rangle & |\overline{\Pi}_1\rangle & |\Pi_{-1}\rangle & |\overline{\Pi}_{-1}\rangle \\ |\Sigma\rangle & 0 & 0 & 0 & -\sqrt{2}B & 0 & 0 \\ |\overline{\Sigma}\rangle & 0 & 0 & 0 & 0 & -\sqrt{2}B & 0 \\ |\Pi_1\rangle & 0 & 0 & -A & 0 & 0 & 0 \\ |\overline{\Pi}_1\rangle & -\sqrt{2}B & 0 & 0 & A & 0 & 0 \\ |\Pi_{-1}\rangle & 0 & -\sqrt{2}B & 0 & 0 & A & 0 \\ |\overline{\Pi}_{-1}\rangle & 0 & 0 & 0 & 0 & 0 & -A \end{pmatrix} \tag{1.4}$$

where the bar over the states represent the second spin component.

1.2.2 Topography of the PESs

The lowest adiabatic states $1A'$, $2A'$ and $1A''$ of Cl(^2P) + H_2 system have been computed by means of internally-contracted multireference configuration interaction method (IC-MRCI) by Chapecchi and Werner [75] recently using MOLPRO package of *ab initio* programs [94]. The six resulting potentials have been fitted to analytical functions.

The barrier on the ground state potential of Cl(^2P) + H_2 reaction appears in the linear geometry of the three nuclei. The location and the height of the barrier are found to be almost identical without and with SO coupling, as demonstrated in Table. 1.1. Since at the barrier the $^2\Pi$ state is already very high in energy (see Fig. 1.1), the effect of SO coupling between the $^2\Pi$ and $^2\Sigma$ states becomes negligible. Thus, at the barrier the energy of the $^2\Sigma$ state is hardly affected by the SO coupling, while the Cl(^2P) + H_2 asymptote is lowered by 1/3 of the SO splitting of the Cl-atom. This effectively leads to an increase of the barrier height by the same amount (0.84 kcal/mol).

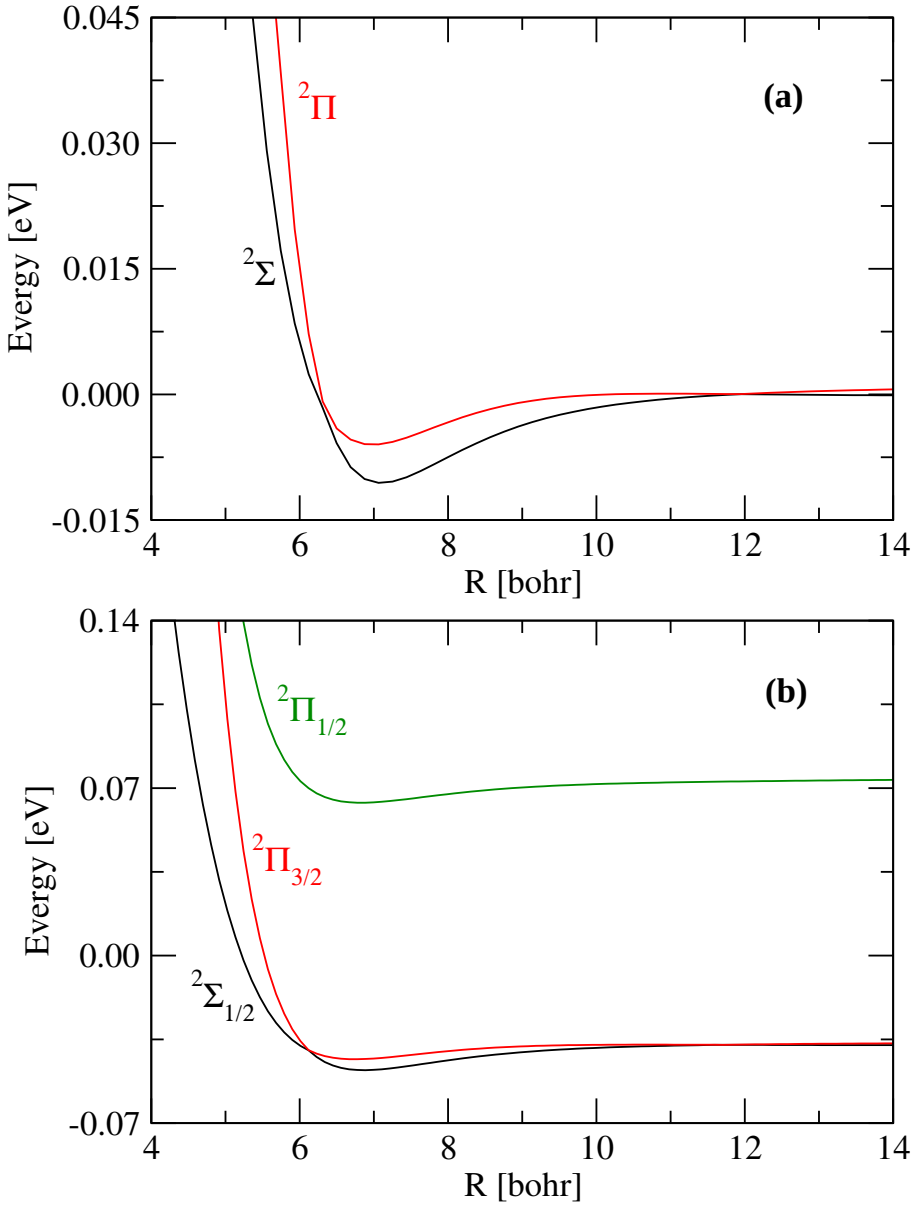

Figure 1.3: One dimensional cuts of the diabatic potential energy surfaces of the Cl(^2P) + H_2 system for the collinear geometries (r = 1.4 a_0) in the absence (panel a) and presence (panel b) of SO coupling reproduced from Ref. [75]

Table 1.1: Comparison of barrier properties for the Cl(^2P) + H_2 reaction

Surface	R (a_0)	r (a_0)	γ (rad)	E (eV)	ω_i -	ω_b cm^{-1}	ω_s cm^{-1}
CW	3.631	1.854	0.0	7.60	1296i	541	1361
BW2	3.631	1.854	0.0	7.61	1294i	540	1360

In the absence of SO coupling, the potential energy cuts of $^2\Sigma$ and $^2\Pi$ adiabatic electronic states as a function of R, are shown in Fig. 1.3(a) for collinear arrangement of Cl(^2P) + H_2 at the equilibrium distance of H_2 (r = 1.4 a_0). As shown in the figure 1.3(a), there is an avoided-crossing of the $^2\Sigma$ and $^2\Pi$ potentials at an intermediate distance (about at R = 6.1 a_0) which leads to a conical intersections in non-collinear geometries. The effect of SO coupling in $^2\Sigma$ and $^2\Pi$ adiabatic electronic states are shown in Fig. 1.3(b). The $^2\Sigma_{1/2}$, $^2\Pi_{3/2}$ and $^2\Pi_{1/2}$ electronic states are plotted as a function of R. The $^2\Sigma$ state is hardly affected by SO coupling while the splitting of the $^2\Pi_{3/2}$ and $^2\Pi_{1/2}$ state corresponds to the SO coupling constant of Cl-atom (882 cm^{-1}).

We present in Figs 1.4(a-b), the contour plots of the diabatic Σ and Π potentials as a function of R and r for the collinear geometry of the three nuclei. The Σ potential, shown in Fig. 1.4(a), is most attractive in perpendicular geometries ($\gamma = 90^0$). There are wells in the entrance and exit channels, separated by the central barrier. The minimum occurs at R = 5.78 a_0 , r = 1.403 a_0 and the well depth amounts 0.51 kcal/mol [90]. At collinear geometries the potential is also attractive, but the well depth is only 0.3 kcal/mol. On the contrary, the V_Π potentials (the average of the two $^2\Pi$ potentials) shown in Fig. 1.4(b), is repulsive at small values of R. The above features are in sharp contrast with the semiempirical G3 PES [87]. G3 PES has no minimum and it is most repulsive for $\gamma = 90^\circ$ and these differences lead to completely different dynamical behavior at

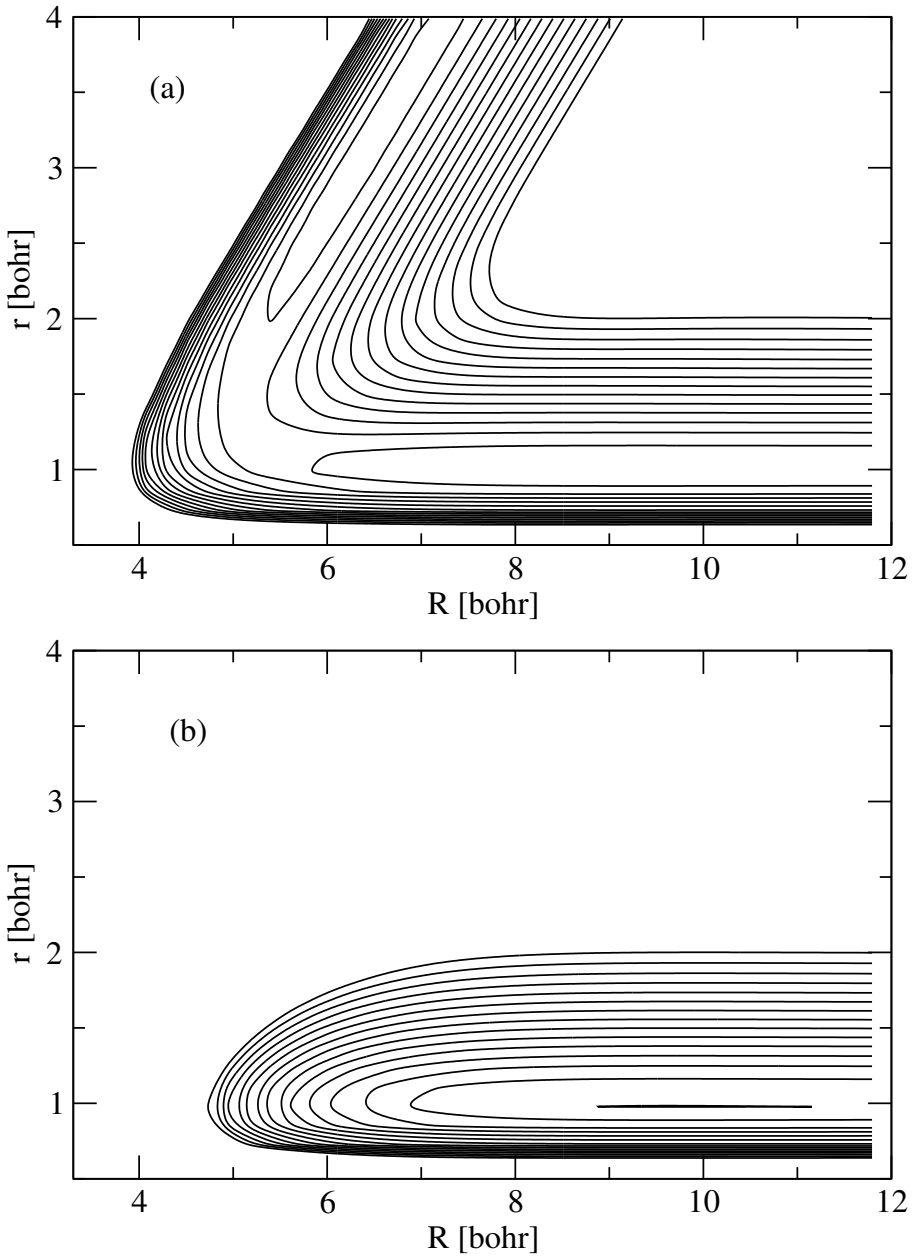

Figure 1.4: Contour plot of the adiabatic $^2\Sigma$ (panel *a*) and $^2\Pi$ (panel *b*) CW PES of Cl(^2P) + H_2 for the collinear arrangement of the three nuclei. The contour levels are plotted in the range of 0 - 3 eV with a increment of 0.3 eV for each contour lines.

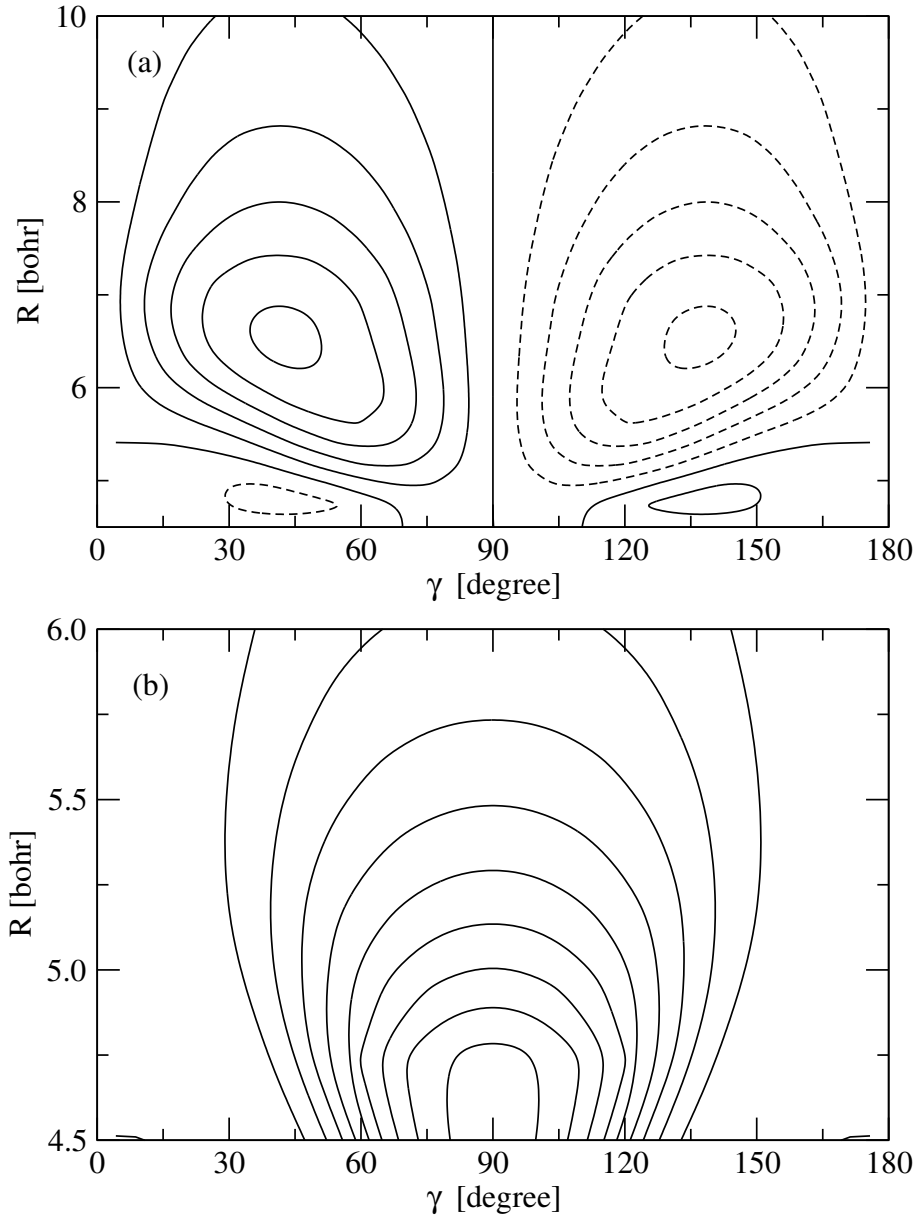

Figure 1.5: Same as 1.4, for the diabatic coupling potential V_1 (panel a) and diabatic difference potential V_2 (panel b) as a function of R and γ. The dotted lines correspond to negative energies.

low collision energies [60].

The diabatic coupling potentials are shown in Figs. 1.5(a-b). The V_1 potential, shown in Fig. 1.5(a) is zero for $\gamma = 0$, 90, 180^0 and changes sign at these angles. The V_2 potential which describes the splitting of the two diabatic $^2\Pi$ potentials is shown in Fig. 1.5(b). This potential is zero for $\gamma = 0$ and 180^0 and has a maximum at 90^0. The splitting between the two Π states increase with decreasing R.

1.3 Current state of research and the aim of the present work

Recently, Taatjes [57] have carried out infrared frequency-modulation measurements of absolute rate constants for the Cl + HD reaction. The angular distribution and time-of flight spectra for Cl + H_2 and Cl + D_2 reactions were measured in a crossed molecular beam apparatus by Alagia *et al.* [58]. Employing a photoinitiated reaction technique Kandel *et al.* [59] measured the vibrationally state-resolved differential cross sections and product rotational distributions for the Cl + HD reaction. But, in light of the new measurements on the reactivity of the ground Cl ($^2P_{3/2}$) and excited Cl*($^2P_{1/2}$) SO states by Liu and coworkers, [62,63], this reaction has received a renewed interest for theoretical study.

The reactivity of the excited SO electronic states of Cl(^2P) is explored by Alexander and coworkers [80, 95]. by a time-independent wave packet approach. They found that the Coriolis coupling has a considerably weaker effect and SO coupling is responsible for the major nonadiabatic effects. With a direct contrast with the experimental results, they predict that the BO-allowed reaction of the ground state will be much more efficient that the BO-forbidden reaction of the excited SO state. Differential cross sections (DCS) on the coupled electronic

PESs have been calculated by Balucani *et al.* . [81]. Their calculations suggest that the magnitude of the DCSs for the SO excited state reaction are much smaller than the ground state and the excited SO state plays a minor role in the reaction. Thermal rate constants including the SO coupling in the dynamics is calculated by Manthe [96] by the multi-configuration time-dependent Hatree (MCTDH) approach [97]. A detailed comparison with previous results based on non-relativistic PES is also given along with the experimental results.

The aim of the present work is to study the the effect of the nonadiabatic coupling on some dynamical observables *viz.*, the initial state-selected reaction probabilities, integral reaction cross sections, thermal rate constants etc. of $Cl(^2P)$ + H_2 (HD) $\rightarrow$ HCl (DCl) + D (H) reactions with the aid of a time-dependent wave packet (TDWP) approach. The photodetachment spectrum of ClH_2^- (ClD_2^-) are recorded by Neumark and coworkers [64, 65]. We simulate this spectrum theoretically by propagating wave packets on the coupled multi-sheeted reactive PESs of Cl + H_2 (D_2) and compared the results with the experimental findings. The calculated photodetachment spectrum reveals resolved structures of low-frequency van der Waals resonances. These dynamical resonances in $Cl(^2P)$ + H_2 scattering are identified and characterized, subsequently. Finally, the dissociation dynamics of Cl···HD van der Waals complex following the electron detachment of Cl^-–HD anion is studied and the effect of the nonadiabatic coupling on the channel-specific dissociation probabilities are analyzed.

1.4 Overview of the Thesis

In Chapter 2, we present a detailed theoretical framework to deal with the nuclear dynamics in the coupled-state situation by a TDWP approach. The nuclear dynamics is treated with a two-state model Hamiltonian considering the electronic coupling effects only and with a three-state model Hamiltonian when the electronic and SO coupling are included in the calculations. The flux operator is represented both in the adiabatic as well as diabatic electronic representations to calculate the initial state-selected and energy resolved reaction probabilities. Preparation of the initial WP, its propagation and the final analysis - each of these topics are discussed at length in this chapter. The reaction probabilities depending on the total angular momentum J are summed up using the coupled-state (CS) approximation to calculate the integral reaction cross sections and the averaging of the latter over the collision energies at a given temperature yields the thermal rate constants.

In chapter 3, we discuss the reaction probability results of $Cl(^2P)$ + H_2 (HD) obtained with the formalism outlined in chapter 2. The reaction probability obtained including electronic coupling alone and including both the electronic and SO coupling are calculated both in adiabatic and diabatic electronic representations. The coupled state results with the inclusion of only electronic coupling do not differ much from the uncoupled ones but the SO coupling has a significant impact on the dynamics. The reactivity of the different SO states of $Cl(^2P)$ + H_2 reaction is also examined. The Π states are nonreactive in the adiabatic limit. But these states can yield product in their electronic ground state via the nonadiabatic transition to the $^2\Sigma_{1/2}$ state. The time-dependence of the electronic population in the adiabatic and diabatic electronic representations and the probability density of the WP in different times are also discussed in details in this

chapter.

The channel specific reaction probability of the Cl(^2P) + H_2 (HD) reaction for $J > 0$ is studied thereafter. We have calculated the reaction probabilities with partial-wave contribution upto total angular momentum $J = 58$ for Cl(^2P) + H_2 and $J = 69$ for the Cl(^2P) + HD reactions. The channel specific integral reaction cross sections for the uncoupled and coupled state situations are compared with the available experimental results. The thermal rate constants are obtained by statistically averaging over the rotational states $j = 0$ - 2. Compared to the uncoupled state results, we find that the theoretical rate constants including the electronic and SO coupling are closer to the available experimental results for both the Cl(^2P) + H_2 and Cl(^2P) + HD reactions.

In chapter 4, the photodetachment spectrum of ClH_2^- (ClD_2^-) is theoretically calculated probing the pre-reactive van der Waals region of the Cl(^2P) + H_2 asymptote. We consider a Franck-Condon (FC) transition from the ClH_2^- (ClD_2^-) anion to the three coupled electronic states of neutral ClH_2 (ClD_2). A time-dependent version of the Fermi-Golden rule expression is used to calculate the spectral intensity. The final theoretical result obtained with the initial of ClH_2^- are in good accord with the experimental recording of Neumark and coworkers [64, 65]. An examination of the fine structures of the theoretical spectrum revealed van der Waals progression (motion along the Cl $\cdots H_2$ coordinate) as well as progression along the ClH_2 bending vibration and H_2 vibration. This is illustrated by plotting the probability density contours ($|\Psi|^2$) of the eigenfunctions. The effect of nonadiabatic coupling is also analyzed on the energy eigenvalue spectra of few representative peaks.

In chapter 5, we study the dissociation dynamics of the Cl$\cdots$HD van der Waals complex following the electron detachment of Cl^-–HD anion. The Cl^-–HD anion

is promoted to the reactive PES of neutral Cl···HD upon photodetachment. A FC transition is assumed for this step and the subsequent reaction dynamics is simulated by means of quantum WP propagation. The channel specific, HCl + D or DCl + H or Cl + HD, dissociation probabilities are calculated both for the uncoupled and coupled state situations. It is found that the dissociation to the Cl + HD nonreactive channel is dominated followed by the HCl + D and DCl + H reactive channels, respectively, in both uncoupled and coupled state situations.

Finally, the summarizing remarks including the future direction are provided in Chapter 6.

In Appendix 1, a theoretical study of the photoelectron spectrum of F_2O pertaining to an ionization to the ground ($\widetilde{X}\ ^2B_1$) and low-lying excited electronic states ($\widetilde{A}\ ^2B_2$, $\widetilde{B}\ ^2A_1$ and $\widetilde{C}\ ^2A_2$) of F_2O^+ were presented. The vibronic interactions between the $\widetilde{A}\ ^2B_2$ and $\widetilde{B}\ ^2A_1$ electronic states of F_2O^+ are treated within a linear coupling approach and the strength of the vibronic coupling parameter is calculated by *ab initio* method. The nuclear dynamics is simulated both by time-independent and time-dependent quantum mechanical wave packet approaches. While the first photoelectron band exhibit resolved vibrational progression along the symmetric stretching mode the second one is highly overlapping. The latter is attributed to the nonadiabatic interactions among the energetically close $\widetilde{A}\ ^2B_2$, $\widetilde{B}\ ^2A_1$ and $\widetilde{C}\ ^2A_2$ electronic states of F_2O^+. The theoretical findings are in good accord with the available experimental results.

Chapter 2

Reactive Scattering Dynamics on the Coupled Electronic manifold

2.1 Introduction

In the following we describe the formalism to study the reactive scattering dynamics of a bimolecular collision occurring on a coupled manifold of electronic states. The nuclear dynamics is studied with a two-state model considering only the electronic coupling in the dynamics. A three-state model is used when both the electronic and SO coupling are included in the dynamics. The flux operator is represented both in an adiabatic as well as in a diabatic electronic representation in the two-state model, whereas, only a diabatic electronic representation is employed throughout in the three-state model. In a reactive scattering study, ideally the reaction is initiated in an adiabatic electronic representation and then transformed to a diabatic electronic representation for propagation in which, the diverging kinetic coupling terms of the adiabatic representation change into smooth potential energy coupling terms as stated in Chapter 1 [10]. Due to

the associated complexity (and uncertainty) in defining a suitable adiabatic-to-diabatic transformation angle, it often becomes cumbersome when the number of participating electronic state increased. However, one can use a numerical diagonalization method to approximately calculate the adiabatic-to-diabatic transformation matrix elements. The final scattering attributes can be analyzed both in the adiabatic as well as in the diabatic electronic representations and one finally arrives at identical results in either way.

2.2 A general scheme to solve the TDSE

The molecular collisions generally take place in the position-momentum and the time-energy space. In order to model the collision process, a discrete Hilbert space [98, 99] is constructed in the from of a grid. The discrete grid is usually constructed in the coordinate space, with each grid point being characterized by a finite value of interaction potential. The coordinate space, (x), is divided into a set of N discrete points with a spacing of Δx between two successive points. The eigenvalues of the position operator $\hat{x}$ at each grid points are given by [99]:

$$x_i = (i-1)\Delta x, i = 1, ..., N \tag{2.1}$$

The corresponding eigenvectors $|x_i\rangle$, are given by the orthogonality and completeness relations and the wavefunctions for an arbitrary physical state can be represented as $\phi(x_i) = \langle x_i|\phi\rangle$. Wavefunctions are normalized on the grid and the normalization integral becomes $\int_{-\infty}^{+\infty} \phi^\star(x)\phi(x)dx = 1$. The maximum length of the grid ($L = N\Delta x$) along the spatial coordinate x, determines the spacing

between two successive points in the momentum space (k):

$$\Delta k = \frac{2\pi}{N\Delta x}. \tag{2.2}$$

In the momentum space, the grid is centered at zero and all other points are distributed symmetrically on either side of it. If the maximum momentum is represented by p_{max} ($=\hbar k_{max}$) in the k space, then the total momentum ranges from $-p_{max}$ to $+p_{max}$.

Once the grid is set up, the nuclear motion on the electronic PESs is monitored by solving the time-dependent Schrödinger equation:

$$i\hbar\frac{\partial\Psi}{\partial t} = \hat{H}\Psi \tag{2.3}$$

where, $\hat{H}$ ($=\hat{T}+\hat{V}$) defines the Hamiltonian operator of the system. $\hat{T}$ is the nuclear kinetic energy part of the Hamiltonian and $\hat{V}$ defines the potential energy part. For a general $A+BC$ atom-diatom reaction, represented in ordinary Jacobi coordinates (see Sec. 1.2.1 for details) the Hamiltonian operator is given by

$$\hat{H} = -\frac{\hbar^2}{2\mu}\frac{\partial^2}{\partial R^2} - \frac{\hbar^2}{2\mu'}\frac{\partial^2}{\partial r^2} - \frac{\hbar^2}{2I}\frac{1}{\sin\gamma}\frac{\partial}{\partial\gamma}\left(\sin\gamma\frac{\partial}{\partial\gamma}\right) + V(R,r,\gamma). \tag{2.4}$$

The first two terms in the right hand side of the above equation represent the radial kinetic energy operators along R and r, respectively, and the third term represents the rotational kinetic energy operator. The quantity, $\mu = m_A(m_B + m_C)/(m_A+m_B+m_C)$, is the $A+BC$ three-body reduced mass, $\mu' = m_Bm_C/(m_B+m_C)$, is the BC reduced mass where m_A, m_B and m_C are the masses of A, B and C nuclei, respectively. The quantity I represents the moments of inertia of the collisional system, $\frac{1}{I} = \frac{1}{\mu R^2} + \frac{1}{\mu' r^2}$.

For this explicitly time-independent Hamiltonian, the solution of the TDSE reads

$$|\Psi(t)\rangle = \exp\left[\frac{-i\hat{H}t}{\hbar}\right]|\Psi(t=0)\rangle, \tag{2.5}$$

where, $|\Psi(t=0)\rangle$ and $|\Psi(t)\rangle$ are the wavefunctions of the reacting system at time 0 and t, respectively.

In order to solve this equation numerically, we need to evaluate the action of the kinetic ($\hat{T}$) and potential ($\hat{V}$) energy operators on the Hamiltonian separately. Since $\hat{T}$ and $\hat{V}$ do not commute with each other as $\hat{T}$ is a function of the momentum space (p), and $\hat{V}$ is a function of position (x) only. The operator $\hat{V}$ being local in the coordinate space, its action on Ψ is only a multiplication of its magnitude with the value of Ψ at each grid point x_i:

$$\hat{V}(x)\Psi(x_i) = V(x_i)\Psi(x_i) \tag{2.6}$$

But the kinetic energy operator ($\hat{T} = \frac{\hat{p}^2}{2m} = \frac{\hbar^2 k^2}{2\mu}$) is nonlocal in the coordinate space and the evaluation of the $\hat{T}\Psi$ can not be done by a simple multiplication. This operation can be done through a suitable collocation technique [100, 101] by utilizing the concept of the discrete Hilbert space.

The basic idea behind the collocation method is to use two different representations of the function: (i) A grid representation; where the function is known by its value at the grid points $\{x_i\}$, e.g. $\hat{V}$, and (ii) A basis set representation $\{g_n(x)\}$; where the continuous functions are approximated at each point by a discrete sum in terms of a finite basis set. The basis functions $\{g_n(x)\}$ at various grid points x_i are connected through appropriate expansion coefficients (a_n) at

the grid points:

$$\Psi(x_i) \equiv \overline{\Psi}(x_i) = \sum_{n=0}^{N-1} a_n g_n(x_i) \tag{2.7}$$

where N is the size of the basis set. This method is adapted for the evaluation of a nonlocal operator, e.g. $\hat{T}$ such that

$$\hat{T}\Psi(x) = \frac{\hbar^2 k^2}{2\mu}\overline{\Psi}(k) = \frac{\hbar^2 k^2}{2\mu} a_k, \tag{2.8}$$

This technique is also known as a pseudospectral approximation.

A special case of the collocation technique is the Fourier method [100–103]. With the use of Fourier transform one can switch back and forth between the two reciprocal Hilbert spaces (e.g. position and momentum or the time and frequency). As a result, Fourier transform is generally used to evaluate the action of $\hat{T}$ on Ψ.

In this method, the wavefunction $\Psi(x)$ is expanded in terms of the orthogonal plane wave basis functions:

$$\Psi(x) \approx \sum_{k=-(N/2-1)}^{N/2} a_k \exp\left[i2\pi kx/L\right], \tag{2.9}$$

where, a_k is becomes the Fourier expansion coefficient and it represents the amplitude of the wavefunction in momentum space. Using the orthogonality relation between the Fourier functions, one can obtain these coefficients by inverting the relation with a set of equidistant sampling points $\{x_i\}$

$$a_k = \frac{1}{N}\sum_{i=1}^{N} \Psi(x_i) \exp\left[-i2\pi kx_i/L\right]. \tag{2.10}$$

These are discrete Fourier transforms.

The use of fast Fourier transform (FFT) method for computing the action of the kinetic energy part of the Hamiltonian on the wavefunction was first introduced by Feit *et al.* [104] and Kosloff and Kosloff [102] In this method, the action of the kinetic energy operator on $\Psi(x)$ involves transforming the coordinate space wave function to momentum space by forward FFT (FT), multiplying by the kinetic energy $T(k)$, and then transforming it back to the coordinate space by an inverse FFT (FT^{-1}). In general, the continuous FFT can be represented as:

$$FT[\Psi(x)] = \overline{\Psi}(k) = \frac{1}{\sqrt{2\pi}} \int_{-\infty}^{\infty} \Psi(x) e^{-ikx} dx. \tag{2.11}$$

$$FT^{-1}[\overline{\Psi}(k)] = \Psi(x) = \frac{1}{\sqrt{2\pi}} \int_{-\infty}^{\infty} \overline{\Psi}(k) e^{ikx} dk \tag{2.12}$$

This method requires the wave function to satisfy periodic boundary conditions and for band-limited functions this transformation is exact [102]. Functions under these potentials remain localized in the phase space box where the amplitude of the function becomes zero at the boundary of the box. Otherwise, as time progresses the WP gradually reaches the grid edges and undergoes spurious reflections resulting interference between the outgoing and reflected components. But wave functions (except the semilocalized wave functions) can not be confined simultaneously both in coordinate and momentum spaces. This boundary conditions for the wave packets can be met by using absorbing boundaries, e.g. a negative imaginary potential (NIP) of the form $-iV_0$, in addition to the real potential of the system at the last few points near the grid edges [105]. They provide a convenient way to damp the WP components to reduce their amplitude to zero at the grid boundaries and thereby prevent the unphysical reflections. One more attractive feature of the FFT method [106] is that it scales as $O(N \log N)$ with the number of grid points N. Thus this method becomes especially suitable

for large-scale problems as the computational effort increases slowly with the grid size.

But this FFT scheme is numerically inefficient to calculate the rotational part of the kinetic energy operator. This is because the rotational kinetic energy operator contains a $(1/\sin^2\gamma)$ term which leads to singularity in the discrete angle space for $\gamma = 0$ and π. One can deal with this situation by using a discrete variable representation (DVR) and finite basis representation (FBR). The DVR-FBR transformation is an example of another orthogonal collocation method which uses specific basis functions and points on the grid [107,108]. This method uses an orthogonal transformation between the DVR and the FBR and vice versa. The DVR is a basis consisting N discrete points, whereas the FBR is a basis consisting of N square-integrable functions appropriate to the DVR coordinates. In the DVR, the continuous eigenvalues of the coordinate operator is discretized [109] by diagonalizing the relevant Hamiltonian matrix. The matrix elements are determined by orthogonal transformation relation between the points and the basis functions. Both the basis are designed to evaluate the action of the operators in their respective local representations.

It has been shown by Light and coworkers [110–112], in the framework of DVR representation, the collocation method is much more efficient when the two representations are related through some quadrature scheme. Following the work of Harris *et al.* [107], Dickinson and Certain [108] proposed the use of orthogonal polynomial basis functions (e.g. the Hermite polynomials), corresponding to the Gaussian quadrature to carry out an orthogonal transformation between the N quadrature points and N basis functions. The γ_k grid points have been taken as the abscissas of a Gauss-Legendre quadrature, such that the rotational kinetic energy operator is diagonal in the associated Legendre polynomial basis

set $\{P_l^{\Omega}(\cos\gamma)\}$.

In summary, all the operations involving in the $\hat{H}\Psi$ are represented schematically in the following.
If $\Psi = \{\Psi_{ijk} = \Psi(R_i, r_j, \theta_k)\}$ is the grid representation of the wave function, and χ is the corresponding momentum representation, the total Hamiltonian of Eq. 2.4 will be acted on ψ in the following way:

(i) Kinetic energy $\partial^2/\partial R^2$ term,

$$\Psi \rightarrow \underline{FFT(R)} \rightarrow \{\chi^{(R)}_{mjk}\} \rightarrow \underline{\times \left[-K_m^{(R)}\right]} \rightarrow \{\chi''^{(R)}_{mjk}\} \rightarrow \underline{FFT^{-1}(R)} \rightarrow \Psi^{(1)}.$$

(ii) Kinetic energy $\partial^2/\partial r^2$ term,

$$\Psi \rightarrow \underline{FFT(r)} \rightarrow \{\chi^{(r)}_{ink}\} \rightarrow \underline{\times \left[-K_n^{(r)}\right]} \rightarrow \{\chi''^{(r)}_{ink}\} \rightarrow \underline{FFT^{-1}(r)} \rightarrow \Psi^{(2)}.$$

(iii) Kinetic energy $(1/2I\sin\theta)(\partial/\partial\theta)[\sin\theta(\partial/\partial\theta)]$ term,

$$\Psi \rightarrow \underline{\tau(\theta)} \rightarrow \{\chi^{(\theta)}_{ijl}\} \rightarrow \underline{\times \left[-\tfrac{1}{2I(R_i,r_j)}l(l+1)\right]} \rightarrow \{\chi''^{(\theta)}_{ijl}\} \rightarrow \underline{\tau^{-1}(\theta)} \rightarrow \Psi^{(3)}.$$

(iv) Potential energy term $V(R, r, \theta)$,

$$\Psi \rightarrow \underline{\hat{V}} \rightarrow \{V(R_i, r_j, \theta_k)\psi_{ijk}\} \equiv \Psi^{(4)}.$$

Finally,

$$\hat{H}\Psi = -\frac{\hbar^2}{2\mu}\Psi^{(1)} - \frac{\hbar^2}{2\mu'}\Psi^{(2)} - \hbar^2\Psi^{(3)} + \Psi^{(4)}$$

2.3 The Hamiltonian

The Hamiltonian describing the vibronic and SO interactions of the electronic states and the nuclear motion in Cl(^2P) + H_2 collisions is most conveniently written in a diabatic electronic representation. In this representation the coupling between the surfaces is caused by the off-diagonal elements of the electronic part of the Hamiltonian and the nuclear part is diagonal [26]. It is conveniant to use the mass-scaled reactant channel Jacobi Coordinates R, r and γ in the body-fixed frame in order to describe the collision process. The mass-scaled Jacobi coordinates can be defined in terms of the ordinary Jacobi coordinate as:

$$R' = R\lambda \text{ and } r' = r/\lambda,$$

where, $\lambda = \sqrt{\frac{\mu}{\mu'}}$, is the scaling factor. For a general $A + BC$ system, the scaled three body reduced mass, μ, and the diatomic reduced mass, μ', are given by

$$\mu' = \frac{m_B m_C}{m_B + m_C} \tag{2.13}$$

$$\mu = \sqrt{\frac{m_A m_B m_C}{m_A + m_B + m_C}}, \tag{2.14}$$

where, m_A, m_B and m_C are the masses of the atom A, B and C, respectively. The Jacobi angle (angle between $\vec{R}$ and $\vec{r}$) is denoted by γ. The body-fixed z axis is defined to be parallel to $\vec{R}$ and H_2 lies in the xz plane.

In the following, the schemes outlined by Rebentrost and Lester [113], Schatz and coworkers [114] and Alexander and coworkers [47] we denote the various angular momentum terms of the Hamiltonian. The electronic orbital angular momentum vector of the atom is denoted by $\boldsymbol{l}$ with l [=1 for Cl(^2P)] being the corresponding quantum number, the electronic spin angular momentum vector

of the atom is denoted by $\boldsymbol{s}$ where s [$= \pm 1/2$ for Cl(^{2}P)] is the corresponding quantum number. $\boldsymbol{L} = \boldsymbol{l} + \boldsymbol{s}$, describes the electronic total angular momentum of the atom and L is the corresponding quantum number with values L=1/2 or 3/2. The nuclear rotational angular momentum vector of the diatom is denoted by $\boldsymbol{j}$, the nuclear orbital angular momentum vector of the atom relative to the diatom is denoted by $\boldsymbol{N}$ with corresponding quantum numbers being j and N respectively. The total (electronic plus nuclear) angular momentum is denoted by $\boldsymbol{J}$ [$=\boldsymbol{L} + \boldsymbol{j} + \boldsymbol{N}$] where the corresponding quantum number J can have half integer values. The body-fixed projection quantum number associated with $\boldsymbol{j}$, $\boldsymbol{L}$, and $\boldsymbol{J}$ are denoted as Ω_j, Ω_L and Ω, respectively. With the choice of the present body-fixed z axis, we have $\Omega = \Omega_j + \Omega_L$.

The general form of the diabatic multi-state Hamiltonian for the Cl(^2P) + H_2 reactive system can be written as:

$$\mathcal{H} = \mathcal{H}^{Nu} + \mathcal{H}^{el} + \mathcal{H}^{so} \tag{2.15}$$

where $\mathcal{H}^{Nu}$ is the nuclear part of the Hamiltonian, $\mathcal{H}^{el}$ represents the nonrelativistic electronic Hamiltonian and $\mathcal{H}^{so}$ is the relativistic SO Hamiltonian. With the set of mass-scaled Jacobi coordinates (R, r and γ) as described above, the (diagonal) nuclear part of the Hamiltonian can be written as:

$$\mathcal{H}^{Nu} = \frac{1}{2\mu}\left[P_R^2 + P_r^2\right] + \frac{\boldsymbol{j}^2}{2\mu r^2} + \frac{\boldsymbol{N}^2}{2\mu R^2} \tag{2.16}$$

Here P_R and P_r are the momentum operators corresponding to the two Jacobi distances R and r, respectively. $\mathcal{H}^{el}$ represents the nonrelativistic electronic Hamiltonian and $\mathcal{H}^{so}$ is the relativistic SO Hamiltonian. The centrifugal term in Eq.

(2.16) can further be expressed by substituting $\boldsymbol{N} = \boldsymbol{J} - \boldsymbol{L} - \boldsymbol{j}$ as [114]

$$\begin{aligned}\frac{\boldsymbol{N}^2}{2\mu R^2} &= \frac{(\boldsymbol{J}^2 + \boldsymbol{L}^2 + \boldsymbol{j}^2)}{2\mu R^2} - \frac{(2\boldsymbol{J}.\boldsymbol{L} + 2\boldsymbol{J}.\boldsymbol{j} - 2\boldsymbol{j}.\boldsymbol{L})}{2\mu R^2} \\ &= \frac{(\boldsymbol{J}^2 + \boldsymbol{L}^2 + \boldsymbol{j}^2)}{2\mu R^2} - \frac{J_z L_z + J_z j_z - j_z L_z}{\mu R^2} \\ &\quad \frac{1}{2\mu R^2}\left[(J_+ L_- + J_- L_+) + (J_+ j_- + J_- j_+) - (L_+ j_- + L_- j_+)\right] \quad (2.17)\end{aligned}$$

The terms arising from the coupling between the $\boldsymbol{J}$, $\boldsymbol{L}$ and $\boldsymbol{l}$ operators, in terms of the raising and lowering operators, appears in the off-diagonal part of the nuclear Hamiltonian and are known as Coriolis coupling terms. By neglecting these Coriolis coupling terms one arrives at the well known coupled-states or centrifugal Sudden (CS) Approximation [93, 115]. Within this approximation, Ω becomes a good quantum number and it is conserved in the BF frame. This approximation greatly simplifies the $J \neq 0$ calculations by reducing the computational dimensionality of the problem and provides reasonably accurate results for many bimolecular reactions [116–120].

We utilize this general form of the Hamiltonian in our subsequent study of the electronic and SO coupling effects in $Cl(^2P) + H_2$ reaction.

2.3.1 A two-state model Hamiltonian to study the electronic coupling effect

It is noted before that, when SO couplings are not considered in the dynamics, the $^2\Sigma$ and $^2\Pi$ electronic states of $Cl(^2P) + H_2$ system forms a conical intersection at the collinear arrangements of the three nuclei. The nuclear dynamics is studied with a two-state nonrelativistic model in this case. The diabatic Hamiltonian for the total angular momentum $\boldsymbol{J} \neq 0$, [Eqs (A.1-2.17)] for the $^2\Sigma$-$^2\Pi$ interacting

electronic manifold can then be expressed as

$$\begin{aligned}\mathcal{H}^d &= \mathcal{H}^{Nu} + \mathcal{H}^{el} \\ &= T_N \begin{pmatrix} 1 & 0 \\ 0 & 1 \end{pmatrix} + \begin{pmatrix} H_\Sigma & H_{\Sigma\Pi} \\ H_{\Pi\Sigma} & H_\Pi \end{pmatrix}, \end{aligned} \tag{2.18}$$

where T_N represents the nuclear kinetic energy operator

$$\begin{aligned} T_N &= \frac{1}{2\mu}\left[P_R^2 + P_r^2\right] + \frac{\boldsymbol{j}^2}{2I} + \frac{J^2}{2\mu R^2} \\ &= -\frac{\hbar^2}{2\mu}\left[\frac{\partial^2}{\partial R^2} + \frac{\partial^2}{\partial r^2}\right] - \frac{\hbar^2}{2I}\frac{1}{\sin\gamma}\frac{\partial}{\partial\gamma}\left(\sin\gamma\frac{\partial}{\partial\gamma} - \frac{\Omega^2}{\sin^2\gamma}\right). \end{aligned} \tag{2.19}$$

The quantity I represents the three-body moment of inertia, $I = \mu R^2 r^2/(R^2+r^2)$. H_Σ and H_Π in Eq. (2.18) are the energies of the ‘ $^2\Sigma$ -like’and ‘ $^2\Pi$ -like’diabatic electronic states, respectively and $H_{\Sigma\Pi} = H_{\Pi\Sigma}$ is the Σ-Π electronic coupling potential.

The electronic part of the Hamiltonian is diagonal in the adiabatic electronic representation and the off-diagonal elements of the nuclear part describe the nonadiabatic coupling between the two states. The adiabatic Hamiltonian can be obtained from diabatic one of Eq. (2.18) through a similarity transformation as

$$\begin{aligned}\mathcal{H}^{ad} &= \boldsymbol{S}^\dagger \mathcal{H}^d \boldsymbol{S}, \\ &= T_N \mathbf{1} + \boldsymbol{S}^\dagger \left[T_N, \boldsymbol{S}\right] + \begin{pmatrix} V_\Sigma & 0 \\ 0 & V_\Pi \end{pmatrix}, \end{aligned} \tag{2.20}$$

where T_N represents the nuclear kinetic energy operator of Eq (2.19). The nonadiabatic coupling matrix is given by, $\boldsymbol{\Lambda} = -\boldsymbol{S}^\dagger[T_N, \boldsymbol{S}]$. The quantity $V_{\Sigma(\Pi)}$ denotes

adiabatic potential energy of the $^2\Sigma(^2\Pi)$ state. In terms of the diabatic potentials of Eq. (2.18) the latter is given by

$$V_{\Sigma(\Pi)} = \frac{H_\Sigma + H_\Pi}{2}\begin{pmatrix}1 & 0\\ 0 & 1\end{pmatrix} \mp \sqrt{\left(\frac{H_\Sigma - H_\Pi}{2}\right)^2 + H_{\Sigma\Pi}^2}. \tag{2.21}$$

The quantity $\boldsymbol{S}$ in Eq. (2.20) defines an orthogonal transformation matrix. For the present 2×2 Hamiltonian $\boldsymbol{S}$ is given by

$$\boldsymbol{S} = \begin{pmatrix}\cos\alpha & \sin\alpha\\ -\sin\alpha & \cos\alpha\end{pmatrix}, \tag{2.22}$$

where α represents the coordinate dependent adiabatic-to-diabatic transformation angle. Using the diabatic Hamiltonian of Eq. (2.18) and the rotation matrix of Eq. (2.22) one arrives at the following expression of the adiabatic Hamiltonian [33, 34, 121]

$$\begin{aligned}\mathcal{H}^{ad} = {} & T_N\begin{pmatrix}1 & 0\\ 0 & 1\end{pmatrix} + \begin{pmatrix}V_\Sigma & 0\\ 0 & V_\Pi\end{pmatrix} + \left[\frac{\hbar^2}{2\mu}(\alpha_R'^2 + \alpha_r'^2) + \frac{\hbar^2}{2I}\alpha_\gamma'^2\right]\begin{pmatrix}1 & 0\\ 0 & 1\end{pmatrix} + \\ & \left[\frac{\hbar^2}{2\mu}(\alpha_R'' + 2\alpha_R'\frac{\partial}{\partial R} + \alpha_r'' + 2\alpha_r'\frac{\partial}{\partial r}) + \frac{\hbar^2}{2I}(\alpha_\gamma'' + 2\alpha_\gamma'\frac{\partial}{\partial\gamma} + \alpha_\gamma'\cot\gamma)\right]\begin{pmatrix}0 & -1\\ 1 & 0\end{pmatrix},\end{aligned} \tag{2.23}$$

where $\alpha_x' = \partial\alpha/\partial x$ and $\alpha_x'' = \partial^2\alpha/\partial x^2$. The third term in the right hand side of Eq. (2.23) corresponds to the diagonal Born-Huang term [2] and the fourth term corresponds to the off-diagonal derivative coupling term.

2.3.2 A three-state Hamiltonian with electronic and relativistic spin-orbit coupling

The $^2\Sigma$ and $^2\Pi$ states of ClH_2 transform as 1A′, 1A″ and 2A′ species, respectively, in the noncollinear geometry. These states correlate to the $^2\Sigma_{1/2}$, $^2\Pi_{3/2}$ and $^2\Pi_{1/2}$ species at the linear geometry when the SO coupling is considered. In the Cartesian notation of Alexander and coworkers [47] these states can be designated as $|\Sigma\rangle$, $|\Pi_y\rangle$ and $|\Pi_x\rangle$ and in terms of the projection of the electronic orbital angular momentum (signed) along $\vec{R}$ they can be denoted as $|\Sigma\rangle$, $|\Pi_{-1}\rangle$ and $|\Pi_1\rangle$ states, respectively. As described in details in Sec. 1.2.1 the matrix of the electronic interaction potential, in a 6×6 basis defined by the three Cartesian diabatic states and the two possible spin projections can be described in terms of three diagonal, electronically diabatic PESs, as well as a forth PES, which is the coupling between the two states of A' symmetry. In terms of the four diabatic PESs and two SO coupling elements, the matrix of the interaction potential in the signed-λ basis is given by:

$$\mathcal{H}^{el}+\mathcal{H}^{so}=\begin{pmatrix} & |\Sigma\rangle & |\overline{\Sigma}\rangle & |\Pi_1\rangle & |\overline{\Pi}_1\rangle & |\Pi_{-1}\rangle & |\overline{\Pi}_{-1}\rangle \\ |\Sigma\rangle & V_\Sigma & 0 & -V_1 & -\sqrt{2}B & V_1 & 0 \\ |\overline{\Sigma}\rangle & 0 & V_\Sigma & 0 & -V_1 & -\sqrt{2}B & V_1 \\ |\Pi_1\rangle & -V_1 & 0 & V_\Pi - A & 0 & V_2 & 0 \\ |\overline{\Pi}_1\rangle & -\sqrt{2}B & -V_1 & 0 & V_\Pi + A & 0 & V_2 \\ |\Pi_{-1}\rangle & V_1 & -\sqrt{2}B & V_2 & 0 & V_\Pi + A & 0 \\ |\overline{\Pi}_{-1}\rangle & 0 & V_1 & 0 & V_2 & 0 & V_\Pi - A \end{pmatrix} \quad (2.24)$$

where the bar over the states represent the second spin component.

Since the spin states occur in degenerate pairs (Kramer's degeneracy), it is shown that the above Hamiltonian can be decoupled into two 3×3 blocks, in a

complex basis invariant to the time reversal [47]

$$|\Sigma_\epsilon\rangle = \frac{1}{\sqrt{2}}[\epsilon|\overline{\Sigma}\rangle + i|\Sigma\rangle], \tag{2.25a}$$

$$|\Pi_{\pm\epsilon}\rangle = \frac{1}{\sqrt{2}}[\epsilon|\overline{\Pi}_{\pm 1}\rangle + i|\Pi_{\pm 1}\rangle], \tag{2.25b}$$

where $\epsilon = \pm 1$. The matrix of the $\mathcal{H}^{el} + \mathcal{H}^{so}$ then decouples as [47]

$$\mathcal{H}^{el} + \mathcal{H}^{so} = \begin{pmatrix} H & 0 \\ 0 & H^\dagger \end{pmatrix} \tag{2.26}$$

where H is a 3×3 Hermitian matrix in the basis of the three states with $\epsilon = \pm 1$:

$$H = \begin{pmatrix} & |\Sigma\rangle & |\Pi_1\rangle & |\Pi_{-1}\rangle \\ |\Sigma\rangle & V_\Sigma & -V_1 - i\sqrt{2}B & V_1 \\ |\Pi_1\rangle & -V_1 + i\sqrt{2}B & V_\Pi + A & V_2 \\ |\Pi_{-1}\rangle & V_1 & V_2 & V_\Pi - A \end{pmatrix} \tag{2.27}$$

$H^\dagger$ is the Hermitian adjoint of H. All the elements of the above Hamiltonian matrix are provided by the CW PES [75]. We use this Hamiltonian in the dynamical simulations discussed below. At this point we note that it is cumbersome to formulate a unique adiabatic-to-diabatic transformation matrix pertinent to the above 3×3 diabatic Hamiltonian. The S matrix, in this case, can be calculated by numerical diagonalizing the $\mathcal{H}^{el} + \mathcal{H}^{so}$ matrix for each node of the grid. We restrict ourselves to treat the entire dynamics in the diabatic electronic basis. A detailed study on the dynamics in the adiabatic electronic representation is presently under progress.

2.4 Preparation of the initial wave packet

In the reactive scattering study the initial wavefunction is prepared in the asymptotic reagent channel (i.e. $R \to \infty$) where there is no influence of the interaction potential. In the coupled 3× 3 situation, the initial wavefunction can be located in any of the three diabatic PESs. In vector notation, for a particular total angular momentum $\boldsymbol{J}$, the initial wavefunction is given by:

$$|\Psi^J_\Omega(R,r,\gamma,0)\rangle = \Psi^J_{\Omega_1}(R,r,\gamma)\begin{pmatrix}1\\0\\0\end{pmatrix} + \Psi^J_{\Omega_2}(R,r,\gamma)\begin{pmatrix}0\\1\\0\end{pmatrix} + \Psi^J_{\Omega_3}(R,r,\gamma)\begin{pmatrix}0\\0\\1\end{pmatrix}, \tag{2.28}$$

where, $\begin{pmatrix}1\\0\\0\end{pmatrix}$, $\begin{pmatrix}0\\1\\0\end{pmatrix}$ and $\begin{pmatrix}0\\0\\1\end{pmatrix}$ denotes the $^2\Sigma_{1/2}$, $^2\Pi_{3/2}$ and $^2\Pi_{1/2}$ diabatic electronic states, respectively.

The nuclear wave functions for the respective electronic states Ψ_i (i=1,2,3) can be written in terms of the product of the translational wavefunction $F(R)$ for the motion along R, the ro-vibrational wavefunction $\Phi_{vj}(r)$ of the H_2 molecule and $\mathcal{L}^2$-normalized associated Legendre polynomial $\tilde{P}^\Omega_j(\cos\gamma)$ to describe the motion along the approach angle γ,

$$|\Psi^J_{\Omega_i}(R,r,\gamma,0)\rangle = F(R)\Phi_{vj}(r)\tilde{P}^K_j(\cos\gamma_n) \tag{2.29}$$

We choose a minimum uncertainty Gaussian wave packet (GWP) for $F(R)$:

$$F(R) = \left(\frac{1}{2\pi\delta^2}\right)^{\frac{1}{4}} \exp\left[-\frac{(R-R_0)^2}{4\delta^2} - ik_0(R-R_0)\right]. \tag{2.30}$$

The quantity δ is the width parameter of the GWP, and R_0 and k_0 correspond to the location of its maximum in the coordinate and momentum space, respectively. The functions $\Phi_{vj}(r)$ along with the normalized Legendre polynomials ($\sqrt{(2j+1)/2}P_j(\cos\gamma)$) represents the ro-vibrational eigenfunction corresponding to a (v,j) state of the H_2 molecule. The function $\Phi_{vj}(r)$ are obtained by solving the eigenvalue equation of the free H_2 molecule:

$$\left[-\frac{\hbar^2}{2\mu'}\frac{d^2}{dr'^2}+V(r')+\frac{j(j+1)\hbar^2}{2\mu' r'^2}\right]\Phi_{vj}(r')=\epsilon_{vj}\Phi_{vj}(r'). \tag{2.31}$$

Here μ' is the reduced mass, ϵ_{vj} the energy eigenvalue and $r'[=r(\mu/\mu')^{1/2}]$ the unscaled internuclear distance of H_2 molecule. The potential energy of the H_2 molecule $V(r')$ is obtained from the CW PES by setting $R\rightarrow\infty$. We used the sine-DVR approach of Colbert and Miller [122] to solve the above eigenvalue equation. The $\mathcal{L}^2$-normalized associated Legendre polynomials are given by

$$\tilde{P}_j^K(\cos\gamma)=\sqrt{\frac{2j+1}{2}\frac{(j-K)!}{(j+K)!}}P_j^K(\cos\gamma) \tag{2.32}$$

which are the eigenfunctions of the $\hat{j}^2$ operator.

The coordinate grid consists of equally spaced points R_l and r_m along the Jacobi distances R and r, respectively, and the Jacobi angle is chosen as the node of a n-point Gaussian quadrature. The initial wavefunction at each node (R_l,r_m,γ_n) of this grid is given by

$$|\Psi_K^J(R_l,r_m,\gamma_n,t=0)\rangle=|\Psi_{lmn}\rangle=\sqrt{w_n}F(R_l)\phi_{vj}(r_m)\tilde{P}_j^K(\cos\gamma_n). \tag{2.33}$$

where,w_n is the weight of the Gaussian guadrature associated with the grid point n.

2.5 Time evolution of the WP

The general solution of the TDSE [Eq. (2.3)] is given by

$$\Psi(t) = \hat{P} \exp\left[-i\hbar \int_0^T \hat{H}(t')dt'\right] \Psi(0) \tag{2.34}$$

where, $\Psi(0)$ and $\Psi(t)$ are the wavefunctions at time 0 and t, respectively. $\hat{P}$ is the time ordering operator. For an explicitly time-independent Hamiltonian, the solution reads as in Eq. (2.5). The exponential operator in the above forms a continuous dynamical group where time t is a parameter, and is known as the time-evolution operator denoted by $\hat{U}(t, t_0)$ [123]. For $t_0 = 0$, $\hat{U}(t, t_0) = e^{-i\hat{H}t/\hbar}$. Time t is sliced in smaller steps of length Δt and the time-evolution for the entire range of time is accomplished through:

$$\hat{U}(t) \;=\; \Pi_{n=0}^{N_t-1} \hat{U}((n+1)\Delta t, n\Delta t) \tag{2.35}$$

where, N_t is the total number of time-evolution steps and $\Delta t = t/N_t$.

In quantum molecular dynamics, there are several approximate methods to propagate the WP in time. Some of these methods are the split-operator method [103,104], Chebyshev polynomials (CP) scheme [124,125], second-order differencing (SOD) [98,126], symplectic integrator (SI) [127] and real WP [128] method. Short-iterative Lanczos (SIL) [129] method is also used explicitly for the time-independent Hamiltonians. All these methods vary in terms of their performance and accuracy. For the present problem, we have used the second order split-operator method [104] for the time propagation of the initial WP.

In the application of the evoluation operator to solve Schrödinger Equation (c.f. Eq. 2.5), there is an error arising from the fact that kinetic and potential

energy operators do not commute. However, by splitting the time evoluation operator symmetrically the commutator error is reduced to third order. Such an approach is known as the second-order split-operator scheme [130]. It can be either potential referenced or kinetic referenced. The potential referenced second-order split-operator scheme is given by:

$$e^{-i\hat{H}\Delta t/\hbar} = e^{-i\hat{T}\Delta t/2\hbar}e^{-i\hat{V}\Delta t/\hbar}e^{-i\hat{T}\Delta t/2\hbar} + O(\Delta t^3). \tag{2.36}$$

In the kinetic-referenced split-operator scheme the exponential containing the potential-energy operator is symmetrically split and the kinetic-energy is sandwiched in between. The time evolution of the WP in the potential-referenced scheme is given by

$$\begin{aligned} \Psi(t+\Delta t) &= e^{-i\hat{T}\Delta t/2\hbar}e^{-i\hat{V}\Delta t/\hbar}e^{-i\hat{T}\Delta t/2\hbar}\Psi(t) \\ &= Q\Psi(t) \end{aligned} \tag{2.37}$$

The norm conservation of the state leads to the probability conservation during time-evolution, which demands the operator $\hat{U}$ is linear and unitary:

$$\hat{U}\hat{U}^\dagger = \hat{U}^\dagger\hat{U} = 1. \tag{2.38}$$

It is clear from the above expression that the split-operator scheme is unitary and the norm of WP is therefore conserved. However, the energy conservation fails in this scheme due to the noncommutability of the potential and kinetic energy operators. To obtain comparatively accurate results, an optimum time step is

selected based on the maximum potential energy on the grid [98, 104].

$$\Delta t < \frac{\pi}{3\Delta V_{max}}, \quad \Delta V_{max} = V_{max} - V_{min}. \tag{2.39}$$

In the present case, the exponential operator with the 3×3 Hamiltonian [c.f. Eq. 2.27], can be expanded as:

$$\begin{aligned} \exp\left[\frac{-i\mathcal{H}^d\Delta t}{\hbar}\right] &= \exp\left[\frac{-iH\Delta t}{2\hbar}\right]\exp\left[\frac{-i\boldsymbol{j}^2\Delta t}{4I\hbar}\mathbf{1}\right]\exp\left[\frac{-iT(R,r)\Delta t}{\hbar}\mathbf{1}\right] \\ &\quad \times \exp\left[\frac{-i\boldsymbol{j}^2\Delta t}{4I\hbar}\mathbf{1}\right]\exp\left[\frac{-iH\Delta t}{2\hbar}\right] + O[(\Delta t)^3], \end{aligned} \tag{2.40}$$

where $T(R,r) = (P_R^2 + P_r^2)/2\mu$ is the total radial kinetic energy operator. $\mathbf{1}$ represents a 3×3 unit matrix. The relativistic electronic Hamiltonian H [Eq. (2.27)] can be decomposed as

$$\begin{aligned} H &= \begin{pmatrix} V_\Sigma & 0 & 0 \\ 0 & V_\Pi + A & 0 \\ 0 & 0 & V_\Pi - A \end{pmatrix} - V_1 \begin{pmatrix} 0 & 1 & 0 \\ 1 & 0 & 0 \\ 0 & 0 & 0 \end{pmatrix} + \\ &\quad \sqrt{2}B \begin{pmatrix} 0 & -i & 0 \\ i & 0 & 0 \\ 0 & 0 & 0 \end{pmatrix} + V_1 \begin{pmatrix} 0 & 0 & 1 \\ 0 & 0 & 0 \\ 1 & 0 & 0 \end{pmatrix} + V_2 \begin{pmatrix} 0 & 0 & 0 \\ 0 & 0 & 1 \\ 0 & 1 & 0 \end{pmatrix} \end{aligned} \tag{2.41}$$

Since the diagonal and the off-diagonal parts of the above electronic Hamiltonian do not commute with each other the propagator containing it in Eq. (2.40) is

further splitted as

$$\begin{aligned}
\exp\left[-iH\frac{\Delta t}{2\hbar}\right] &= \exp\left[-i\begin{pmatrix} V_\Sigma & 0 & 0 \\ 0 & V_\Pi + A & 0 \\ 0 & 0 & V_\Pi - A \end{pmatrix}\frac{\Delta t}{4\hbar}\right] \exp\left[iV_1\begin{pmatrix} 0 & 1 & 0 \\ 1 & 0 & 0 \\ 0 & 0 & 0 \end{pmatrix}\frac{\Delta t}{2\hbar}\right] \\
&\quad \times \exp\left[-i\sqrt{2}B\begin{pmatrix} 0 & -i & 0 \\ i & 0 & 0 \\ 0 & 0 & 0 \end{pmatrix}\frac{\Delta t}{2\hbar}\right] \exp\left[-iV_1\begin{pmatrix} 0 & 0 & 1 \\ 0 & 0 & 0 \\ 1 & 0 & 0 \end{pmatrix}\frac{\Delta t}{2\hbar}\right] \times \\
&\quad \exp\left[-iV_2\begin{pmatrix} 0 & 0 & 0 \\ 0 & 0 & 1 \\ 0 & 1 & 0 \end{pmatrix}\frac{\Delta t}{2\hbar}\right] \exp\left[-i\begin{pmatrix} V_\Sigma & 0 & 0 \\ 0 & V_\Pi + A & 0 \\ 0 & 0 & V_\Pi - A \end{pmatrix}\frac{\Delta t}{4\hbar}\right]
\end{aligned}$$

The exponent containing the off-diagonal matrix elements is now expressed in terms of the Pauli matrices [131]

$$\begin{aligned}
\exp\left[-i(-V_1)\begin{pmatrix} 0 & 1 & 0 \\ 1 & 0 & 0 \\ 0 & 0 & 0 \end{pmatrix}\frac{\Delta t}{2\hbar}\right] &= \begin{pmatrix} \cos(-V_1\Delta t/2\hbar) & -i\sin(-V_1\Delta t/2\hbar) & 0 \\ -i\sin(-V_1\Delta t/2\hbar) & \cos(-V_1\Delta t/2\hbar) & 0 \\ 0 & 0 & 0 \end{pmatrix}, \\
\exp\left[-i\sqrt{2}B\begin{pmatrix} 0 & -i & 0 \\ i & 0 & 0 \\ 0 & 0 & 0 \end{pmatrix}\frac{\Delta t}{2\hbar}\right] &= \begin{pmatrix} \cos(\sqrt{2}B\Delta t/2\hbar) & -\sin(\sqrt{2}B\Delta t/2\hbar) & 0 \\ -\sin(\sqrt{2}B\Delta t/2\hbar) & \cos(\sqrt{2}B\Delta t/2\hbar) & 0 \\ 0 & 0 & 0 \end{pmatrix}, \\
\exp\left[-iV_1\begin{pmatrix} 0 & 0 & 1 \\ 0 & 0 & 0 \\ 1 & 0 & 0 \end{pmatrix}\frac{\Delta t}{2\hbar}\right] &= \begin{pmatrix} \cos(V_1\Delta t/2\hbar) & 0 & -i\sin(V_1\Delta t/2\hbar) \\ 0 & 0 & 0 \\ -i\sin(V_1\Delta t/2\hbar) & 0 & \cos(V_1\Delta t/2\hbar) \end{pmatrix} \text{ and} \\
\exp\left[-iV_2\begin{pmatrix} 0 & 0 & 0 \\ 0 & 0 & 1 \\ 0 & 1 & 0 \end{pmatrix}\frac{\Delta t}{2\hbar}\right] &= \begin{pmatrix} 0 & 0 & 0 \\ 0 & \cos(V_2\Delta t/2\hbar) & -i\sin(V_2\Delta t/2\hbar) \\ 0 & -i\sin(V_2\Delta t/2\hbar) & \cos(V_2\Delta t/2\hbar) \end{pmatrix}.
\end{aligned}$$

The Eq. (2.40) is used in conjunction with the fast Fourier transform method [102] to evaluate the action of the exponential containing the radial kinetic energy operator. The action of the rotational kinetic energy operator is carried out by transforming the DVR wavefunction, $|\Psi_{lmn}\rangle$, [Eq. (2.33)] to the angular momentum space (FBR), multiplying it by the diagonal value of the operator ($\mathrm{e}^{-ij(j+1)\Delta t\hbar/4I}$), and transforming it back to the DVR representation [112]. Numerically this is accomplished in a single step [132, 133]:

$$\exp\left[\frac{-i\boldsymbol{j}^2\Delta t}{4I\hbar}\right]|\Psi_{lmn'}\rangle = \sum_n \left\{\sum_j \boldsymbol{T}^{\dagger}_{n',j} e^{-ij(j+1)\Delta t\hbar/4I}\boldsymbol{T}_{j,n}\right\}|\Psi_{lmn}\rangle, \qquad (2.42)$$

where, j is the rotational quantum number of the H_2 molecule. The coefficients $\boldsymbol{T}_{j,n}$ are the elements of the DVR-FBR transformation matrix, constructed in terms of Legendre polynomials (eigenfunctions of the $\boldsymbol{j}^2$ operator for $\boldsymbol{J} = 0$) [109, 110, 132]:

$$\boldsymbol{T}_{j,n} = \sqrt{w(n)}\sqrt{\frac{2j+1}{2}}P_j(\cos\gamma_n), \qquad (2.43)$$

and $\boldsymbol{T}^{\dagger}_{n,j}$ are the elements of the inverse transformation matrix, i.e., the Hermitian conjugate to $\boldsymbol{T}_{j,n}$.

As the WP moves forward in time, its fast moving components approach the grid boundaries and are no longer relevant for the rest of the dynamics [134]. Therefore, to avoid unphysical reflections or wrap around of these components from the boundaries of a finite sized grid, the WP at each time step is multiplied by a damping function [135]

$$f(X_i) = \sin\left[\frac{\pi}{2}\frac{(X_{mask} + \Delta X_{mask} - X_i)}{\Delta X_{mask}}\right], \qquad X_i \geq X_{mask} \qquad (2.44)$$

which is activated outside the dividing line in the product channel and also in the

asymptotic reactant channel. X_{mask} is the point at which the damping function is initiated and $\Delta X_{mask}(= X_{max} - X_{mask})$ is the width of X over which the function decays from 1 to 0, with X_{max} being the maximum value of X in that direction, in a particular channel.

2.6 Final analysis (Flux Operator approach)

The flux operator $\hat{F}$ is most generally defined in terms of a dividing surface Θ, which is a function of the reaction coordinate x that separates the products from the reactants [136]

$$\hat{F} = \frac{i}{\hbar}\left[\mathcal{H}^d, \Theta\right]. \tag{2.45}$$

In the present case the obvious choice for Θ is given by $\Theta = h(x - x_d)$, where h is the Heaviside step function which equals to unity for positive argument and zero otherwise. x_d is the dividing surface which is to be chosen far out in the product channel to ensure the asymptotic motion for all $x \geq x_d$. Since Θ depends only on coordinates it commutes with the electronic part of the Hamiltonian and Eq. (2.45) becomes

$$\hat{F} = \frac{i}{\hbar}\left[T_N, \Theta\right]. \tag{2.46}$$

The quantity T_N represents the nuclear kinetic energy part of the Hamiltonian.

The quantum flux operator [Eq. (2.46)] is diagonal in the diabatic electronic representation. Taking the value of Θ as, $\Theta = h(r - r_d)$, the non-zero diagonal elements of the flux operator take the form [33, 136, 137]

$$\hat{f}_{ii} = \frac{-i\hbar}{2\mu}\left[\frac{\partial}{\partial r}\delta(r - r_d) + \delta(r - r_d)\frac{\partial}{\partial r}\right]. \tag{2.47}$$

In order to calculate the reaction probability in the two-state adiabatic elec-

tronic basis, the flux operator needs to be represented in this basis. As the quantity Θ in the Flux operator depends only on the reaction coordinate (r), the r-dependent part of the nuclear kinetic energy operator is of only relevance in Eq. (2.45). The latter is non-diagonal in the adiabatic basis and is given by

$$T_r^{ad} = \frac{-\hbar^2}{2\mu} \begin{pmatrix} \frac{\partial^2}{\partial r^2} - \alpha_r'^2 & (\alpha_r'' + 2\alpha_r' \frac{\partial}{\partial r}) \\ -(\alpha_r'' + 2\alpha_r' \frac{\partial}{\partial r}) & \frac{\partial^2}{\partial r^2} - \alpha_r'^2 \end{pmatrix}. \tag{2.48}$$

One arrives at the same expression as in Eq. (2.47) for the diagonal elements of the flux operator and its off-diagonal elements take the following form [33]

$$\hat{f}_{12} = -\hat{f}_{21} = \frac{-i\hbar\alpha_r'}{\mu}\delta(r - r_d). \tag{2.49}$$

The reaction probability is obtained from the expectation value of this flux operator in the basis of the energy normalized time-independent wavefunction [136].

2.6.1 Calculation of reaction probability

The reaction probability is defined as the expectation value of this flux operator in the basis of energy normalized time-independent reactive scattering wavefunction at the dividing surface. In the diabatic basis, the initial state i (corresponding to a specific vibrational ν and rotational j state of the reagent H_2) selected and energy resolved reaction probability (summed over final states $f(v', j')$ of the product HCl) is given by

$$P_i^R(E) = \sum_f |S_{fi}^R|^2 = \left\langle \Phi^d(R, r_d, \gamma, E)|\hat{F}|\Phi^d(R, r_d, \gamma, E) \right\rangle, \tag{2.50}$$

where S_{fi}^R is the reactive scattering matrix from an initial state (i) of the reactant to a final state (f) of the product. In the two state model, where only the electronic coupling is considered in the dynamics, the wave function in the diabatic basis can be written as the components of the two electronic states,

$$|\Phi^d(R, r_d, \gamma, E)\rangle = \begin{pmatrix} |\phi_1^d(R, r_d, \gamma, E)\rangle \\ |\phi_2^d(R, r_d, \gamma, E)\rangle \end{pmatrix}, \tag{2.51}$$

where ϕ_1^d and ϕ_2^d correspond to the wavefunction components on the diabatic state H_Σ and H_Π, respectively. The function $|\phi_k^d(R, r_d, \gamma, E)\rangle$ is obtained by Fourier transforming the time-evolved wave packet $|\psi_k^d(R, r, \gamma, t)\rangle$ along the dividing surface at r = r_d followed by the energy normalization as

$$|\phi_k^d(R, r_d, \gamma, E)\rangle = \frac{1}{\sqrt{2\pi}} \frac{1}{\kappa_E} \int_{-\infty}^{+\infty} e^{iEt/\hbar} |\psi_k^d(R, r, \gamma, t)\rangle dt|_{r=r_d}. \tag{2.52}$$

For a given total energy E the quantity κ_E is the weight of the translational component, $F(R)$, of the initial wave packet,

$$\kappa_E = \left(\frac{\mu}{2\pi\hbar k}\right)^{1/2} \int_{-\infty}^{+\infty} F(R) e^{ikR} dR, \tag{2.53}$$

where, $k = \sqrt{2\mu(E-\epsilon)}/\hbar$, with ϵ_{vj} being the initial ro-vibrational energy of the H_2 molecule.

In terms of ϕ_1^d and ϕ_2^d the above expression can be rewritten as [33]

$$\begin{aligned} P_i^R(E) &\approx \sum_{k=1}^{2} \left\langle \phi_k^d(R, r_d, \gamma, E) | \hat{f}_{kk} | \phi_k^d(R, r_d, \gamma, E) \right\rangle, \\ &\approx \frac{\hbar}{\mu} \sum_{k=1}^{2} \mathrm{Im} \left[\left\langle \phi_k^d(R, r_d, \gamma, E) | \frac{\partial \phi_k^d(R, r_d, \gamma, E)}{\partial r} \right\rangle \right] |_{r=r_d}. \end{aligned} \tag{2.54}$$

The quantity in the right hand side of the above equation is integrated over the entire range of R and γ in order to obtain the reaction probability.

Contrary to the analogous expression [Eq. (2.54)] in the diabatic basis, the result in the adiabatic basis contains also off-diagonal electronic contributions. The reaction probability in this basis is given by [33]

$$\begin{aligned} P_i^R(E) &= \frac{\hbar}{\mu}\left[\mathrm{Im}\langle\phi_1^{ad}(R,r_d,\gamma,E)|\frac{\partial\phi_1^{ad}(R,r_d,\gamma,E)}{\partial r}\rangle\right] \\ &+ \frac{\hbar}{\mu}\left[\mathrm{Im}\langle\phi_2^{ad}(R,r_d,\gamma,E)|\frac{\partial\phi_2^{ad}(R,r_d,\gamma,E)}{\partial r}\rangle\right] \\ &+ 2\mathrm{Im}\langle\phi_1^{ad}(R,r_d,\gamma,E)|\alpha_r'|\phi_2^{ad}(R,r_d,\gamma,E)\rangle. \end{aligned} \tag{2.55}$$

These off-diagonal terms in the reaction probability expression are expected to play an important role when both channels, corresponding to V_Σ and V_Π are open. If only V_Σ is open, then the first of the three terms on the right hand side of Eq. (2.55) contributes to the reaction probability only. Even in this case, however, both terms in the diabatic analogue of Eq. (2.55) may play a role, because adiabatic and diabatic states need not coincide asymptotically.

We restrict ourselves to the diabatic electronic basis in the three-state model when both electronic and SO coupling are considered in the dynamics. Defining the energy normalized time-independent diabatic wavefunction in this basis as

$$|\Phi^d(R,r_d,\gamma,E)\rangle = \begin{pmatrix} |\phi_1^d(R,r_d,\gamma,E)\rangle \\ |\phi_2^d(R,r_d,\gamma,E)\rangle \\ |\phi_3^d(R,r_d,\gamma,E)\rangle \end{pmatrix}, \tag{2.56}$$

the reaction probability is given by [33, 34]

$$\begin{aligned} P_i^R(E) &\approx \sum_{k=1}^{3} \left\langle \phi_k^d(R, r_d, \gamma, E) | \hat{f}_{kk} | \phi_k^d(R, r_d, \gamma, E) \right\rangle, \\ &\approx \frac{\hbar}{\mu} \sum_{k=1}^{3} \mathrm{Im} \left[\left\langle \phi_k^d(R, r_d, \gamma, E) | \frac{\partial \phi_k^d(R, r_d, \gamma, E)}{\partial r} \right\rangle \right] |_{r=r_d}. \end{aligned} \quad (2.57)$$

where, ϕ_1^d, ϕ_2^d and ϕ_3^d represent the wavefunction components on the $|\Sigma\rangle$, $|\Pi_{3/2}\rangle$ and $|\Pi_{1/2}\rangle$ state, respectively.

2.6.2 Calculation of integral reaction cross section and thermal rate constant

The reaction probabilities depending upon J and Ω values [cf. Eq. (2.54 or 2.55)] are summed up to calculate the integral reaction cross section for a specified initial (v, j) state of ClHD.

$$\sigma_{vj}(E) = \frac{\pi}{k_{vj}^2} \sum_{\Omega=0}^{j} \frac{1}{(2j+1)} \sum_{J \geq \Omega}^{J_{max}} (2J+1) P_{vj}^{J\Omega}(E). \quad (2.58)$$

The initial state-selected thermal rate constant is calculated from the total integral reaction cross section [138],

$$K_{vj}(T) = \sqrt{\frac{8K_BT}{\pi\mu}} \frac{1}{(K_BT)^2} \int_0^\infty E\sigma_{vj}(E) e^{-E/K_BT} dE, \quad (2.59)$$

where K_B is the Boltzmann constant. Finally, the rotationally averaged thermal rate constants can be obtained by averaging over a Boltzmann distribution of

such states

$$K_v(T) \;=\; \sum_j \frac{K_{vj}(E)}{Q_{rot}}(2j+1)e^{-Bj(j+1)hc/K_BT}, \tag{2.60}$$

where B is the rotational constant of the reagent and
Q_{rot} $(= \sum_j (2j+1)e^{-Bj(j+1)hc/K_BT})$ is the rotational partition function.

Chapter 3

Quantum wave packet dynamics of Cl + H_2 (HD) reaction

3.1 Introduction

Quantum dynamical results of Cl(^2P) + H_2 (HD) reaction obtained with the formalism outlined in Chapter 2 are presented and discussed in this Chapter. The total reaction probabilities obtained on the uncoupled $^2\Sigma$ adiabatic electronic state of the Cl(^2P) + H_2 reaction is shown first as a function of the total energy E (atom-diatom translational + diatomic rovibrational). The effect of electronic coupling on the reaction attributes is considered thereafter. Here the role of conical intersections between the $^2\Sigma$ and $^2\Pi$ electronic states is examined with a two-state model considering electronic coupling in the dynamics, as detailed in Sec. 2.3.1. Following the earlier literature, [79, 139, 140] we neglect the electronic angular momentum in the two-state approximation and also in the uncoupled surface calculations. Therefore, these calculations correspond to the lowest value of the total angular momentum $J = 0$. In the couple state model, the initial WP

is prepared in the adiabatic electronic state and then transformed to the diabatic electronic representation before propagation. The final reaction probability is calculated both in the adiabatic as well as diabatic electronic representation. The electronic population dynamics and the probability of density of the WP during the course of propagation is also studied in order to understand the mechanistic details of the nuclear dynamics on the coupled manifold of electronic states.

This study is extended to a coupled three-state model (c.f. Chapter 2) by including the relativistic SO interactions in the dynamics along with the electronic coupling. We resort to a diabatic electronic representation throughout this model. The dynamics is investigated for the lowest value of the total angular momentum, $J = 0.5$, employing six diabatic electronic PESs as discussed in Sec 2.3.2. The reactivity of the different SO states of $Cl(^2P) + H_2$ reaction obtained by initiating the reaction on the $^2\Sigma_{1/2}$, $^2\Pi_{3/2}$ and $^2\Pi_{1/2}$ diabatic states separately including both electronic and SO coupling in the dynamics.

Finally, the reaction probabilities of $Cl(^2P) + H_2$ and $Cl(^2P) + HD$ reactions for $J \neq 0$ are calculated. The preliminary results obtained on the channel specific integral reaction cross sections in the uncoupled and coupled states situations are shown and compared with the available experimental results. The Boltzmann averaged thermal rate constants are also shown and compared with the available experimental results. We note that in the coupled three states model, the initial WP in the reactive scattering process ideally needs to be prepared in the adiabatic electronic representation. This requires the suitable adiabatic-to-diabatic transformation matrix. We have recently designed such matrices by numerically diagonalizing the diabatic electronic Hamiltonian. The effect of the diabatic to adiabatic transformation on the reaction dynamics is presently being examined.

3.2 Computational Details

The detailed theoretical framework and computational methodology to treat the reaction dynamics by the TDQM approach is outlined in Chapter 2. We describe below the details of the numerical parameters used in the calculations.

A coordinate grid consisting of 128×64×48 points in the R, r and γ space with R ranging between 0.10 a_0 and 14.0 a_0 and r between 0.10 a_0 and 8.0 a_0 is constructed. The grid along γ is taken as the nodes of a 48-point Gauss-Legendre quadrature (GLQ) [141]. The initial WP is prepared at R_0=10.0 a_0 and the width parameter of the GWP, δ is chosen to be 0.18 a_0. The WP is time propagated with a step size Δt of 0.1347 fs for a total time of 204.8 fs. In order to avoid unphysical reflections or wrap arounds of the fast moving components of the WP at the grid boundaries, it is multiplied by a damping function [135] at each time step which is activated outside the dividing line at r=5.14 a_0 in the product channel and also in the asymptotic reactant channel at R=10.51 a_0. The convergence of the calculations is explicitly checked by performing several test calculations by varying the grid parameters noted above. Particularly, the results show some variation of a smaller grid ($0 < 48$ points) is used along the angle γ. The oscillations in the reaction probability curves increase at high energies on reducing the number of angular grid points. We noticed that increasing the width of the absorbing region by a factor of two in either direction does not alter the final results. In the section below, we present and discuss the dynamical results obtained on the Cl(^2P) + H_2 reaction using the numerical parameters described above.

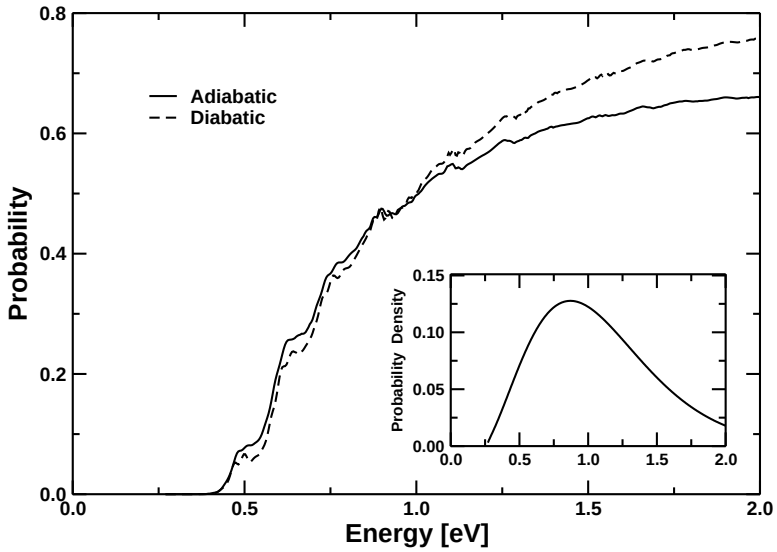

Figure 3.1: Total reaction probability (summed over the product vibrational and rotational states) of the $Cl(^2P) + H_2$ (v=0, j=0) = HCl ($X^1\Sigma_g$) + H (^2S) reaction on the uncoupled $^2\Sigma$ adiabat (solid line) and diabat (dashed line) of the CW potential energy surface (Ref [80, 81]), for the total angular momentum $\boldsymbol{J} = 0$. The reaction probability is plotted as a function of total energy E (Cl, H_2 translational + H_2 ro-vibrational). The energy E is measured relative to H_2 potential minimum. The energy distribution of the initial translational GWP is shown in the inset.

3.3 Result and Discussion

3.3.1 Reaction Probability for total angular momentum $J = 0$

The total probability [summed over all open vibrational (v') and rotational (j') states of the product HCl at a given energy] of Cl(^2P) + H_2 (v=0, j=0) reaction on the uncoupled $^2\Sigma$ PES, as a function of the total energy E (Cl-H_2 translational plus H_2 ro-vibrational) is shown in Fig. 3.1. The $^2\Sigma$ PES correlates with the products, HCl ($\tilde{X}^2\Sigma_g^+$) + H (^2S), in their electronic ground state. The reaction probabilities obtained on the uncoupled adiabatic and diabatic $^2\Sigma$ PES are shown by the solid and dashed lines, respectively. The energy distribution of the initial translational GWP is shown in the inset. It can be seen that the translational components of the initial WP cover the range of energies being investigated here and one may expect to reliably obtain the reaction probabilities in this energy range. Both the uncoupled adiabatic and diabatic probabilities reveal the signature of quasibound resonance formation in the reaction. Some of these resonances are identified and characterized in terms of their eigenvalue, eigenfunction and lifetime and are discussed in detail in Chapter 4. The adiabatic and diabatic surfaces coincide at the collinear arrangement of the three nuclei, however, the two reaction probabilities differ due to some differences of these surfaces at the non-collinear geometries. Single surface dynamics on the $^2\Pi$ adiabat as well as $^2\Pi$ diabat revealed no reaction in this energy range. The $^2\Pi$ state correlates with the electronically excited products HCl ($a^3\Pi$) + H(^2S) at very high energies [c.f. Fig. 1.1]. Therefore, the $^2\Sigma$ PES is expected to be the main contributor to the adiabatic dynamics of Cl(^2P) + H_2 reaction at low and moderate collision energies.

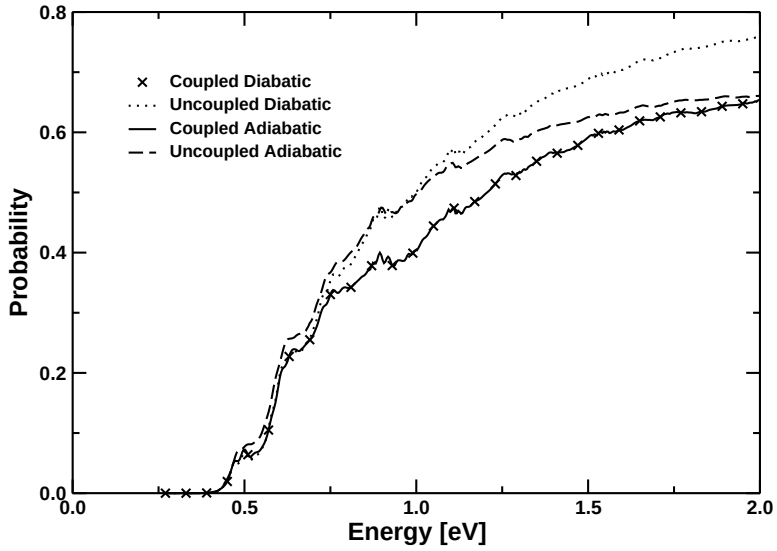

Figure 3.2: Same as Fig. 3.1. The solid line indicates the reaction probability obtained in the coupled ($^2\Sigma$ - $^2\Pi$ electronic) two-state picture. In the coupled state calculations the initial WP is prepared on the $^2\Sigma$ adiabat. The reaction probabilities obtained by analyzing the reactive flux on the adiabatic (Eq. 2.55) and the diabatic (Eq. 2.54) electronic representation are shown by the solid line and the crosses, respectively. The uncoupled $^2\Sigma$ adiabatic and diabatic state results of Fig. 3.1 are included as dotted and dashed lines, respectively, for comparison.

As discussed in the preceding sections that there are two important surface coupling mechanisms, *viz.* the Σ-Π electronic coupling and the Σ-Π and Π-Π SO couplings, expected to contribute to the reactivity of the $^2\Pi$ surface via nonadiabatic transition to the $^2\Sigma$ electronic state. In the following, we first focus on the effect of Σ-Π electronic coupling on the Cl(^2P) + H_2 reaction dynamics.

3.3.2 Nonadiabatic effects due to Electronic Coupling

The coupled two-state model described in section 2.3.1 has been utilized for this purpose. In Fig. 3.2, we show the probability of the Cl(^2P) + H_2 ($v = 0$, $j = 0$) → HCl ($\Sigma v', \Sigma j'$)+ H reaction obtained in this coupled state picture by the solid line. The coupled state results are obtained by preparing the initial WP in the asymptotic reagent channel of the $^2\Sigma$ electronic state in the adiabatic representation. This initial WP is then transformed to the diabatic electronic basis using the transformation matrix of Eq. (2.22). The adiabatic-to-diabatic mixing angle ϕ is defined with the aid of a two-state diabatic electronic Hamiltonian [cf. Eq. (2.18)] as

$$\tan(2\phi) = \frac{2\mathcal{H}_{\Sigma\Pi}}{(\mathcal{H}_{\Sigma\Sigma} - \mathcal{H}_{\Pi\Pi})} \ . \tag{3.1}$$

The propagation of the WP is carried out in the diabatic electronic representation and the reaction probability is calculated both in the adiabatic [cf. Eq. (2.55)] as well as in the diabatic [cf. Eq. (2.54)] electronic representation. The final reaction probability results calculated in either representations must be identical for a given initial WP. In order to verify this we show in Fig. 3.2 the reaction probability calculated using Eq. (2.55) as solid line and those calculated using Eq. (2.54) as crosses. We find that only the first term of either Eq. (2.55) or Eq. (2.54) contributes to the reaction probability. This is in accord with the

nonreactive nature of the $^2\Pi$ surface in the energy range of the present investigations. In order to clearly reveal the impact of the Σ-Π conical intersections on the reaction probability, we also include the uncoupled adiabatic and diabatic results of Fig. 3.1 in Fig. 3.2 and show them by long and short-dashed lines, respectively. It can be seen from Fig. 3.2 that the resonance structures and their energetic locations in the uncoupled and coupled-state results remain nearly the same. At low energies, the uncoupled and coupled-state results show only minor differences. This statement is more appropriate when the uncoupled state results with the diabatic initial packet is considered. The difference between the two results becomes prominent beyond ~ 0.7 eV only. The onset of the reaction remains at ~ 0.43 eV in both the uncoupled and coupled state results. We note that we find the coupled state results with a diabatic initial packet is exactly identical to the uncoupled diabatic results.

3.3.3 Time-dependent dynamics

In order to better understand the uncoupled and coupled state results of Fig. 3.2, we show in Fig. 3.3 the time evolution of the adiabatic and diabatic electronic populations in the coupled state situation. The adiabatic electronic populations can be calculated either by using the $\boldsymbol{S}$ matrix of Eq. (2.22) or by defining suitable adiabatic projection operators. The $\boldsymbol{S}$ matrix is a double valued function of the coordinate and possesses a branch point at the conical intersection [29–31]. This is circumvented by using adiabatic projectors in the diabatic electronic

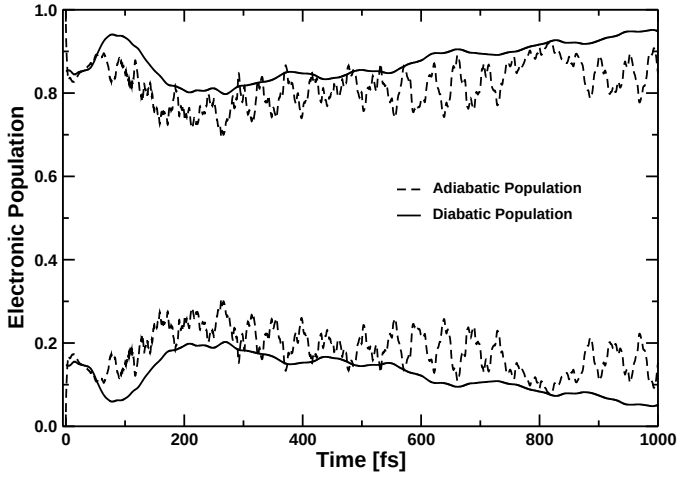

Figure 3.3: Time dependence of the electronic populations in the Σ-Π coupled two-state dynamics of Fig. 3.2. The initial WP is located on the $^2\Sigma$ adiabat. The adiabatic and diabatic electronic populations are shown by the dashed and solid lines, respectively. The upper two curves represent populations of the $^2\Sigma$ state where as the lower ones to that of the $^2\Pi$ state.

representation [121]

$$\begin{aligned} P_{\Sigma}^{ad} &= \boldsymbol{S} \begin{pmatrix} 1 & 0 \\ 0 & 0 \end{pmatrix} \boldsymbol{S}^{\dagger} \\ &= \frac{1}{2} - \frac{1}{2(\Delta^2 + \mathcal{H}_{\Sigma\Pi}^2)^{1/2}} \begin{pmatrix} -\Delta & \mathcal{H}_{\Sigma\Pi} \\ \mathcal{H}_{\Sigma\Pi} & \Delta \end{pmatrix} \\ P_{\Pi}^{ad} &= 1 - P_{\Sigma}^{ad} \end{aligned} \tag{3.2}$$

where the quantity Δ is half of the energy gap between the two diabatic surfaces. The expectation values of the above projectors define the electronic populations in the respective electronic states. The two curves in the upper part of Fig. 3.3 represent the adiabatic (dashed-line) and diabatic (solid-line) population of the $^2\Sigma$ electronic state. Since the initial WP is located in the

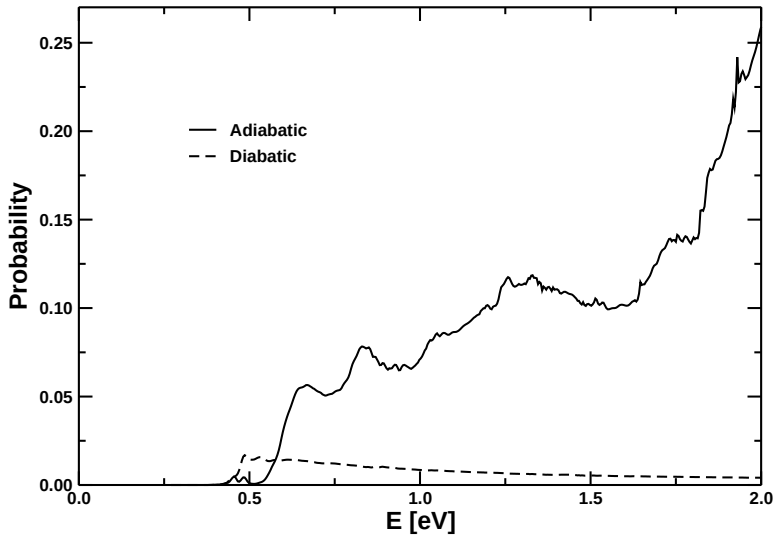

Figure 3.4: The total probability of the $Cl(^2P) + H_2 \rightarrow HCl(\ \Sigma v',\ \Sigma j') + H$ reaction calculated with the coupled two-state model by locating the wave packet initially on the $^2\Pi$ adiabat (solid line) and diabat (dashed line).

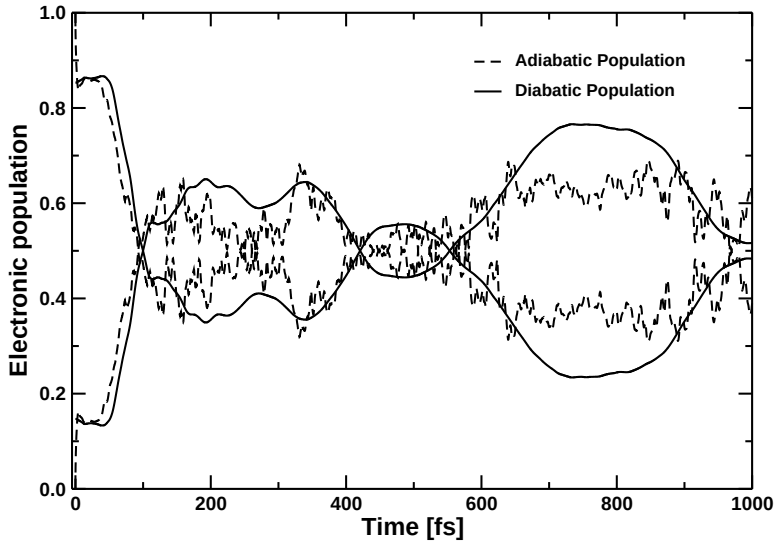

Figure 3.5: Time dependence of the electronic populations in the coupled state dynamics of Fig. 3.4. The initial WP is located on the $^2\Pi$ adiabat. The adiabatic and diabatic electronic populations are shown by the dashed and solid lines, respectively. The upper two curves represent the populations of the $^2\Pi$ state where as the lower ones to that of the $^2\Sigma$ state.

asymptotic reagent channel of the $^2\Sigma$ adiabat, the population of this state is 1.0 and that of $^2\Pi$ adiabat is 0.0 at t=0. These populations represent the fractional electronic populations. An initial sharp decay of the $^2\Sigma$ adiabatic population to within $\sim$ 10 fs is followed by quasi-periodic recurrences can be seen from the figure. The population of the $^2\Pi$ adiabat, on the other hand, reveals an initial growth followed by quasi-periodic recurrences. It is evident from Fig. 3.3 that upto a maximum of $\sim$ 25% of the WP flux flows to the $^2\Pi$ adiabat, a part of which moves back and forth between the two states during the reaction, which results into the appearance of beat-like structures in the population curves. The initial location of the WP corresponds to an admixture of the two diabatic states. Therefore, a 83% (17%) population of the $^2\Sigma$ ($^2\Pi$) diabatic state is obtained at t=0. In about 100 fs a major fraction of the WP flux on the $^2\Pi$ diabat flows back to the $^2\Sigma$ diabat through the seam of conical intersections. The population of the $^2\Pi$ diabat grows again due to recrossing of the WP through the conical intersection. The damping of recurrences in the diabatic population curves is caused by the dephasing of the WP which seems to result from the anharmonicity originating from the "cusp" like behavior of the adiabatic PESs at the conical intersection as well as from the interference effects due to recrossing of the WP through the conical intersection in the diabatic picture.

The $^2\Pi$ state of Cl(^2P) + H_2 is nonreactive in the adiabatic limit. However, the nonadiabatic effects associated with the Σ-Π electronic coupling induces reactivity of the $^2\Pi$ surface via an indirect mechanism. In order to examine this we show in Fig. 3.4 the probability of Cl(^2P) + H_2(v=0,j=0) reaction initiating on the $^2\Pi$ electronic state. The results obtained with the adiabatic and diabatic initial WP are shown by solid and dashed lines, respectively. The WP prepared on the $^2\Pi$ state first transits to the $^2\Sigma$ state (driven by the nonadiabatic effects due to

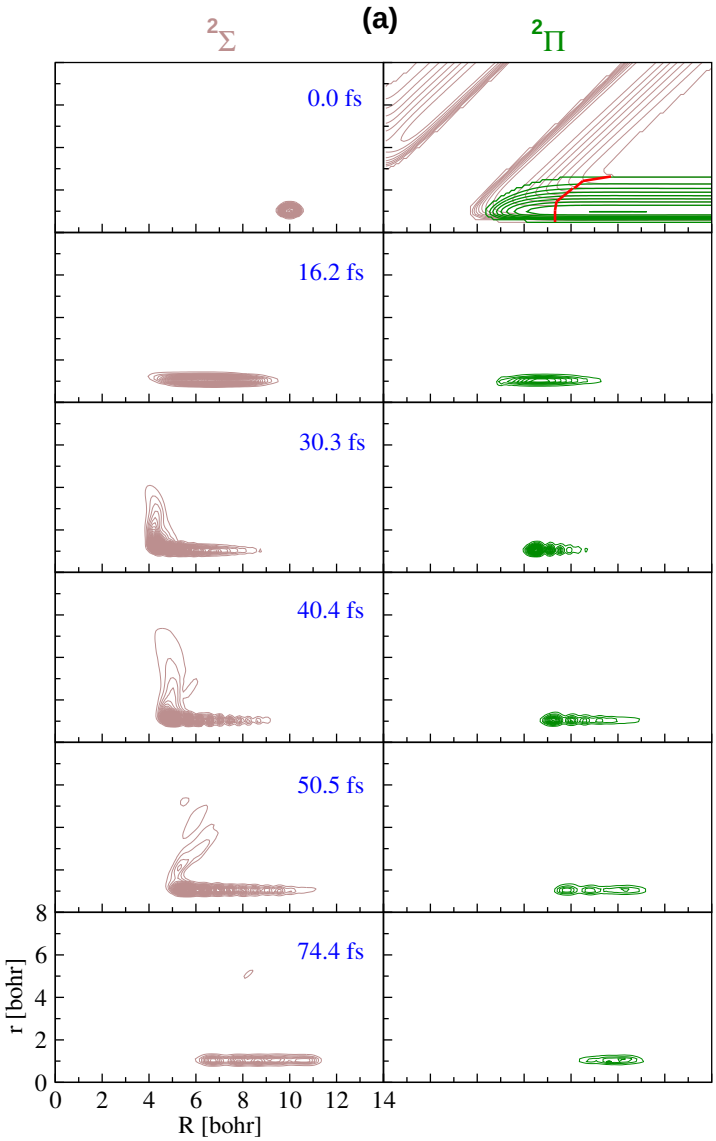

Figure 3.6: Probability density ($|\Psi|^2$) of the WP evolving on the $^2\Sigma$ adiabat in the coupled two-state dynamics of the Cl(^2P) + H_2 (v=0, j=0) → HCl($\Sigma v'$, $\Sigma j'$) + H reaction at different times (indicated in each panel) for the case of the WP initially being on the $^2\Sigma$ adiabat. The potential energy contours of the $^2\Sigma$ and $^2\Pi$ diabatic electronic states for the collinear arrangement of the three nuclei are included as brown and green solid lines, respectively in the upper panel of the right column. The seam of conical intersections of these states is indicated by a solid red line.

Σ-Π electronic coupling) and the reactivity of the $^2\Pi$ state solely arises from the fraction of the WP flux reaching the product channel on the $^2\Sigma$ surface. When compared with the coupled state results of Fig. 3.4, it can be seen that the reactivity of the $^2\Pi$ state is much less than that of the $^2\Sigma$ state. The onset of the reaction occurs at ~ 0.43 eV as in Fig. 3.2. Furthermore, it can be seen from Fig. 3.4 that an adiabatic initial WP yields more product than a diabatic one. This is because the adiabatic initial WP represents an admixture of the two diabatic states. However, this situation does not arise when the reaction is monitored throughout in a diabatic representation.

The time-dependence of the adiabatic and diabatic electronic populations in the coupled state dynamics with the initial WP on the $^2\Pi$ adiabat is shown in Fig. 3.5. The adiabatic and diabatic populations are indicated by the dashed and solid lines, respectively. The upper two curves represent the adiabatic and diabatic electronic populations of the $^2\Pi$ state, whereas, the lower ones represent those of the $^2\Sigma$ state. When compared with the population dynamics of Fig. 3.3, it can be seen that the nonadiabatic effects are much stronger when the reaction is initiated on the $^2\Pi$ state. Since the initial WP is located on the $^2\Pi$ adiabat, the population of this state is 1.0 and that of $^2\Sigma$ adiabat is 0.0 at t=0. The population of the $^2\Pi$ adiabat exhibits an initial sharp decrease to a value of ~ 0.3 within $\sim$ 200 fs followed by quasi-periodic recurrences fluctuating statistically around a value of ~ 0.5 at longer times. The initial sharp decrease of the $^2\Pi$ adiabatic population relates to a nonadiabatic relaxation time of $\sim$ 170 fs of this state. The population of the $^2\Sigma$ adiabat reveals a complementary initial growth followed by quasi-periodic recurrences. The diabatic electronic populations of the $^2\Pi$ and $^2\Sigma$ states are 85% and 15%, respectively, at t=0. The recurrences seen in the adiabatic population curves are heavily damped in the diabatic ones and

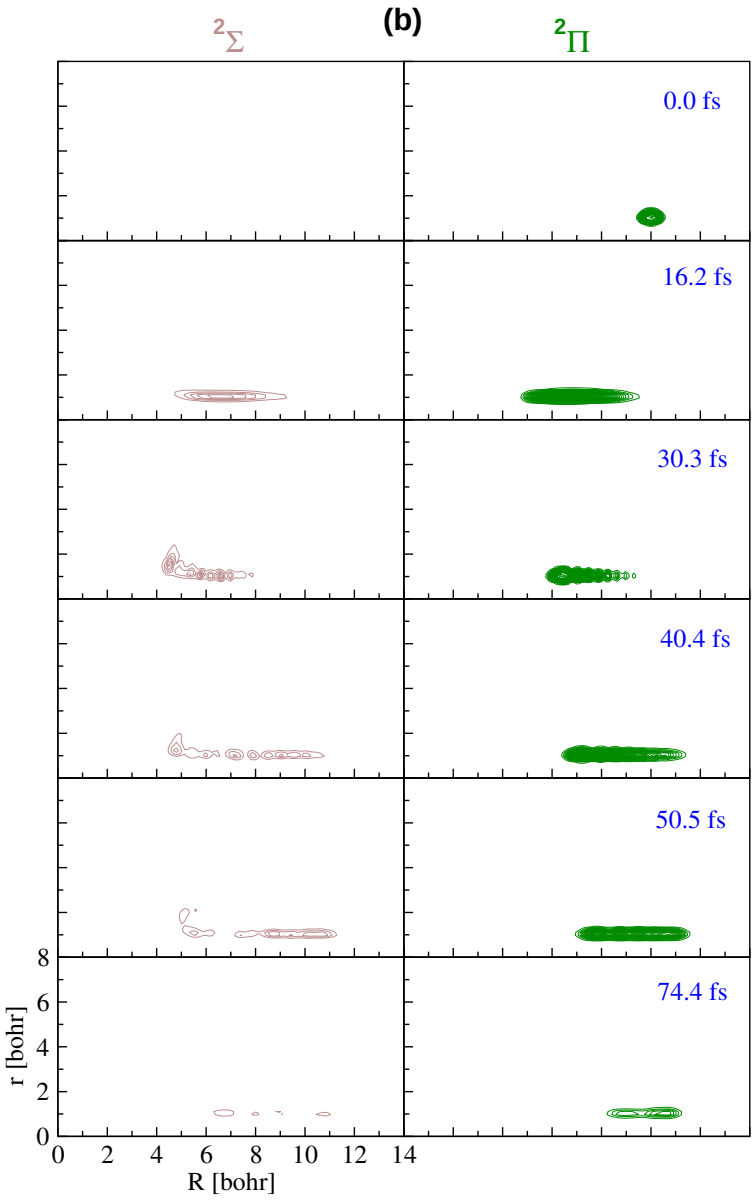

Figure 3.7: Same as Fig. 3.6. The initial WP being located on the $^2\Pi$ adiabat.

indicates a more prominent recrossing of the WP through the conical intersection.

In order to better reveal the vibronic coupling effects on the nuclear dynamics, we show snapshots of the WP probability density ($|\Psi|^2$) evolving on the $^2\Sigma/^2\Pi$ electronic states at different times in Fig. 3.6 and 3.7 when the reaction is initiated on the $^2\Sigma$ and $^2\Pi$ adiabat, respectively. The probability density of the time evolved WP on the $^2\Sigma$ and $^2\Pi$ states are shown in the left and right columns of each figure. The probability density of the WP averaged over the angular coordinate γ. The WP initially located on the $^2\Sigma$ adiabat [cf. Fig. 3.6] approach the interaction region and a part of it transits to the $^2\Pi$ state within $\sim$ 16.2 fs. This is because the seam of $^2\Sigma$-$^2\Pi$ conical intersections lies in the reagent channel [see the upper panel of the right column of Fig. 3.6]. The WP on the $^2\Sigma$ state spreads into the product channel at longer times (cf. 30.3, 40.4 and 77.4 fs) and leads to the formation of the product, HCl ($X^1\Sigma_g^+$) + H (^2S). The WP on the $^2\Pi$ surface on the otherhand, moves back to the reagent channel at longer times and is damped by the absorbing boundary. The motion of the WP on both the $^2\Sigma$ and $^2\Pi$ states at longer times reveals several recrossings through the intersection seam, which is also reflected in the damping of the recurrences in the diabatic population curves in Fig. 3.3. The WP dynamics for the reaction initiated on the $^2\Pi$ adiabat (cf. Fig. 3.7) reveals interesting effects of the conical intersection. Here the reactivity is solely governed by the nonadiabatic coupling effects. It can be seen from the time evolution of the WP that the fraction of the WP flux that transits to the $^2\Sigma$ surface only leads to reaction in the energy range considered here. The seam of conical intersections is more closer to the interaction region of the $^2\Pi$ surface [cf. Fig. 3.6, upper panel of the right column] and the nonadiabatic effects are relatively stronger on the WP dynamics on this state. A significant fraction of the WP flux moves to the $^2\Sigma$ surface within $\sim$ 20

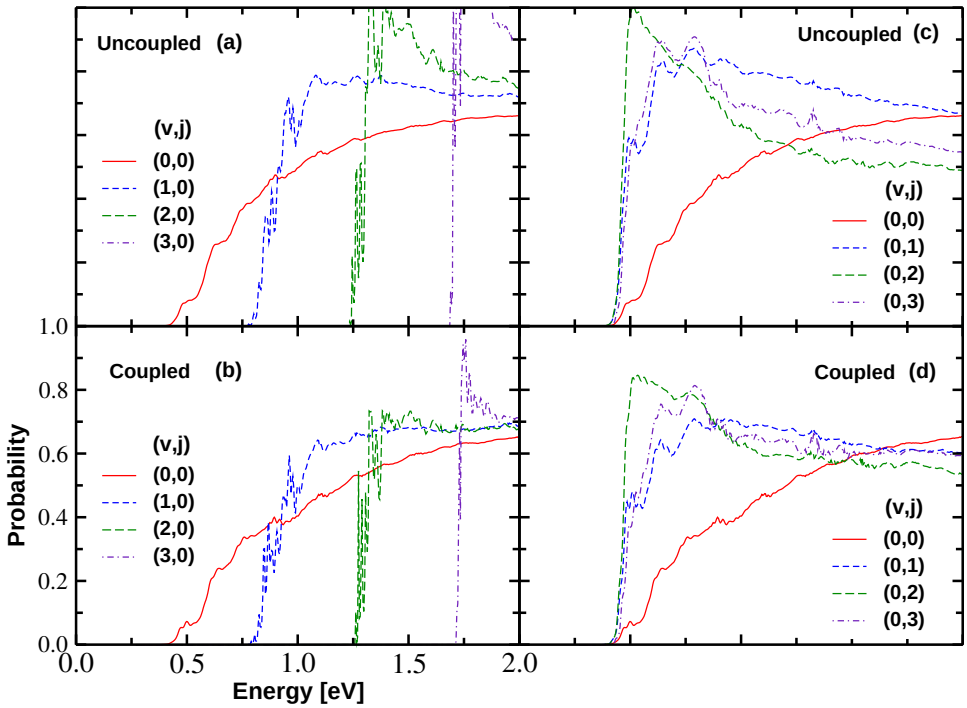

Figure 3.8: Effect of vibrational (in panel (a) and (b)) and rotational (in panel (c) and (d)) excitation of reagent H_2 on the $Cl(^2P)$ + H_2 reaction dynamics on $^2\Sigma$ PES. The uncoupled adiabatic results are shown in the panel (a) and (c). The result obtained in the coupled two-state picture by initiating the reaction on the $^2\Sigma$ adiabat are shown in the panel (b) and (d). The vibrational (v) and rotational (j) quantum states of H_2 are indicated in each panel.

fs, a part of it leads to reaction and the remaining part exhibits several recrossings through the intersection seam, and finally gets absorbed in the reagent channel.

3.3.4 The effect of reagent vibrational and rotational excitation on the reactivity

We now discuss on the effect of vibrational and rotational excitation on the reaction dynamics of the uncoupled and coupled $^2\Sigma$ state. In Fig. 3.8(a) the reaction probabilities of the Cl(^2P) + H_2 (v=0-3, j=0) on the uncoupled $^2\Sigma$ adiabat are shown. When compared with the H_2 (v=0, j=0) reaction probability, it can be seen that the reagent vibration in general promotes the reaction. Understandably, the reaction threshold shifts to the higher total energy on vibrational excitation of the reagent H_2. We note that, the translational energy threshold has been found to shift to a lower value on vibrational excitation. For example, for the probability curves for the uncoupled situation shown in Fig. 3.8(a), this threshold occurs at $E_{tr} \sim$ 0.155, 0.004, -0.039 and -0.051 eV for v=0, 1, 2 and 3, respectively. In the coupled states results of Fig. 3.8(b), the translational threshold further decreases slightly and occurs at $E_{tr} \sim$ 0.142, -0.015, -0.028 and -0.034 eV respectively, in that order. The resonance features become more prominent in the reaction with vibrationally excited reagent. The reaction probabilities of Cl(^2P) + H_2 (v=0-3, j=0) on the coupled $^2\Sigma$ state are shown in Fig. 3.8(b). The reaction is started on the uncoupled $^2\Sigma$ adiabat. When compared with the uncoupled state results of Fig. 3.8(a), it can be seen that the nonadiabatic coupling with the $^2\Pi$ state leads to a decrease of the reaction probability. This is partly because the fraction of the WP flux reaching the $^2\Pi$ state moves into the asymptotic reagent channel of this state and gets absorbed there. The sharp resonance features in the coupled state reaction probabilities of Fig. 3.8(b) remain as prominent as the uncoupled

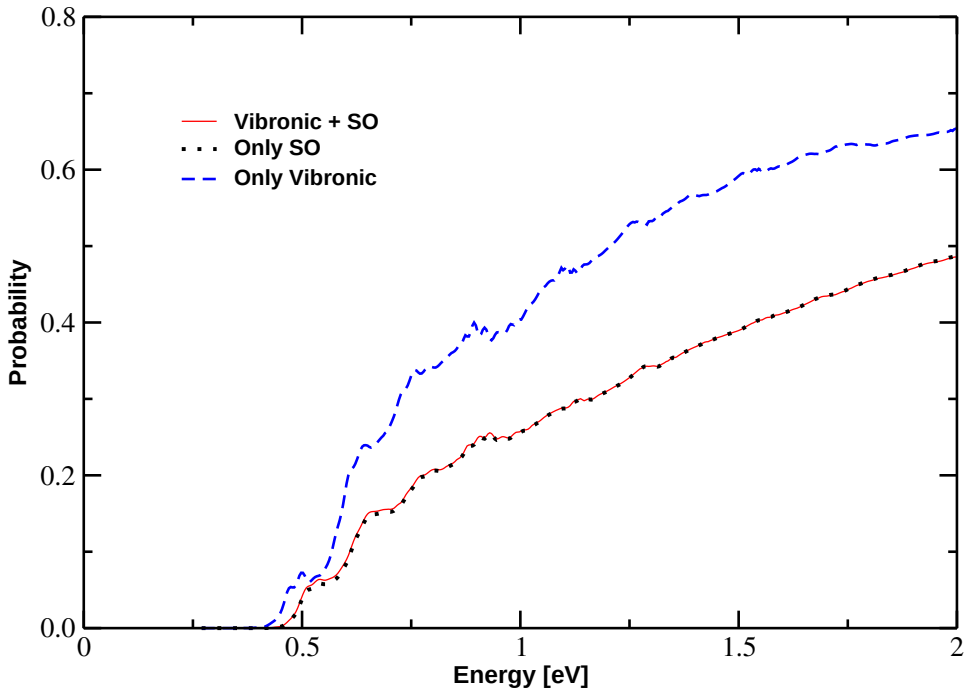

Figure 3.9: Total probability of the Cl(^2P) + H_2 (v=0, j=0) → HCl($\Sigma v'$, $\Sigma j'$) + H reaction calculated with the coupled three-state model of Sec. II.C for $\boldsymbol{J} = 0.5$. The WP is initially located on the $^2\Sigma$ diabat. The reaction probability obtained by considering the vibronic and SO coupling together in the dynamics is shown by the solid line. The dots superimposed on it represent the probability obtained with the SO coupling alone in the dynamics. For comparison the probability obtained with vibronic coupling alone (and shown in Fig. 3.2) for $\boldsymbol{J} = 0$ is included as dashed lines.

state results of Fig. 3.8(a).

The effect of reagent rotation on the reaction on the uncoupled and coupled $^2\Sigma$ state is shown in Figs. 3.8(c) and 3.8(d), respectively. The translational energy threshold also decreases with increasing rotational excitation. This threshold occurs at $E_{tr} \sim 0.155$, 0.113, 0.082 and 0.045 eV in the uncoupled state results (cf. Fig. 3.8(c)) and at $E_{tr} \sim 0.142$, 0.097, 0.072 and 0.041 eV in the coupled state results (cf. Fig. 3.8(d)) for $j = 0$, 1, 2 and 3, respectively. It can be seen from Fig. 3.8(c) that, the rotational excitation of the reagent H_2 facilitates the reaction at low energies. The resonance features are not as sharp as that obtained with the vibrationally excited reagent (cf. Fig. 3.8(a)). Inclusion of the coupling to the $^2\Pi$ state decreases the overall reaction probabilities (cf. Fig. 3.8(b)) when compared with the uncoupled state results of Fig. 3.8(c). The overall variation of the coupled state reaction probabilities (cf. Fig. 3.8(d)) with energy and the resonance features are similar to that of the uncoupled state results of Fig. 3.8(c).

3.3.5 Nonadiabatic effects due to Electronic and Spin-Orbit Coupling

We now examine the combined vibronic and SO coupling effects on the Cl(^2P) + H_2 (v=0, j=0) $\rightarrow$ HCl($\Sigma v'$, $\Sigma j'$) + H reaction employing the coupled three-state model described in Section 2.3.2. In Fig. 3.9, we show the energy dependence of the total reaction probability for the case of the WP initially on the $^2\Sigma_{1/2}$ diabat. The results obtained by considering the vibronic and SO coupling together for $\boldsymbol{J} = 0.5$ are plotted with the solid red line. The black dots superimposed on it indicate the results obtained by considering the SO coupling alone in the dynamics. For comparison, we also include the results obtained with the vibronic coupling alone (cf. Fig. 3.2) as blue dashed lines in Fig. 3.9. It can be seen that the SO

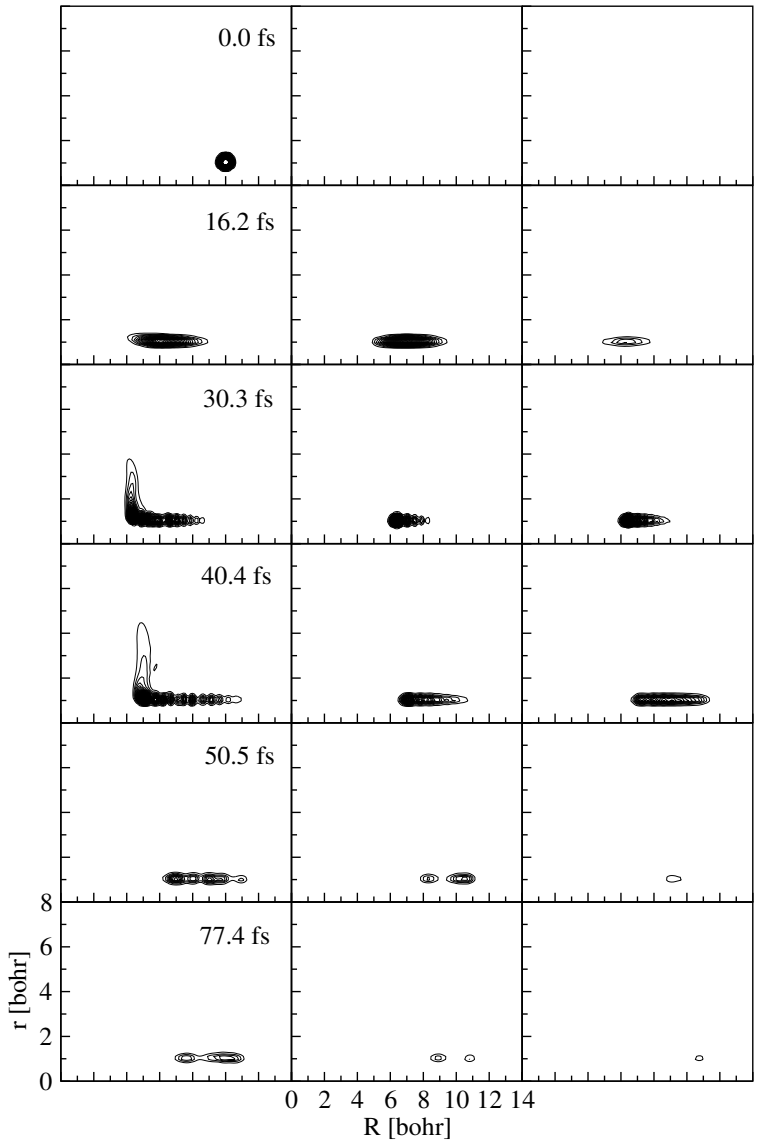

Figure 3.10: Probability density ($|\Psi|^2$) of the WP on the $^2\Sigma_{1/2}$ (left panel), $^2\Pi_{3/2}$ (middle panel) and $^2\Pi_{1/2}$ (right panel) diabats at different times (indicated in each panel) in the coupled three-state dynamics of Cl(^2P) + H_2 (v=0, j=0) $\rightarrow$ HCl($\Sigma v'$, $\Sigma j'$) + H reaction. The WP is initially located on the $^2\Sigma_{1/2}$ diabat and both the vibronic and SO coupling effects are considered.

coupling have significant impact on the reaction dynamics with H_2 (v=0, j=0) as compared to the electronic coupling. It is shown above that the uncoupled and coupled (vibronic) results for the $^2\Sigma$ diabat do not differ. It can be seen from Fig. 3.9 that the results obtained with the vibronic and SO coupling together and the SO coupling alone are nearly identical. The reactivity of the $^2\Sigma$ state significantly decreases when SO coupling is considered. A close look at the oscillations in the reaction probability curves in Fig. 3.9 reveals that some of the fine oscillations observed with the vibronic coupling alone are absent in the probability curve with the SO coupling. These fine oscillations (although are not very prominent) may arise from the Stueckelberg type of interference effects between the $^2\Sigma$ and $^2\Pi$ like amplitudes for reactive scattering. The existence of such oscillations is demonstrated for the first time in the Cl(^2P) + HCl reaction [73]. The present system has some commonality with it, however, the SO coupling effects in the present case appears to be stronger. The remaining oscillations are due to the resonances in the system.

The time evolution of the WP in the coupled three-state picture is shown in Fig. 3.10. The WP densities on the $^2\Sigma_{1/2}$, $^2\Pi_{3/2}$ and $^2\Pi_{1/2}$ diabatic states at different times (indicated in the panel) are shown in the left, middle and right column of Fig. 3.10, respectively. Since the reaction is started on the $^2\Sigma_{1/2}$ diabat, the WP density on the other two states is 0.0 at t=0. It is already noted above that the vibronic coupling does not affect the reaction probability in this case. The nonadiabatic transition in this case is mainly caused by the SO interactions. The latter drive considerable fraction of WP flux to the $^2\Pi_{3/2}$ and $^2\Pi_{1/2}$ diabats already within $\sim$ 16 fs. The amount of the WP flux flowing to the latter state is significantly lower than to the former one. It can be seen that the WP flux on the $^2\Sigma_{1/2}$ diabat only leads to the reaction. The WP flux on the other

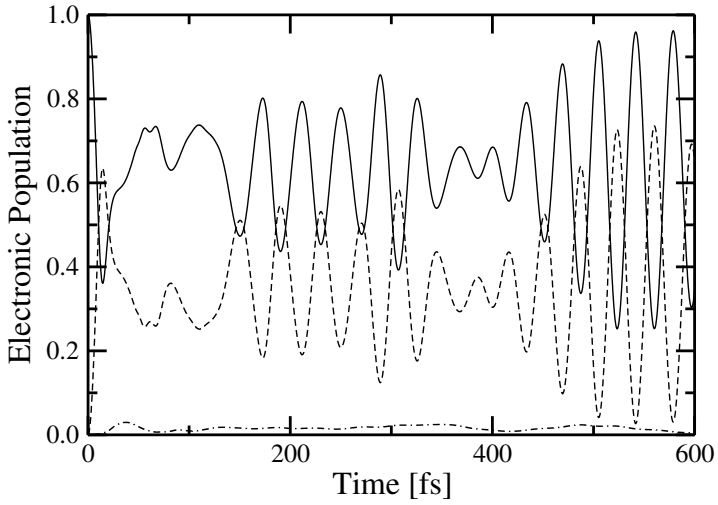

Figure 3.11: Time dependence of the electronic populations of the $^2\Sigma_{1/2}$ (solid line), $^2\Pi_{3/2}$ (dashed line) and $^2\Pi_{1/2}$ (dot-dashed line) diabats in the coupled three-state dynamics of Fig. 8. The WP is initially located on $^2\Sigma_{1/2}$ diabat.

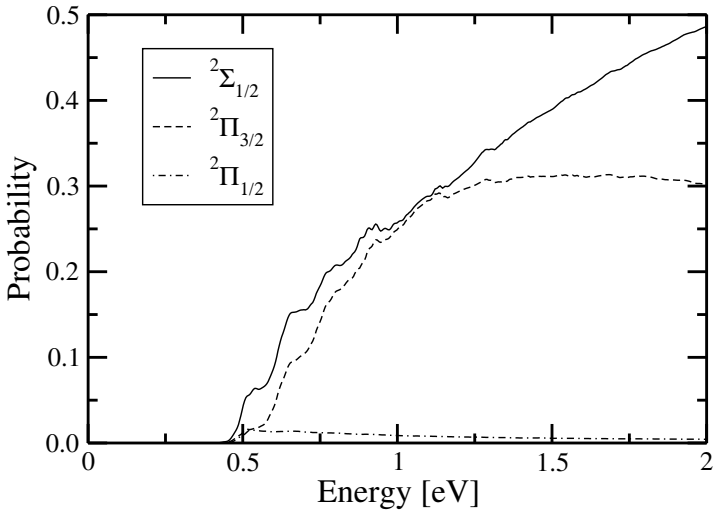

Figure 3.12: Total probability of the Cl(^2P) + H_2 (v=0, j=0) → HCl($\Sigma v'$, $\Sigma j'$) + H reaction obtained by initially preparing the WP in the $^2\Sigma_{1/2}$ (solid line), $^2\Pi_{3/2}$ (dashed line) and $^2\Pi_{1/2}$ (dot-dashed line) diabat. The probabilities are calculated with coupled three-state model of Sec. II.C and for $\boldsymbol{J} = 0.5$.

two states finally gets absorbed by the absorbing potential in their asymptotic reagent channel. These observations are also supported by the time dependence of the diabatic electronic populations plotted in Fig. 3.11. The populations of the $^2\Sigma_{1/2}$, $^2\Pi_{3/2}$ and $^2\Pi_{1/2}$ diabat are shown by the solid, dashed and dot-dashed lines, respectively. It can be seen that there is significant exchange of WP flux between the $^2\Sigma_{1/2}$ and $^2\Pi_{3/2}$ states, the flux flow to the $^2\Pi_{1/2}$ state on the other hand is significantly less which is also indicated by the WP densities in Fig. 3.10. The initial sharp decrease of the WP flux of the $^2\Sigma_{1/2}$ state and its flow to the $^2\Pi_{3/2}$ state reveals a considerable strength of SO coupling between these states.

3.3.5.1 Reactivity of different Spin-Orbit States

The reactivity of the different SO states of Cl(^2P) + H_2 (v=0, j=0) is presented in Fig. 3.12. Here the probability results are obtained by initiating the reaction on the $^2\Sigma_{1/2}$, $^2\Pi_{3/2}$ and $^2\Pi_{1/2}$ diabat separately in the coupled three-state picture for $\boldsymbol{J} = 0.5$. The resulting probability results are shown by the solid, dashed and dot-dashed lines, respectively, in that order. The Π state reacts *via* nonadiabatic transitions to the $^2\Sigma_{1/2}$ state. This is solely mediated by the Σ-Π SO coupling. It can be seen from Fig. 3.12 that the SO excited state of Cl atom is less reactive compared to its SO ground state. This is in agreement with the available theoretical results [80, 81] but in apparent contradiction with the experiment [62, 63].

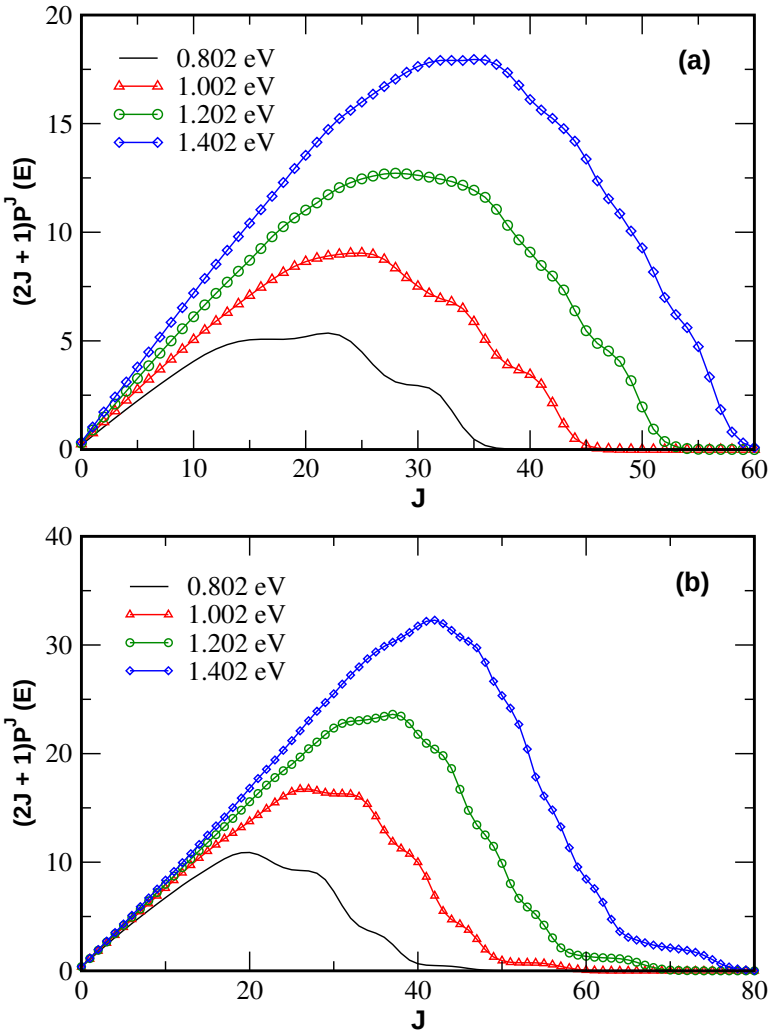

Figure 3.13: Weighted partial wave contribution to the total integral reaction cross sections in the coupled-state situation for $Cl(^2P)$ + H_2 (panel a) and $Cl(^2P)$ + HD reaction (panel b) at various values of the total energy (indicated in each panel) for the lowest value of v and j.

3.3.6 Reactive Scattering for $J \neq 0$

In this section, we present and discuss the preliminary results on the reaction probability ($J \neq 0$), reaction cross section and thermal rate constant obtained for $Cl(^2P) + H_2$ and $Cl(^2P) + HD$ reactions within the CS approximation employing the theoretical methodology discussed in Sec. 2.6.1. All the WP calculations are carried out by treating Ω as a fixed parameter and appropriate eigenvector matrix is used corresponding to a given Ω value to setup the DVR-FBR transformation matrix. The reaction probabilities are calculated upto a total energy of 1.4 eV and inclusion of partial-wave contribution upto $J = 58$ is found to be necessary to obtain a converged reaction cross section for the $Cl(^2P) + H_2$ reaction in this energy range. This has been verified in Fig. 3.13(a) by plotting the J dependence of the degeneracy weighed coupled reaction probability with four representative values of the total energy. The weighed probability values for a given energy initially increases with J due to the degeneracy factor $(2J + 1)$ and then decreases at higher J values, due to the shift of the reaction threshold caused by the centrifugal barrier. Similar exercise has been undertaken for the isotopic $Cl(^2P) + HD$ reaction. Partial wave contribution upto $J = 69$ is found to be necessary in this case [c.f. 3.13(b)].

The total reaction probabilities for few selected values of total angular momentum $J = 10$, 20, 40 and 50 and $\Omega = 0$, of the $Cl(^2P) + H_2$ reaction on the uncoupled $^2\Sigma$ surface are plotted in Fig. 3.14 as a function of the total energy E. The $J = 0$ reaction probability reproduced form Fig. 3.1 is also shown for comparison. It can be seen that the reaction onset shifts to higher energies with the increase of the total angular momentum, J. The sharp resonance structures in the reaction probability for $J = 0$ are found to be less pronounced as the J value increases revealing a more direct nature of the reaction. But on the average the

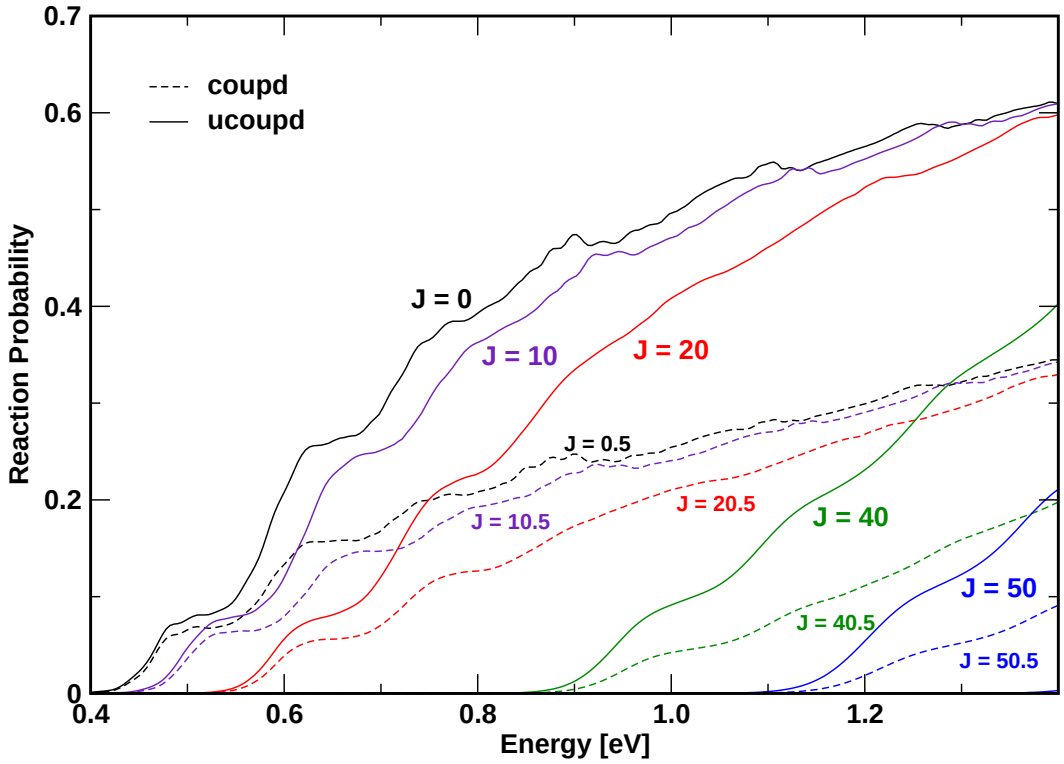

Figure 3.14: Same as Fig. 3.1 and 3.10, for the total angular momentum, $J = 0$, 20, 40 and 50 (indicated in the panel). The uncoupled and coupled state results are shown by solid and dashed lines, respectively.

reaction probabilities for higher values of J are smaller than the corresponding J = 0 results, indicating substantial nonreactive scattering for $J \neq 0$ collisions.

In order to see the effect of electronic and SO coupling on the $J \neq 0$ reaction probabilities, we show the energy dependence of the total reaction probability of the Cl(^2P) + H_2 reaction for J = 10.5, 20.5, 40.5 and 50.5 and Ω = 0.5 in the coupled state situation initially locating the WP on the $^2\Sigma_{1/2}$ diabat, as dashed lines in Fig. 3.14. The results obtained by considering both electronic and SO coupling in the dynamics. We also include the result obtained with J = 0.5 for comparison. The reaction probability significantly decreases with the inclusion of the electronic and SO coupling as we have already discussed in Sec. 3.3.5 for $J = 0.5$. The reaction probability continues to decreases with increasing J and the difference between the uncoupled and coupled surface results also gradually decreases as J increases. Here we note that, the results obtained with the electronic coupling alone do not differ much form the uncoupled state results [see Fig. 3.10], hence we do not consider them here. It can be seen in Fig. 3.14 that, the reaction onset in the coupled state situation shifts towards higher energy compared to the uncoupled one and this shift increases with the increase of the total angular momentum, J. This is because of the higher centrifugal potential due to the SO coupling that adds up with the effective potential energy in coupled state situation [see Eq. 2.17]. The resonance structures also gradually disappear with increasing J in the coupled state situation.

Now we discuss the reaction probabilities calculated for the isotopic Cl(^2P) + HD reaction. This reaction yields either DCl + H (channel R1) or HCl + D (channel R2) products, therefore, in the following, we report the channel specific reaction probabilities. The reaction probabilities of channel R1 and R2 for Cl(^2P) + HD (v = 0, j = 0) reaction as a function of the total energy are plotted in

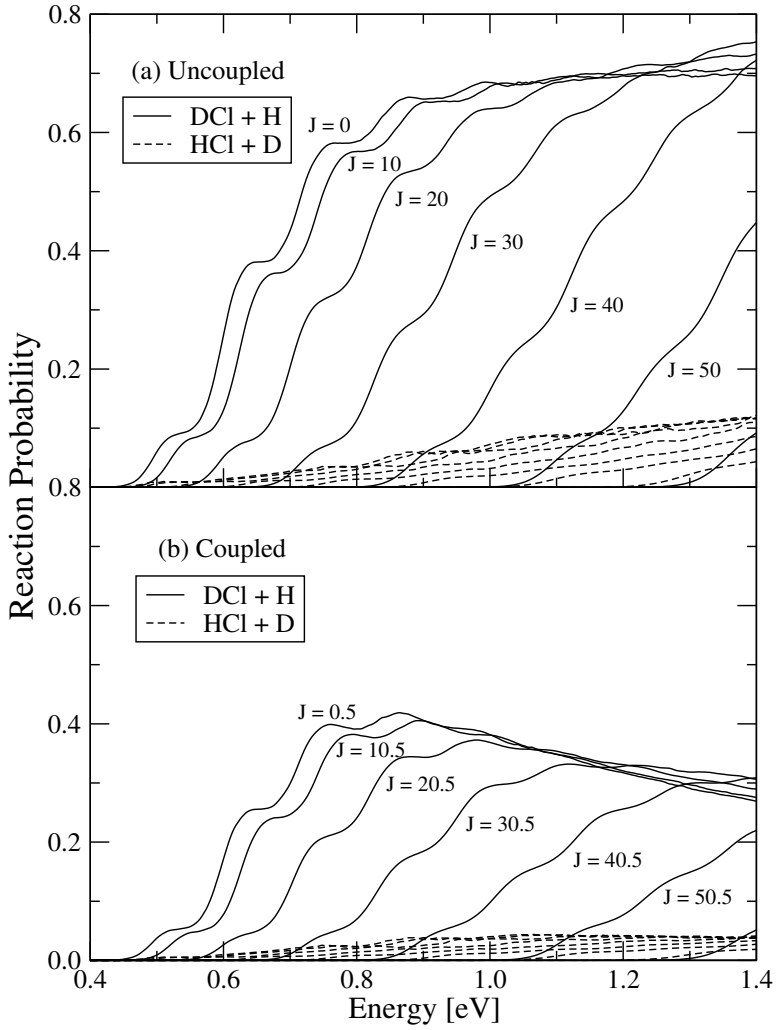

Figure 3.15: Same as Fig. 3.13 for the Cl(^2P) + HD reactions for a few selected total angular momentum J (indicated in each panel) in the uncoupled- (panel a) and coupled-state (panel b) situations.

Fig. 3.15(a-b). We show in Fig. 3.15(a), the reaction probabilities for few representative values of $J = 0$, 10, 20, 30, 40, 50 and 60 (indicated in the panel) and for $\Omega = 0$, by treating the nuclear dynamics on the lower adiabatic surface of the Cl(^2P) + HD reaction without including any nonadiabatic coupling in the dynamics. For the lowest vibrational and rotational state of the reagent HD ($v = 0$ and $j = 0$), the reaction probability results for channel R1 (DCl + H) and channel R2 (HCl +D) are shown by solid and dashed lines, respectively. It can be seen that, the reaction probabilities of R2 channel is very low compared to R1 and formation of DCl + H (R1) is always favored over the the formation of HCl + D (R2) for all values of J. The probability values in both the channels reveal the signature of resonances. However, the resonances are found to be less pronounced for the R2 channel (HCl + D) and gradually vanishes for higher values of J.

In Fig. 3.15(b) we plot the reaction probabilities of Cl(^2P) + HD reaction for $J = 0.5$, 10.5, 20.5, 30.5, 40.5, 50.5 and 60.5, $\Omega = 0.5$ including both electronic and SO coupling in the dynamics. The reaction is studied in the coupled state situations in this case, initially preparing the WP on the asymptotic reagent channel of the ground $^2\Sigma_{1/2}$ diabatic PES of the Cl(^2P) + HD reaction. As we have seen for Cl(^2P) + H_2 reaction, the reactivity of both the channels significantly decreases when the coupling is activated. Some of the fine oscillations in the coupled state reaction probability also become absent when compared with the uncoupled state results. Similar to Cl(^2P) + H_2 reaction, the electronic coupling has a negligible impact on the dynamics of the Cl(^2P) + HD reaction and the SO coupling is mainly responsible for the reduced reaction probability in the coupled state situation. Here, we like to note that, all the coupled state results presented here includes both electronic and SO coupling and the dynamics is treated throughout in a diabatic electronic representations.

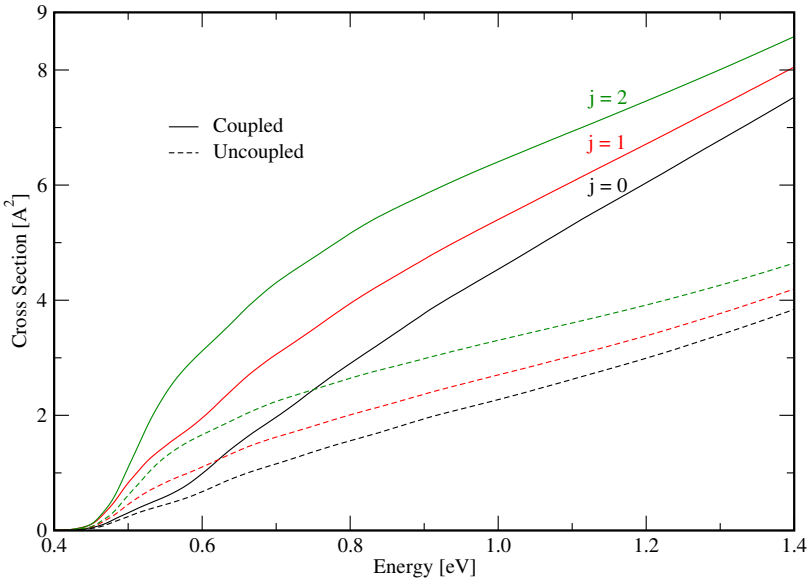

Figure 3.16: Initial state-selected integral reaction cross sections of the Cl(^2P) + H_2 ($v = 0$, $j = 0$, 1, 2) as a function of the total energy E. The cross sections in the uncoupled and coupled state situation are represented by solid and dashed lines, respectively.

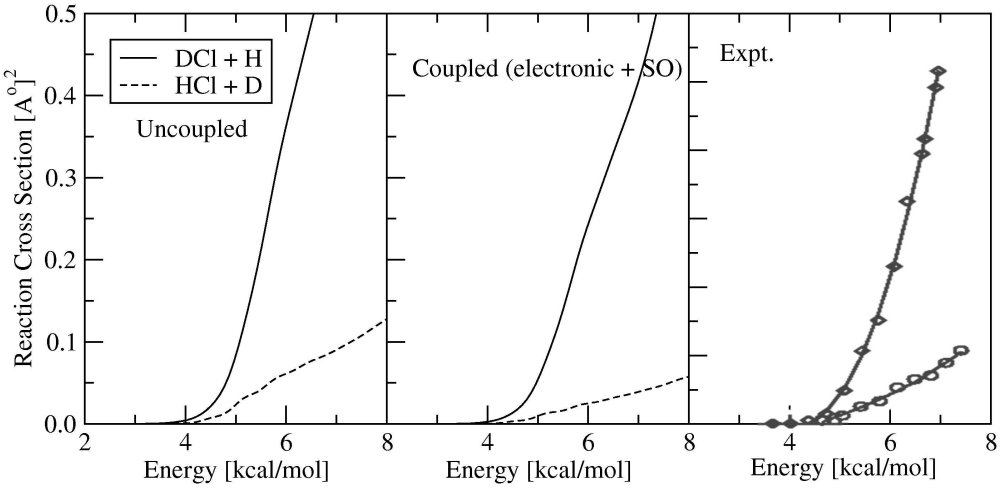

Figure 3.17: Same as Fig. 3.16 for the Cl^2P + HD ($v = 0$, $j = 0$) collision for channel R1 (solid line) and channel R2 (dashed line) in the uncoupled and coupled state situation of Cl(^2P) + HD reaction are plotted along with the experimental recording of Liu et. al. [60].

3.3.7 Initial state-selected integral Reaction Cross Sections

The initial state-selected and energy resolved integral reaction cross sections, as a function of the total energy in the Cl(^2P) + H_2 collisions are shown in Fig. 3.16. These cross sections are calculated by summing up different partial wave contributions with appropriate weights to the reaction probability using Eq. 2.58. The results considering electronic and SO coupling and without considering any coupling in the dynamics are shown by dashed and solid lines, respectively. The reaction cross sections for both the uncoupled and coupled state situations obtained with rotationally excited reagent H_2 ($j = 0$ - 2, indicated in different colors) in its vibrational ground level (v =0) are also shown. The cross section results for $j > 0$ includes contributions form $\Omega > 0$, with maximum $\Omega_{max} = \min(j, J)$, within the CS approximation. The reaction cross section value increases with increasing j and for a given value of j the reaction cross section increases gradually with the total energy in both the uncoupled and coupled state situations. The difference between the uncoupled and coupled state results for a given value of j, is small at low collision energies and increases gradually as the total energy increases. This difference becomes more significant with increasing value of j.

The initial state-selected and energy resolved integral reaction cross sections, as a function of collision energy (total energy - the rovibrational energy of the diatom) of the Cl(^2P) + HD reaction are shown in Fig. 3.17 with the reagent HD in its lowest vibrational and rotational level. The uncoupled and coupled state results are shown in the first two panels, respectively, along with the experimental results of Liu et. al. [60] in the last panel. The overall shape of the theoretical reaction cross sections matches well with the experimental results. But there is a very little difference between the calculated uncoupled and coupled state reaction

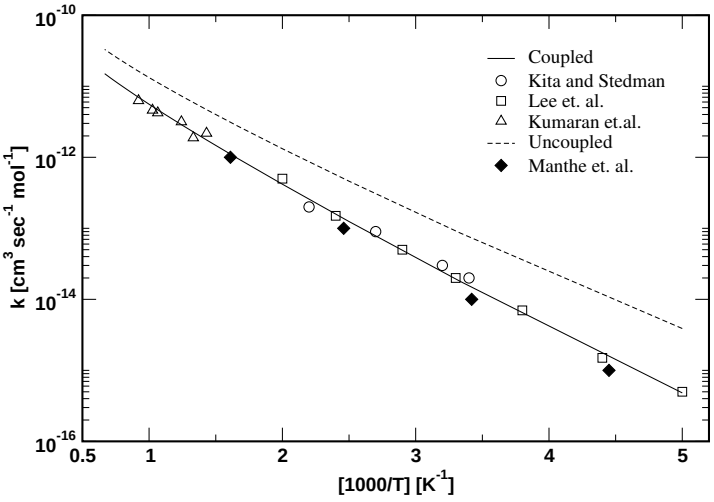

Figure 3.18: Arrhenius plot of the Boltzmann averaged (over j = 0 - 2) thermal rate constants for Cl(^2P) + H_2 ($v = 0$) reaction. The coupled and uncoupled state results are shown by solid and dashed lines, respectively. Points on the diagram represents the results from the literature (see text).

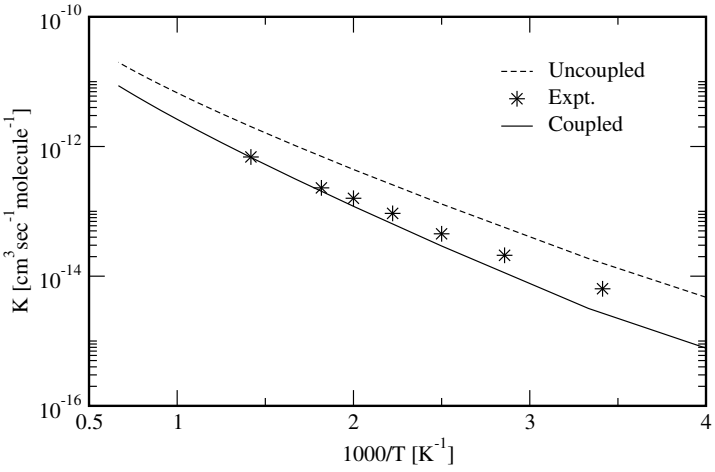

Figure 3.19: Same as Fig. 3.18 for Cl(^2P) + HD reaction.

cross sections. This is because, the entire experimental collision energy range is very low (3 - 7 kcal/mol) and the onset of the reaction probabilities are almost same for both the uncoupled and coupled state situations.

3.3.8 Thermal Rate Constants: Comparison with the experiment

The thermal rate constants obtained by statistically averaging over the rotational states $j = 0$ - 2 are shown in Fig. 3.18 for the $Cl(^2P) + H_2$ $(v = 0)$ reaction. The result obtained by considering electronic and SO coupling in the dynamics is shown by the solid line and the same without considering any coupling are represented by the dashed line. The available experimental [142–145] and recent theoretical results [96] are shown as different points on the diagram. The experimental results of Kita and Stedman [142], Lee *et al.* [143] and Kumaran *et al.* [144] are represented by unfilled circle, square and triangle, respectively. Recent quantum calculations result on the $Cl(^2P) + H_2$ thermal rate constant by Manthe *et al.* [96] is also presented as filled diamonds in Fig. 3.18. It can be seen that the thermal rate constants calculated without including any coupling in the dynamics is far from the experimental results whereas the results considering the electronic and SO coupling in the dynamics matches well with the experiment. Manthe *et al.* [96] calculated the thermal rate constants by using MCTDH method on the single $^2\Sigma_{1/2}$ adiabatic CW PES by explicitly including the SO coupling in the dynamics. Thus, it can be inferred that, the inclusion of SO coupling in the dynamics is necessary to understand the experimental thermal rate constant of $Cl(^2P) + H_2$ reaction.

The experimental rate constants for the $Cl(^2P) + HD$ reaction recorded by Taatjes et. al. [57] are shown as different points and compared with our theoretical

results in Fig. 3.19. Similar to the Cl(^2P) + H_2 reaction, the theoretical results including the electronic and SO coupling is closer to the experimental one. The rate constants match well in the high temperature region, but the difference becomes significant as one moves towards the lower temperature.

3.4 Summary

We have presented a theoretical account of the reactive scattering occurring on three electronic states with two different coupling mechanisms. We then apply this to investigate the dynamics of Cl(^2P) + H_2 $\rightarrow$ HCl ($X^1\Sigma_g^+$) + H (^2S) reaction. The vibronic and SO coupling of the PESs are considered and the nuclear dynamics is studied with the aid of a time-dependent WP approach. We first focus on the role of the vibronic coupling of the $^2\Sigma$-$^2\Pi$ surfaces in the reaction dynamics. These two surfaces form a conical intersection for the collinear arrangement of the three nuclei. With the aid of a coupled two-state model we studied the effects of this conical intersection on the initial state-selected reaction probabilities of this system. Our findings revel a decrease in the probability (when compared with the uncoupled state probability results) when reaction is started on the $^2\Sigma$ adiabat in the coupled state picture. Initiation of the reaction on the $^2\Sigma$ diabat on the other hand has 'no impact 'of vibronic coupling - it leads to the same reaction probability as obtained on the uncoupled $^2\Sigma$ diabat. The reagent vibration in general promotes the reaction and resonances become more prominent when reagent H_2 is vibrationally excited. The reagent rotation also promotes the reaction at low energies. The $^2\Pi$ surface is non-reactive (adiabatically) in the energy range considered in the present paper. However, in the coupled state picture it reacts *via* the conical intersection and leads to the re-

action. Here also initiating the reaction on the $^2\Pi$ adiabat /$^2\Pi$ diabat leads to significant differences in the probability results.

The impact of the vibronic and SO coupling effects in the reaction dynamics is examined next. To the best of our knowledge this situation is rigorously treated for the first time in a time-dependent picture using coupled three-states consisting of six diabatic surfaces. Our analysis reveled a huge impact of SO coupling on the Cl(^2P) + H_2 (v=0, j=0) reaction dynamics. The reactivity of the $^2\Sigma_{1/2}$ decreases significantly (from that of uncoupled surface results) when the SO coupling is considered. The reactivity of the SO excited Cl ($^2P_{1/2}$) is found to be less than the SO ground Cl ($^2P_{3/2}$), in accord with the available theoretical results [80,81].

We presented a preliminary theoretical results on the channel specific reaction cross sections and thermal rate constants for the Cl(^2P) + H_2 and Cl(^2P) + HD reactions. The quantum dynamical simulations are carried out by a time-dependent WP approach within the CS approximations. Calculations of initial state-selected energy resolved reaction probabilities, integral reaction cross sections and thermal rate constants are carried out both in the uncoupled and coupled surface situations in order to examine the effect of the surface coupling on the reaction dynamics. The theoretical results of the integral reaction cross sections and the thermal rate constants are in good accord with the available experimental findings.

Chapter 4

Photodetachment Spectroscopy of ClH_2^- (ClD_2^-)

4.1 Introduction

In this chapter, the photodetachment spectrum of ClH_2^- is theoretically studied. Detachment of one electron probes the van der Waals well region of the reagent asymptote of the reactive Cl + H_2 PESs. The reaction Cl(^2P) + H_2 is slightly endothermic (endothermicity $\sim$ 0.045 eV) and proceeds on a late barrier type of surface (barrier hight $\sim$ 0.366 eV) [81]. Unlike the exothermic F(^2P) + H_2 reaction which proceeds on an early barrier surface and the geometry of FH_2^- is close to this barrier (so that the photodetachment spectroscopy could probe the transition state region of the F + H_2 PES [146]), the geometry of ClH_2^- is much stretched [147] and is far away from the configuration at the barrier. The geometry of ClH_2^- is close to the van der Waals well region of the Cl(^2P) + H_2 asymptote and therefore the photodetachment spectroscopy could successfully probe this delicate region of the PES [64, 65].

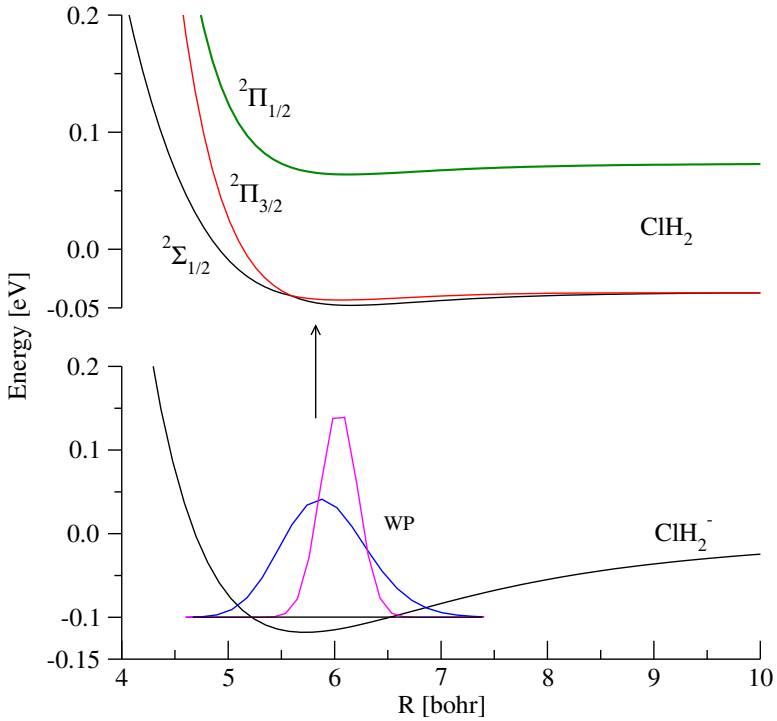

Figure 4.1: Schematic representation of the adiabatic potential energy surfaces of the ground electronic state of ClH_2^- (solid line in the lower part) and the $^2\Sigma_{1/2}$, $^2\Pi_{3/2}$ and $^2\Pi_{1/2}$ SO states of $Cl(^2P)$ + H_2 (in the upper part) along R for r = 1.402 a_0 and $\gamma = 0°$. The initial *ab initio* WP calculated by relaxation scheme and the initial GWP are included in the lower part of the diagram and shown as dashed and dotted lines, respectively. The zero-point vibrational level of ClH_2^- is also shown as a solid line in the lower potential curve. The arrow in the diagram indicates the FC transition.

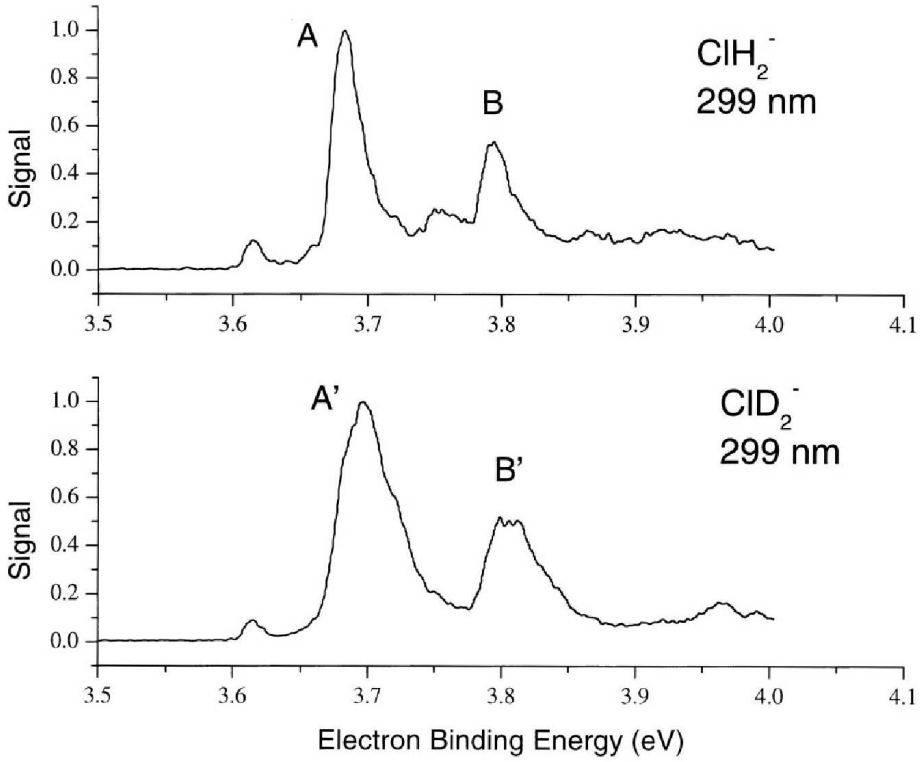

Figure 4.2: Experimental photoelectron spectra of ClH_2^- (top) and ClD_2^- (bottom) at 299 nm (4.154 eV) reproduced form Ref. [64]

The photodetachment process of ClH_2^- is schematically described in Fig. 4.1. The adiabatic potential energy surfaces of the ground electronic state of ClH_2^- and the SO states of ClH_2 are plotted as a function of R for $r = 1.402\ a_0$ and $\gamma = 0°$. The ClH_2^- potential energies are obtained from the PES reported by Alexander [148] and plotted as a solid line in the lower part of the diagram. The ClH_2^- ion is reported to have a linear equilibrium geometry with $R = 5.714$ a_0 [148]. Using the PES of Alexander the wavefunction for the ground vibrational level of ClH_2^- is calculated by a Lanczos based relaxation scheme [149] where the time propagation of the wavefunction is carried out by the short iterative Lanczos procedure with variable time steps. This yields a zero-point energy of $\sim$ -0.097 eV for the anionic ground state. The ground vibrational wavefunction of the anion obtained by this method is superimposed on the anionic potential curve in Fig. 4.1 and shown by the pink line. The zero-point energy level of the anion is indicated by the horizontal line in the diagram. The initial GWP used in this study is also shown as a blue line in the diagram. The FC transition of the anion to the coupled $\Sigma - \Pi$ electronic states of the neutral is indicated by the vertical arrow. In the upper part of the diagram the $^2\Sigma_{1/2}$, $^2\Pi_{3/2}$ and $^2\Pi_{1/2}$ adiabatic SO states of ClH_2 [for $r = 1.402\ a_0$ and $\gamma = 0°$] are shown. The minimum of the van der Waals well occurs at the C_{2v} geometry of ClH_2 at $R_e \sim 5.78\ a_0$. It can be seen from the figure that this value lies well within the range of the anion radical wavefunction. Despite a large difference between the equilibrium geometry of ClH_2^- and the location of the van der Waals minimum on the ClH_2 PES along the angle γ, the ground anionic wavefunction is delocalized along the angle and its amplitude covers a substantial range of γ.

This is the first example of a reactive system where the reagent van der Waals well could be probed through the photodetachment spectroscopy and thereby

providing new spectroscopic evidence of the existence of van der Waals well on a reactive PES. Our theoretical investigations reported herein are motivated by the experimental findings of Neumark and coworkers [64,65]. Their experimental photodetachment spectrum of ClH_2^- shown in Fig. 4.2, is measured at 299 nm (4.154 eV). It revealed two dominant peaks (A and B) at 3.683 eV and 3.793 eV with of 26 and 23 meV widths, respectively. In case of ClD_2^-, the two peak maxima (A' and B') were estimated at 3.697 eV and 3.806 eV. Even though the seperation between the peaks are almost same for these two isotopomers, the photodetachment spectrum of ClD_2^- spectrum are much broader than that of the ClH_2^- spectrum. These two major peaks are attributed to be arising from transitions to the van der Waals wells of the ground and SO excited electronic states of the neutral $Cl(^2P)$ + H_2 system. The separation between the peak maxima of $\sim$ 0.111 eV for ClH_2^- and $\sim$ 0.109 eV for ClD_2^- compares well with the Cl SO splitting of $\sim$ 0.109 eV. Our theoretical approach is based on a time-dependent WP formalism of the Franck-Condon (FC) transition of the ClH_2^- anion to the three coupled electronic states of neutral ClH_2 [150, 151]. The diabatic potential energy surfaces for the $^2\Sigma_{1/2}$, $^2\Pi_{3/2}$ and $^2\Pi_{1/2}$ states of the neutral ClH_2 and their vibronic and SO coupling surfaces reported by Werner and coworkers [75] are employed in our dynamical study. We also use the *ab initio* PES of the ClH_2^- ground electronic state reported by Alexander [148].

4.2 Methodology and Computational Details

In this section we briefly discuss on the theoretical approach employed to describe the photodetachment process. The nuclear dynamics on the coupled diabatic electronic states is followed by a time-dependent WP approach. Since the details

of such an approach are documented in Chapter 2, we will concentrate only on the essentials here. In the time-dependent formalism, the golden rule expression for the spectral intensity pertinent to the Franck-Condon transition of the anion from its vibrational and electronic ground state to the final electronic manifold of the neutral is given by [35]

$$I(E) \sim Re \int_0^\infty e^{iEt/\hbar} \langle \Psi(0) | e^{-i\mathcal{H}t/\hbar} | \Psi(0) \rangle dt, \tag{4.1}$$

where,

$$|\Psi(0)\rangle = |\Psi(t=0)\rangle = \begin{pmatrix} \tau_1 \\ \tau_2 \\ \tau_3 \end{pmatrix} |\Psi^{anion}\rangle, \tag{4.2}$$

plays the role of initial anionic wavefunction prepared on the final coupled manifold of three electronic states of the neutral by photodetachment. The quantities τ_1, τ_2 and τ_3 are the matrix elements of the transition operators for these three electronic states. $|\Psi^{anion}\rangle$ corresponds to the nuclear wave function of the electronic and vibrational ground state of ClH_2^-. $\mathcal{H}$ is the 3×3 diabatic Hamiltonian matrix of the final electronic manifold of neutral ClH_2, which is written below in a diabatic signed-λ basis as introduced by Alexander and Manolopolous [47]. In contrast to the adiabatic electronic basis, the matrix elements of the transition operator; τ_1, τ_2 and τ_3 are slowly varying functions of the nuclear coordinates in a diabatic electronic basis [26]. This enables one to utilize the generalized Condon approximation in the photodetachment process. The choice of the diabatic electronic basis has yet another advantage that the states are coupled through the electronic part of the Hamiltonian matrix rather than the nuclear kinetic energy part as in the adiabatic electronic basis. In the latter case the nonadiabatic

coupling elements exhibit a singularity at the point of degeneracy.

The diabatic Hamiltonian of the $\Sigma - \Pi$ coupled electronic manifold of the $Cl(^2P) + H_2$ has already been discussed in Chapter 2. Here, we will discuss about the initial wavefunction $|\Psi^{anion}\rangle$ corresponding to the ground vibrational level of the ground electronic state of ClH_2^-. It is prepared in the following two ways:

(1) It is approximated to a stationary Gaussian WP (GWP) written in terms of the reagent channel Jacobi coordinates

$$\begin{aligned} |\Psi^{anion}\rangle &= N \exp\left[\frac{(R-R_0)^2}{2\sigma_R^2}\right] \exp\left[\frac{(r-r_0)^2}{2\sigma_r^2}\right] \\ &\times \left\{ \exp\left[\frac{(\gamma-\gamma_0)^2}{2\sigma_\gamma^2}\right] + \exp\left[\frac{(\gamma-\pi+\gamma_0)^2}{2\sigma_\gamma^2}\right] \right\} \end{aligned} \tag{4.3}$$

and located initially in the vicinity of the equilibrium geometry of ClH_2^- reported by Bieske *et. al* [147] at $R_0 = 6.04\ a_0$, $r_0 = 1.4\ a_0$ and $\gamma_0 = 0$ with width parameters $\sigma_R = 0.25\ a_0$, $\sigma_r = 0.25\ a_0$, and $\sigma_\gamma = 0.2$ radian along R, r and γ, respectively. The quantity N is the normalization constant. Hereafter, we refer to this WP as "initial GWP".

(2) It is calculated with the aid of a Lanczos based relaxation scheme using the vibrationally averaged potential energy surface of ClH_2^- reported by Alexander [148] at the coupled-cluster with all single and double excitation and quasiperturbative treatment of triples [CCSD(T)] level of theory. Hereafter, we refer to this WP as the "initial *ab initio* WP".

The action of the exponential operator $\exp[-i\mathcal{H}t/\hbar]$ on the initial wavefunction $|\Psi(0)\rangle$ in Eq. (4.1) is carried out by dividing the time axis into N segments of length Δt each. The exponential operator at each time step is then approximated by the split-operator method [130]. The the fast Fourier transform method [102]

is used to evaluate the action of the exponential containing the radial kinetic energy operator and the discrete variable representation method [112] is used to evaluate the exponential containing the rotational kinetic energy operator $\boldsymbol{j}^2/2I$ on the wavefunction.

The numerical calculations are carried out on a grid consisting of equally spaced points along the Jacobi distances R and r. The grid along γ is chosen as the nodes of a n-point Gauss-Legendre quadrature (GLQ) [141]. A 128×64 gird is used in the $R \times r$ plane with 0.1 $a_0 \leq R \leq$ 18.007 a_0 and 0.1 $a_0 \leq r \leq$ 9.991 a_0. The grid along the Jacobi angle γ is chosen as the nodes of a 49-point GLQ. The calculations are carried out for the total angular momentum J=0.5 and the cross terms of the centrifugal part of the Hamiltonian are not considered in this study. The WP is time evolved for a total of $\sim$ 2 ps with a time step Δt = 0.06 fs. In order to avoid any unphysical reflection or wraparounds, the high energy components of the WP reaching the grid edges at longer times are absorbed by activating a damping potentials [135] at R = 13.49 a_0 and r = 6.38 a_0.

4.3 Results and Discussion

In order to understand the origin of the two broad peaks in the experimental photodetachment spectrum of ClH_2^-, we have thoroughly examined the spectra calculated by considering all possible transitions of ClH_2^- to the uncoupled (adiabatic/diabatic) and coupled (diabatic) electronic states of ClH_2. The photodetachment spectra obtained for transitions of ClH_2^- to the uncoupled adiabatic $^2\Sigma_{1/2}$, $^2\Pi_{3/2}$ and $^2\Pi_{1/2}$ SO states of ClH_2 are shown in Figs. 4.3(a-c), respectively. The spectra in Figs. 4.3(a-c) are obtained with the initial GWP of Eq. 4.1 with parameters as stated above. The intensity in arbitrary units is plotted

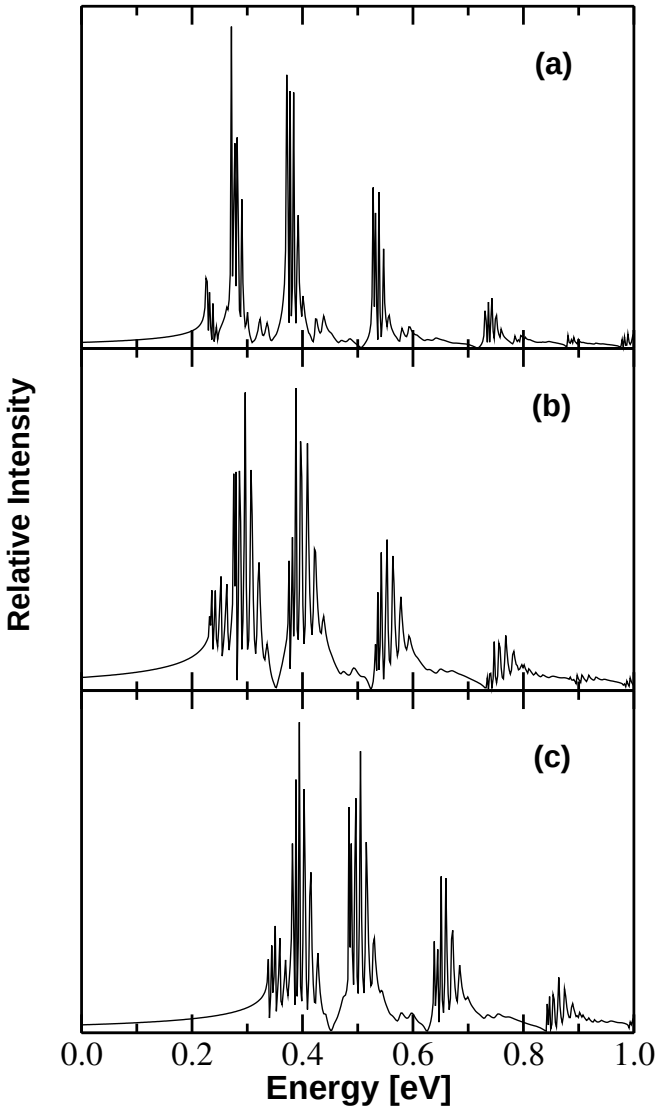

Figure 4.3: The photodetachment spectrum of ClH_2^- for a transition of the initial GWP to the uncoupled (a) $^2\Sigma_{1/2}$, (b) $^2\Pi_{3/2}$, and (c) $^2\Pi_{1/2}$ adiabatic SO states of $Cl(^2P)$ + H_2 . The intensity in arbitrary units is plotted as a function of the energy of the final electronic state E. The zero of the energy scale corresponds to the asymptotically separated Cl + H_2 on the $^2\Sigma_{1/2}$ state.

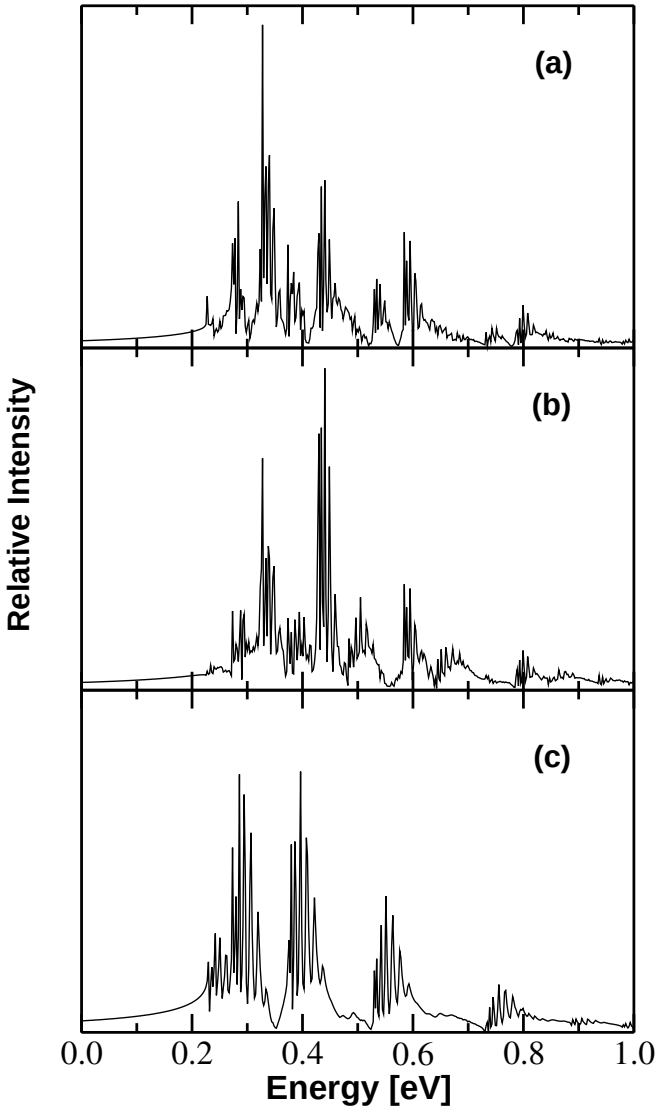

Figure 4.4: Same as Fig. 4.3. The photodetachment spectrum of ClH_2^- for a transition of the inital GWP to the coupled diabatic (a) $^2\Sigma_{1/2}$, (b) $^2\Pi_{3/2}$, and (c) $^2\Pi_{1/2}$ SO states of $Cl(^2P)$ + H_2 .

as a function of the energy of the final vibronic state. The zero of the energy scale corresponds to the asymptotically separated $Cl(^2P) + H_2$ fragments on the $^2\Sigma_{1/2}$ state. Each spectrum in Figs. 4.3(a-c) revels progression of bands separated in energy by an amount nearly equivalent to the SO splitting of the Cl atom ($\sim$ 0.1 eV). Each band consists of numerous resolved peaks presumably arising from the van der Waals progression as well as form a transition to the $Cl(^2P) + H_2$ continuum states. It can be seen that the origin of the spectral progression shifts to the higher energy in going from $^2\Sigma_{1/2}$ to $^2\Pi_{3/2}$ to $^2\Pi_{1/2}$ states. This shift for the $^2\Pi_{3/2}$ state is $\sim$ 0.015 eV relative to the $^2\Sigma_{1/2}$ sate and that for the $^2\Pi_{1/2}$ state $\sim$ 0.106 eV relative to the $^2\Pi_{3/2}$ state. These shifts can be attributed to the asymptotic splittings caused by the Σ-Π and Π-Π SO interactions in ClH_2.

Subsequently, we carried out three coupled state calculations by initially locating the WP in each of the three diabatic electronic states. The spectrum obtained for the transition to the coupled diabatic $^2\Sigma_{1/2}$, $^2\Pi_{3/2}$ and $^2\Pi_{1/2}$ SO states of ClH_2 are shown in Figs. 4.4(a-c), respectively. The resulting three coupled state spectra are then combined together to generate the final results. The spectra obtained in that way with the initial GWP and the initial *ab initio* WP are shown in Figs. 4.5(a-b), respectively. Despite a broad structure of the spectrum with the initial GWP (cf. Fig. 4.5(a)) the energetic locations of the major peaks nicely correlate with those from the initial *ab initio* WP (cf. Fig. 4.5(b)). We note that the initial *ab initio* WP is more localized in the van der Waals well region compared to the initial GWP (cf. Fig. 4.1). Therefore, the contribution from the $Cl(^2P) + H_2$ continuum states is relatively reduced in the spectrum in Fig. 4.5(b). The transition to each of the three SO states of ClH_2 contributes to the complex band structures in Figs. 4.5(a-b).

In order to better understand the coupled state results, we examined the

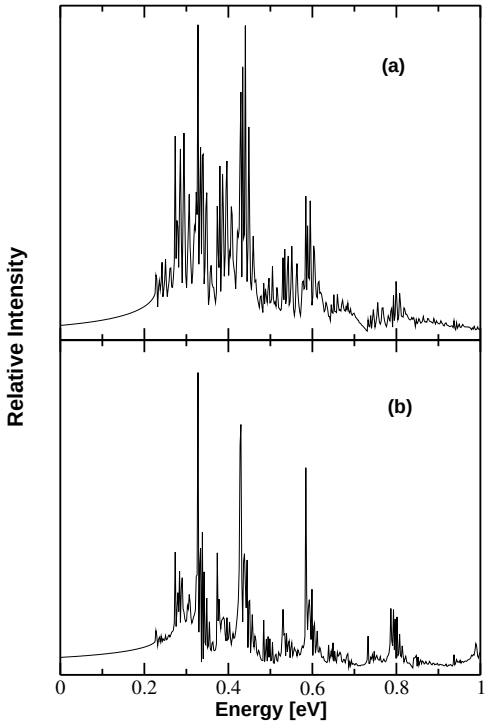

Figure 4.5: The final theoretical photodetachment spectrum of ClH_2^- obtained with (a) an initial GWP and (b) the initial *ab initio* WP. The spectrum in each panel is obtained by adding three coupled state spectra pertinent to the initial transition to each of the three SO states of $Cl(^2P)$ + H_2 shown in Fig. 4.4.

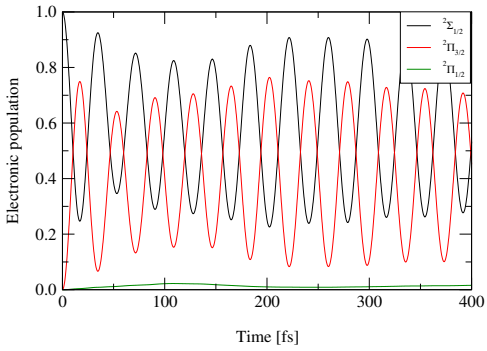

Figure 4.6: Time dependence of the electronic populations of the $^2\Sigma_{1/2}$ (solid line), $^2\Pi_{3/2}$ (dashed line) and $^2\Pi_{1/2}$ (dot-dashed line) diabats in the coupled three-state dynamics of Fig. 8. The WP is initially located on $^2\Sigma_{1/2}$ diabat.

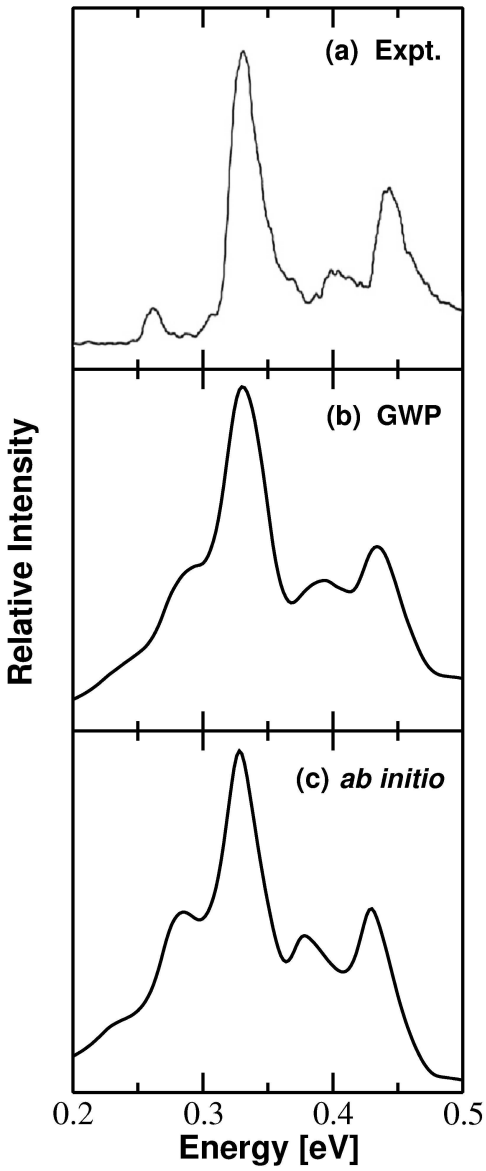

Figure 4.7: The 299 nm experimental photodetachment spectrum of ClH_2^- (panel **a**) reproduced form Ref. [64]. The theoretical results obtained with an initial GWP and an *ab initio* initial WP are shown in panel **b** and **c**, respectively. The intensity in arbitrary units is plotted as a function of energy of the final electronic state. The zero of energy corresponds to the Cl + H_2 asymptote of the $^2\Sigma_{1/2}$ state.

three partial spectra shown in Fig. 4.4 obtained in the coupled state calculations. We found that the partial spectra for the $^2\Sigma_{1/2}$ and $^2\Pi_{3/2}$ states from nearly identical progressions. The group of lines are separated by ~ 0.05 eV in energy. The peak at the origin of the coupled states results in Figs. 4.5(a-b) mostly originates from the $^2\Sigma_{1/2}$ state. The spectra for the $^2\Pi_{1/2}$ state forms quite a different progression, and here the group of lines are separated by ~ 0.10 eV in energy. For an initial transition to either the $^2\Sigma_{1/2}$ or the $^2\Pi_{3/2}$ state, the partial spectra for the $^2\Sigma_{1/2}$ and the $^2\Pi_{3/2}$ states reveal nearly comparable intensities. The intensity of the $^2\Pi_{1/2}$ partial spectra on the other hand, is found to be a factor of ~ 20 less than the other two. Similarly, the intensity of the $^2\Sigma_{1/2}$ and $^2\Pi_{3/2}$ spectra is found to be a factor of ~ 20 less than the $^2\Pi_{1/2}$ spectra for an initial transition to the $^2\Pi_{1/2}$ state. Similar observations follow when the time-dependence of the diabatic electronic populations are examined (Fig. 4.6). The diabatic populations of the $^2\Sigma_{1/2}$ and $^2\Pi_{3/2}$ revel quasiperiodic recurrences ~ 36 fs spaced in time. A considerable exchange of population between the $^2\Sigma_{1/2}$ and $^2\Pi_{3/2}$ states is observed. The population exchange with the $^2\Pi_{1/2}$ state on the other hand, is significantly smaller. This indicates that the coupling between the $^2\Sigma_{1/2}$ and $^2\Pi_{3/2}$ states is much stronger than their coupling with the $^2\Pi_{1/2}$ state. We find that the Σ-Π Vibronic coupling has essentially no effect on the spectrum. Each of the coupled state spectra revels broadening of the bands when compared with the uncoupled diabatic results (not shown here). This broadening solely arises from an increase in the line density in the coupled state spectra caused by the nonadiabatic effects due to SO coupling.

4.3.1 Photodetachment spectra: Comparison with the Experiment

In order to compare with the broad band experimental envelope of Ref. [64] the theoretical spectra shown in Figs. 4.5(a) and 4.5(b) are convoluted separately with a Lorentzian function of 20 meV full width at the half maximum (FWHM). The two convoluted spectra thus obtained with the initial GWP and the initial *ab initio* WP are shown in Figs. 4.7(b-c), respectively, along with the experimental results [64] in Fig. 4.7(a). The relative hight of the two major peaks in the theoretical spectra are adjusted according to the experimental results. This adjustment was necessary as we have assumed constant values for the transition dipole matrix elements in our study.

In the experimental results of Neumark and coworkers [64] the first small peak is attributed to a detachment due to the Cl^- and that between the two large peaks is due to the $Cl(H_2)_2^-$. The two large peaks are spaced $\sim$ 0.111 eV in energy which is nearly identical to the Cl SO splitting of $\sim$ 0.109 eV. The theoretical peak widths of ... meV and ... meV compare well with the experimental results of 26 meV and 23 meV, respectively. The peaks obtained with the initial GWP (cf. panel *b*) are slightly broader than those with the *ab initio* WP (cf. panel *c*) which is also indicated by the spectra presented in Figs. 4.5(a-b). The two shoulder peaks (one at low energy and the other in between the large peaks) are found to get intensity mostly from the transition to the $^2\Pi_{1/2}$ state. The individual peak structures are very complex and each peak originates from highly overlapping transitions to all the SO states of ClH_2. As stated above, the two shoulder peaks have major contributions from the SO excited $^2\Pi_{1/2}$ state of ClH_2. The major contribution to the first large peak comes from transitions to the $^2\Sigma_{1/2}$ and $^2\Pi_{3/2}$ states. The contribution from the transition to the $^2\Pi_{1/2}$ SO

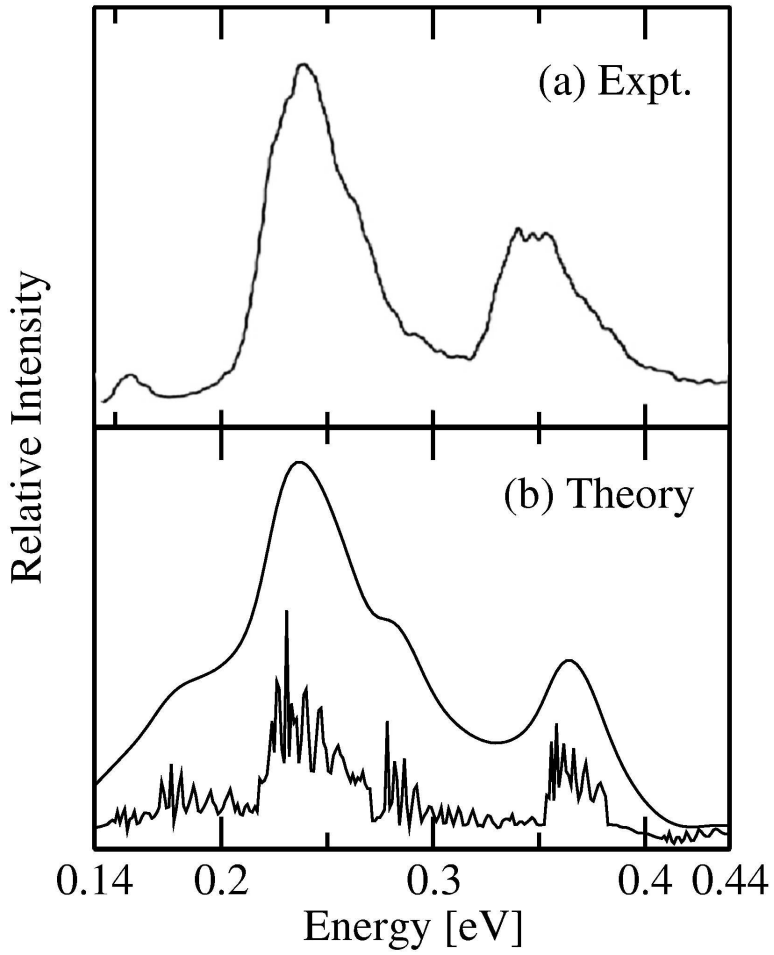

Figure 4.8: The photodetachment spectrum of ClD_2^-. The 299-nm experimental results are reproduced from Ref. [64] and shown in the top panel. The time-dependent WP results at low and high resolution are shown in the bottom panel. The relative intensity is plotted in arbitrary units as a function of the energy of the final electronic state. The zero of energy corresponds to the asymptotically separated Cl + D_2 fragments on the $^2\Sigma_{1/2}$ adiabatic state.

states is negligible in this peak. On the other hand, the major contribution to the second large peak comes from the transition to the $^2\Pi_{3/2}$ SO state and the contributions from the transitions to the $^2\Sigma_{1/2}$ and $^2\Pi_{1/2}$ SO states are of comparable magnitude in this case.

The calculated photodetachment spectrum of ClD_2^- along with the experimental results of Neumark and coworkers [64] is shown in Fig. 4.8(a-b). The relative intensity in arbitrary units is plotted as a function of the energy of the final electronic manifold in electron volts. The theoretical spectrum is obtained in the same way as in the case of ClH_2^-. The spectra pertinent to a transition to each of the $^2\Sigma_{1/2}$, $^2\Pi_{3/2}$ ans $^2\Pi_{1/2}$ diabatic electronic states in the coupled state situation are calculated. The resulting three partial spectra are then combined together and convoluted with a Lorentzian function of 24 meV FWHM to calculate the spectral envelope shown in Fig. 4.8(b). The convergence of the three partial spectra is checked by varying the length of the time propagation and also the width of the absorbing region along R and r. The spectrum shown in Fig. 4.8(b) is obtained by propagating the WP for a total of $\sim$ 1.8 ps with a time step of $\sim$ 0.109 fs. The width of the absorbing potential is set to 7.84 a_0 and 3.92 a_0 along R and r, respectively. It can be seen from Fig. 4.8(b) that the theoretical results are in good accord with the experimental observations. But despite a good overall agreement between the theoretical and experimental results the separation between the peak maxima is $\sim$ 0.03 eV higher in the theoretical results. It is to be noted that the theoretical result is obtained by propagating WP and it is known that spectrum generated by this method is usually associated with background contributions arising from the direct dissociative component of the WP. This problem becomes even more severe as majority of the quasibound states have the feature of a continuum state. Therefore, a part of the difference

between the theoretical and experimental results in Fig. 4.8(b) can be attributed to this. A second source for the difference can be attributed to the approximate adjustment of the transition dipole matrix elements which are assumed to be constants and to the accuracy of the neutral electronic PESs and their coupling surfaces as well as the initial wavefunction of ClD_2^- which has been approximated to a stationary GWP in the present study. The equilibrium geometry of ClD_2^- occurs at somewhat shorter (by $\sim$ 0.1 a_0) distance than ClH_2^- along R. As a result, the WP in case of the transition on ClD_2^- samples relatively more of the repulsive part of the SO states of ClD_2.

A similar peak structures have been reported by Manolopolous and Alexander in the FC simulation of the ClH_2^- and ClD_2^- spectrum [152]. Analogous to the ClH_2^- spectrum [cf. Fig. 4.5] ClD_2^- spectrum also reveals series of peaks which can be attributed to the progression along the R and γ coordinates. In the next section, we examine the individual peaks obtained at higher energy resolution (dynamical resonanaces) in the Cl + H_2 system in details.

4.3.2 Calculation of resonances by a spectral quantization approach

The resonances in the Cl(^2P) + H_2 reaction is investigated in details by spectral quantization method (SQM). This method was proposed by Feit *et al.* [104] for computing the bound state eigenvalues and eigenfunctions by solving the TDSE. In this method, a stationary GWP, $\Psi(0)$, is located initially in the interaction region of the PES. The WP in time t, $\Psi(t)$, is obtained by evolving $\Psi(0)$ in space and time using the formalism dicussed in Sec. 2.5. The temporal autocorrelation function $C(t) = \langle\Psi(0)|\Psi(t)\rangle$, is computed at various time intervals and Fourier

transformed to generate the power spectrum:

$$I(E) \approx Re \int_0^\infty C(t) e^{iEt/\hbar} dt, \tag{4.4}$$

where, $I(E)$ is the spectral intensity. The peaks in the power spectrum arise from the quasibound states of the system and the energy value corresponding to the peak maxima determine their eigenvalues. The accurate eigenvalues are extracted by fitting each peak to a Lorentzian line-shape function

$$Y(E) = Y_0 + \frac{2A}{\pi} \frac{w}{4(E - E_0)^2 + w^2}. \tag{4.5}$$

The peaks are generally contaminated by an overlap with the neighboring states and an estimate of the line-width often becomes cumbersome and difficult. Whenever a peak is fitted reasonably well, the line-width lifetime τ_n is calculated from the full width at the half maximum (FWHM) w of the Lorentzian function by, $\tau_n = \hbar/w$.

Once the eigenvalue of a peak is determined the corresponding eigenfunction is then calculated by the spectral quantization algorithm: by projecting a time-evolved WP onto the desired eigenstate (n) with eigenvalue E_n,

$$\Psi_n(E) \approx \int_0^T e^{iE_n t/\hbar} \Psi(t) dt. \tag{4.6}$$

We first calculate the pseudospeectra for the uncoupled diabatic and adiabatic $^2\Sigma_{1/2}$ surface. The genuineity of different peaks in the pseudospectrum is confirmed by varying the initial location of the WP in the mentioned regions of the PES. Resonances originating from the van der Waals well region of the PESs reveal extended progression along the Cl...H_2 van der Waals coordinate.

In addition, we also examined the resonances arising from the TS region of the $^2\Sigma_{1/2}$ PES of ClH_2. Subsequently, we carried out coupled states calculations by considering the electronic and also the electronic plus SO coupling separately and investigated their role on the overall vibronic structure of each SO states. In the coupled state picture the dynamics is studied throughout in a diabatic representation. All the calculations are carried out for the lowest value of the total angular momentum J, for both the uncoupled and coupled state situations. Finally, the role of the surface coupling on the individual eigenstates of the $^2\Sigma_{1/2}$ adiabatic states is examined and the corresponding time-dependent dynamics is discussed.

4.3.3 Resonances of $Cl(^2P) + H_2$ reaction in the uncoupled adiabatic and diabatic representation

In order to carry out a detailed investigation of the resonances in $Cl(^2P) + H_2$ system, we first report the energy level spectrum of the uncoupled $^2\Sigma_{1/2}$, $^2\Pi_{3/2}$ and $^2\Pi_{1/2}$ adiabatic and diabatic CW PESs. We note that the primary aim of this study is to examine the surface coupling effects on the eigenstates of the $^2\Sigma_{1/2}$ adiabatic state which are important for the $Cl(^2P) + H_2$ reaction dynamics. The eigenstates of the component Π states are considered here only briefly. The calculations are carried out by locating the initial GWP in the van der Waals region of these surfaces as well as in the barrier (TS) region of the $^2\Sigma_{1/2}$ PES. The initial locations and the width parameters of the GWPs used in various calculations reported here are given in Table 4.1. We note that locating the initial WP at $\gamma^\circ = \pi/2$ for a particular value of R° and r° yields identical energy spectrum as for $\gamma^\circ = 0$ or π. The relative intensity of the peaks is only different in the two. In view of the fact that the photodetachment of ClH_2^- samples the collinear configurations of the ClH_2 PESs initially, we here show the

Table 4.1: Parameters for the different choices of the initial Gaussian wave packet used in time evolution.

GWP	R_0 (a_0)	r_0 (a_0)	γ_0 (rad)	δ_R (a_0)	δ_r (a_0)	δ_γ (rad)	$\langle E \rangle$ (eV)
1	5.58	1.402	0.0	0.28	0.24	0.2	0.4868
2	6.04	1.402	0.0	0.25	0.25	0.2	0.4827
3	6.11	1.402	0.0	0.28	0.24	0.2	0.4698
4	6.26	1.402	0.0	0.25	0.24	0.2	0.4733
5	6.56	1.402	0.0	0.25	0.24	0.2	0.4697
6	3.658	1.814	0.0	0.3	0.4	0.2	0.6164
7	4.475	2.049	0.0	0.4	0.3	0.2	1.0381
8	4.599	2.136	0.0	0.3	0.4	0.2	1.2106
9	4.475	2.409	0.0	0.3	0.4	0.2	1.3137
10	4.843	2.387	0.0	0.3	0.4	0.2	1.6763

results obtained by locating the initial wave packet at γ=0 or π.

The pseudospectra obtained by initially locating the GWP No. 2 and 7 on the $^2\Sigma_{1/2}$ adiabat are shown in Figs. 4.9(a) and 4.9(b), respectively. The spectra are obtained through Eq. 4.4 and the decay of the corresponding autocorrelation functions is included as an insert in the respective figures. The peaks in Fig. 4.9(a) correspond to the progression of low-energy van der Waals resonances arising from the shallow well region of the Cl + H_2 asymptote, whereas, those in the Fig. 4.9(b) correspond to the high energy resonances arising from the barrier region of the PES. Location of the initial WP on the PES corresponds to an average energy $\langle E \rangle$ = 1.038 eV for the spectrum in Fig. 4.9(b). This leads to resolved structure of the high energy peaks in the spectrum. The low energy peaks are also obtained with this WP but are much less resolved than in Fig. 4.9(a). The analysis of the individual peaks of Figs. 4.9(a-b) is discussed below.

The pseudospectra obtained with the GWP No. 2 and 7 on the $^2\Sigma_{1/2}$ diabat

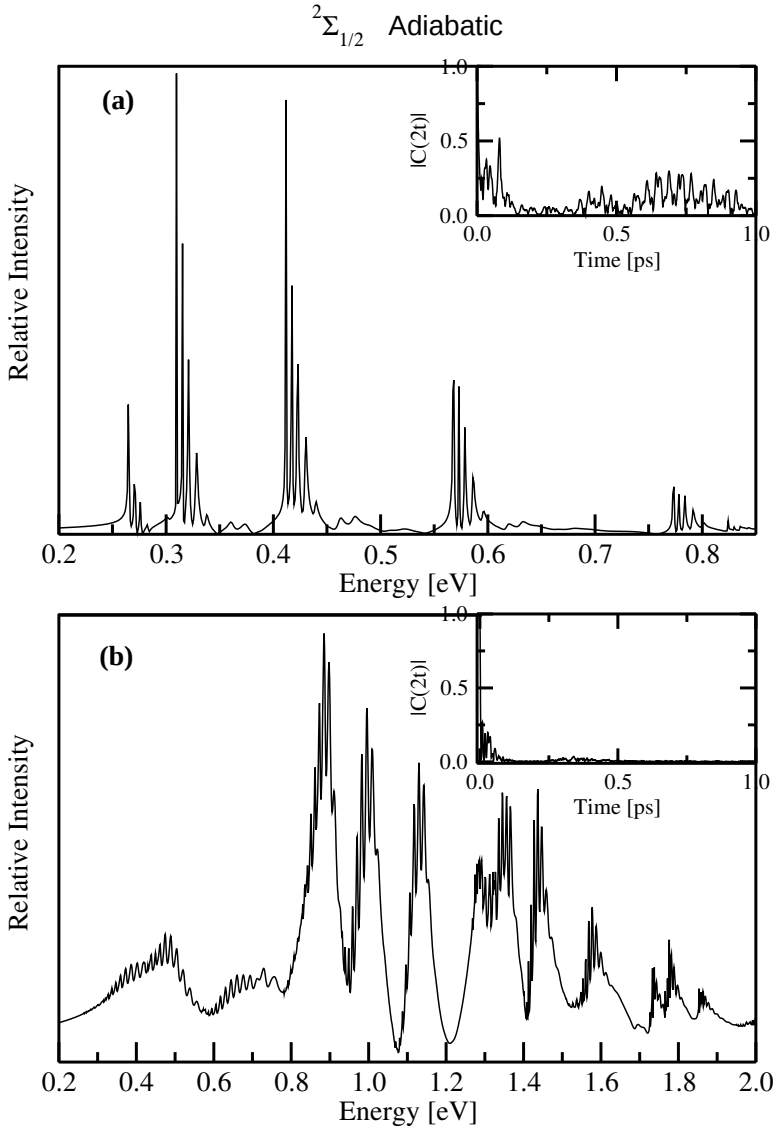

Figure 4.9: The pseudospectrum of the quasibound states of the uncoupled $^2\Sigma_{1/2}$ adiabatic electronic state of ClH_2. The two spectra in panel (a) and (b) are obtained with the GWP No. 2 and 7, respectively. The intensity in arbitrary units is plotted as a function of the energy of the $^2\Sigma_{1/2}$ electronic state. The energy corresponding to peak maxima represents the eigenvalue of the quasibound states. The zero of energy corresponds to the asymptotically separated Cl + H_2 species on the $^2\Sigma_{1/2}$ electronic state. The decay of the absolute value of the corresponding autocorrelation function $|C(2t)|$ in time, is shown as an insert in the respective panels.

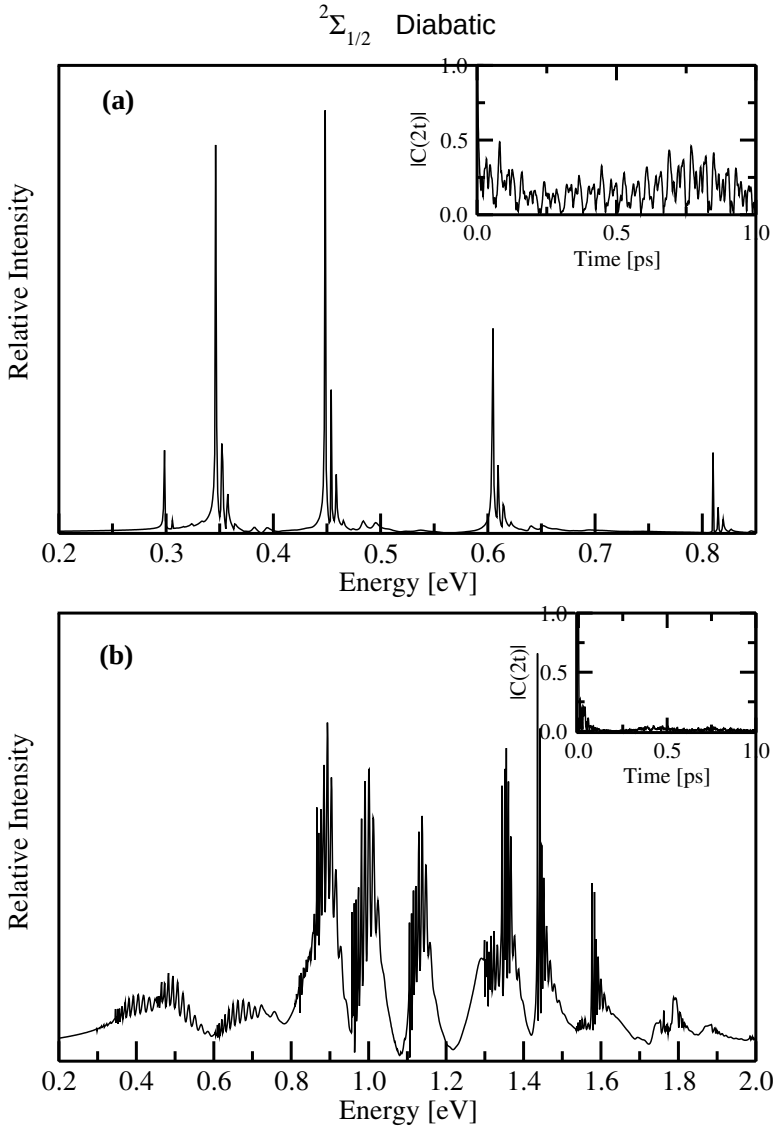

Figure 4.10: Same as in Fig. 2, for the uncoupled $^2\Sigma_{1/2}$ diabatic electronic state.

are shown in Figs. 4.10(a-b). The decay of the corresponding autocorrelation function is also included as an insert in the respective panel. It can be seen from Fig. 4.10(a) that the low-energy diabatic spectrum is less structured than the corresponding adiabatic spectrum shown in Fig. 4.9(a). The high energy spectrum in Fig. 4.10(b) resembles more closely to that in Fig. 4.9(b). However, the high energy diabatic spectrum in Fig. 4.10(b) is relatively more structural than the corresponding adiabatic spectrum in Fig. 4.9(b). The differences between the adiabatic and diabatic results may be due to the fact that a diabatic state represents an admixture of the adiabatic states. The extent of mixing depends on the nuclear coordinates, which is different for the location of the initial WP in the van der Waals well and the barrier regions of the PES. We note that although we calculate the diabatic $^2\Sigma_{1/2}$ spectra for comparison; we will concentrate on the more realistic adiabatic $^2\Sigma_{1/2}$ spectra (cf. Fig. 4.9(a-b)) in the rest of our discussions.

We also calculated the adiabatic and diabatic $^2\Pi_{3/2}$ and $^2\Pi_{1/2}$ spectra. These two surfaces are closed along the channel leading to the ground state products. Therefore, the vibrational structure of the spectrum obtained on these surfaces reveals the spectroscopy of the reagent van der Waals well region only. The resulting spectra show analogous vibrational structure as seen in the low energy $^2\Sigma_{1/2}$ spectra in Fig. 4.9(a) and Fig. 4.10(a). We note that the adiabatic results for the component $^2\Pi$ state has been shown Fig. 4.3 in the previous section. The spectra reveal progression of envelopes and the fine structures under each envelope correspond to the progression along the $Cl\cdots H_2$ dissociation coordinate. An energy shift of ~ 0.1 eV of the 0-0 peak corresponding to the SO splitting of the component Π states has been observed in the two spectra. The spectra for the component $^2\Pi$ state do not reveal any structure at high energies. As mentioned

above, these two states are closed along the r coordinate. This also explains the much similarity observed for the $^2\Sigma_{1/2}$ adiabatic (cf. Fig. 4.9(b)) and diabatic (cf. Fig. 4.10(b)) results at high energies.

4.3.3.1 Resonances of the uncoupled $^2\Sigma_{1/2}$ adiabatic state

The quasibound spectrum of the $^2\Sigma_{1/2}$ adiabatic electronic state is the most crucial governing factor of the outcome of the $Cl(^2P) + H_2$ reaction. Since the adiabatic electronic representation gives the realistic description of the observables in an experiment, in this section we make an effort to analyze the peaks observed in the adiabatic $^2\Sigma_{1/2}$ spectra shown in Figs. 4.9(a-b). We mention that apart from the two spectra shown in Figs. 4.9(a-b), we have computed a number of additional spectra by varying the initial location of the GWP (as described in table 4.1) in order to check the commonality of peaks observed in different spectra. The peak energies and widths are computed by fitting them to a Lorentzian line-shape function and their eigenvectors are computed by the spectral quantization algorithm as described in sec. 4.3.2. The minimum of the van der Waals well on the $^2\Sigma_{1/2}$ adiabatic state occurs at a C_{2v} configuration of ClH_2 at $R \sim 5.78\ a_0$. The low-energy spectrum shown in Fig. 4.9(a) corresponds to the vibrational structure of the prereactive van der Waals complex. The barrier on the $^2\Sigma_{1/2}$ adiabatic state, on the other hand, occurs at the collinear configuration of ClH_2 and a shorter value of $R \sim 3.631\ a_0$ [81]. Therefore, the peaks observed in the spectrum in Fig. 4.10(b) is expected to reveal the spectroscopy of the TS region of the $^2\Sigma_{1/2}$ electronic state.

The energy eigenvalue and lifetime of the resonances extracted from various spectra (calculated in the present study) are collected in table 4.2. We note that a blank entry in table 4.2 represents an uncertainty in estimating the corresponding

TABLE 2: Eigenvalues (E_n's), Assignments, and the Line Width Lifetime of the Quasi-Bound States of ClH_2 on the $^2\Sigma_{1/2}$ Adiabatic Electronic State[a]

eigenvalue (eV)	assignment (n_R,n_r,n_γ)	lifetime (fs)	eigenvalue (eV)	assignment (n_R,n_r,n_γ)	lifetime (fs)
0.264	(0,0,0)		0.885	(7,1,2)	87
0.271	(1,0,0)		0.899	(8,1,2)	62
0.275	(2,0,0)		0.912	(9,1,2)	44
0.283	(3,0,0)	38	9.22	(0,1,4)	
0.310	(0,0,2)		0.928	(1,1,4)	
0.315	(1,0,2)	173	0.932	(2,1,4)	
0.320	(2,0,2)	145	0.940	(3,1,4)	
0.327	(3,0,2)	221	0.948	(4,1,4)	121
0.339	(4,0,2)	93	0.959	(5,1,4)	186
0.347	(5,0,2)		0.970	(6,1,4)	126
0.362	(6,0,2)	117	0.983	(7,1,4)	111
0.375	(7,0,2)	102	0.997	(8,1,4)	73
0.387	(8,0,2)	82	1.011	(9,1,4)	67
0.404	(9,0,2)	60	1.022	(0,0,10)	
0.411	(0,0,4)	500	1.026	(1,0,10)	
0.417	(1,0,4)	308	1.032	(2,0,10)	
0.423	(2,0,4)		1.040	(3,0,10)	
0.431	(3,0,4)	245	1.051	(4,0,10)	150
0.441	(4,0,4)	80	1.070	(0,1,6)	
0.450	(5,0,4)	158	1.080	(2,1,6)	
0.465	(6,0,4)		1.088	(3,1,6)	
0.478	(7,0,4)	194	1.097	(4,1,6)	
0.490	(8,0,4)	91	1.107	(5,1,6)	197
0.506	(9,0,4)	91	1.118	(6,1,6)	118
0.522	(10,0,4)	54	1.131	(7,1,6)	99
0.568	(0,0,6)	232	1.144	(8,1,6)	
0.573	(1,0,6)		1.156	(9,1,6)	45
0.579	(2,0,6)	267	1.264	(0,1,8)	
0.587	(3,0,6)	160	1.270	(1,1,8)	
0.596	(4,0,6)		1.276	(2,1,8)	
0.605	(5,0,6)	307	1.282	(3,1,8)	
0.621	(6,0,6)	121	1.293	(4,1,8)	
0.635	(7,0,6)	132	1.131	(5,1,8)	103
0.668	(8,0,6)	45	1.325	(6,1,8)	27
0.684	(9,0,6)	68	1.336	(7,1,8)	233
0.773	(0,0,8)		1.346	(8,1,8)	169
0.778	(1,0,8)		1.356	(9,1,8)	91
0.784	(2,0,8)		1.401	(0,2,4)	
0.792	(3,0,8)		1.408	(1,2,4)	
0.824	(0,1,2)		1.414	(2,2,4)	
0.829	(1,1,2)	158	1.425	(3,2,4)	
0.835	(2,1,2)		1.427	(4,2,4)	228
0.844	(3,1,2)	132	1.437	(5,2,4)	119
0.851	(4,1,2)	115	1.448	(6,2,4)	68
0.862	(5,1,2)	197	1.460	(7,2,4)	53
0.873	(6,1,2)		1.473	(8,2,4)	22

[a] A blank entry indicates the corresponding quantity could not be determined unambiguously.

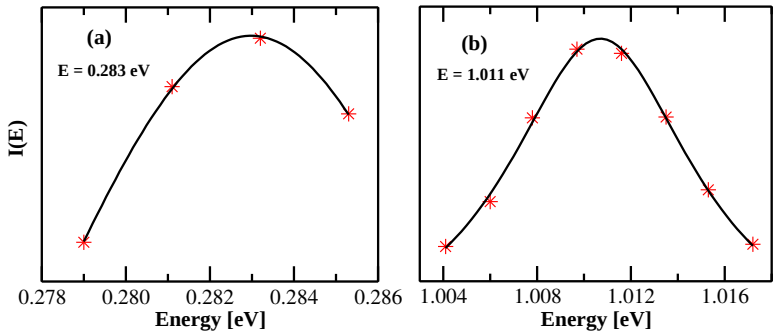

Figure 4.11: Lorentzian line shapes for the two typical spectral peaks centered at $E = 0.283$ eV and $E = 1.011$ eV, shown by the solid curve in panel (a) and (b), respectively. The results obtained from the time-dependent WP calculations are shown by the asterisks. While the peak in panel (a) represents the case where the energy eigenvalue can be estimated accurately but width can not be, the one in panel (b) represents the case where both these quantities can be determined with reasonable accuracy.

peak width. Lorentzian line-shape fittings of two typical peaks are shown in Figs. 4.11(a-b). The asterisks in the figure represents the computed points while the solid curves represent the best-fit Lorentzian. The fitting in Fig. 4.11(a) represents a difficult situation where the energy eigenvalue corresponding to the peak maximum can be extracted, however, the peak width can not be reliably estimated. The fitting shown in Fig. 4.11(b), on the other hand represents the situation where both the parameters can be reliably estimated.

The eigenfunction of a few representative resonances of the uncoupled $^2\Sigma_{1/2}$ adiabatic state are shown in Figs. 4.12(a-n) and in Figs. 4.13(a-h). While the eigenfunctions in Figs. 4.12(a-n) represent the low-energy van der Waals resonances, those in Figs. 4.13(a-h) represent the high-energy resonances arising from the TS region of the PES. Eigenfunctions are plotted in terms of the probability density ($|\Psi|^2$) contours in the (R, r) and (γ, R) plane averaged over γ and r, respectively, in order to clearly identify their nodal pattern revealing the

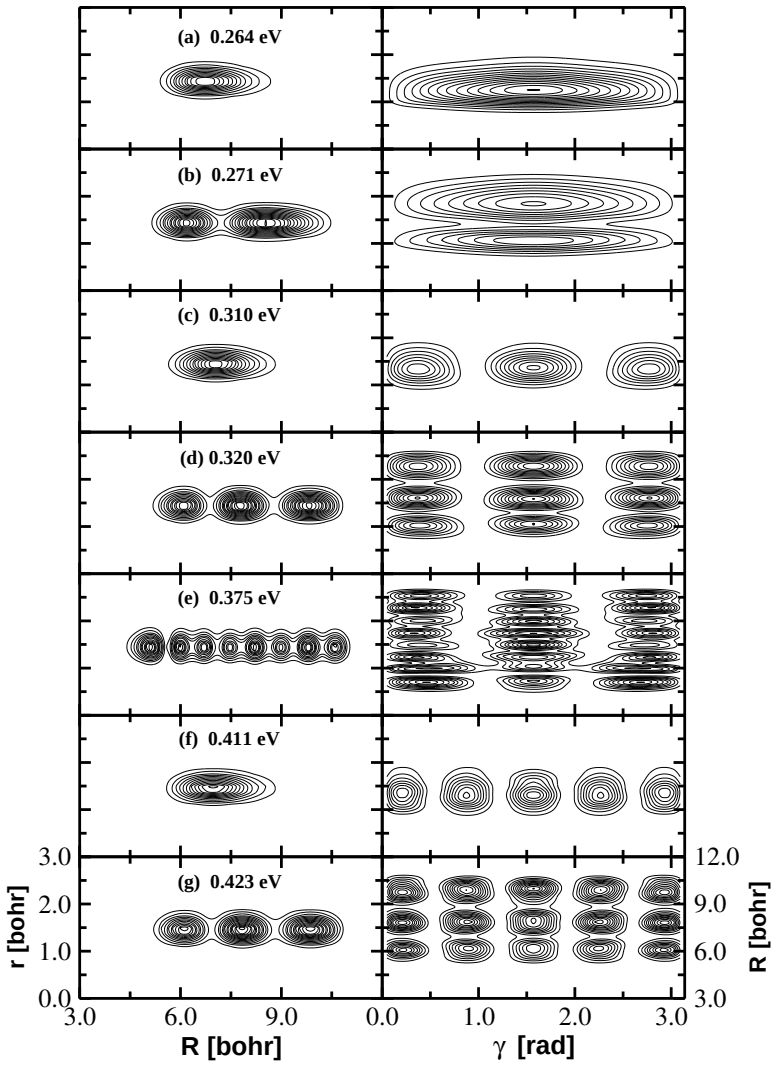

Figure 4.12: Probability density contours of the quasibound eigenfunctions obtained through the spectral quantization algorithm [Eq. (4.6)]. The energy eigenvalues of the quasibound states are indicated in the respective panel and the contour plots are shown both in the (R, r) and (γ, R) planes for average values of γ and r, respectively.

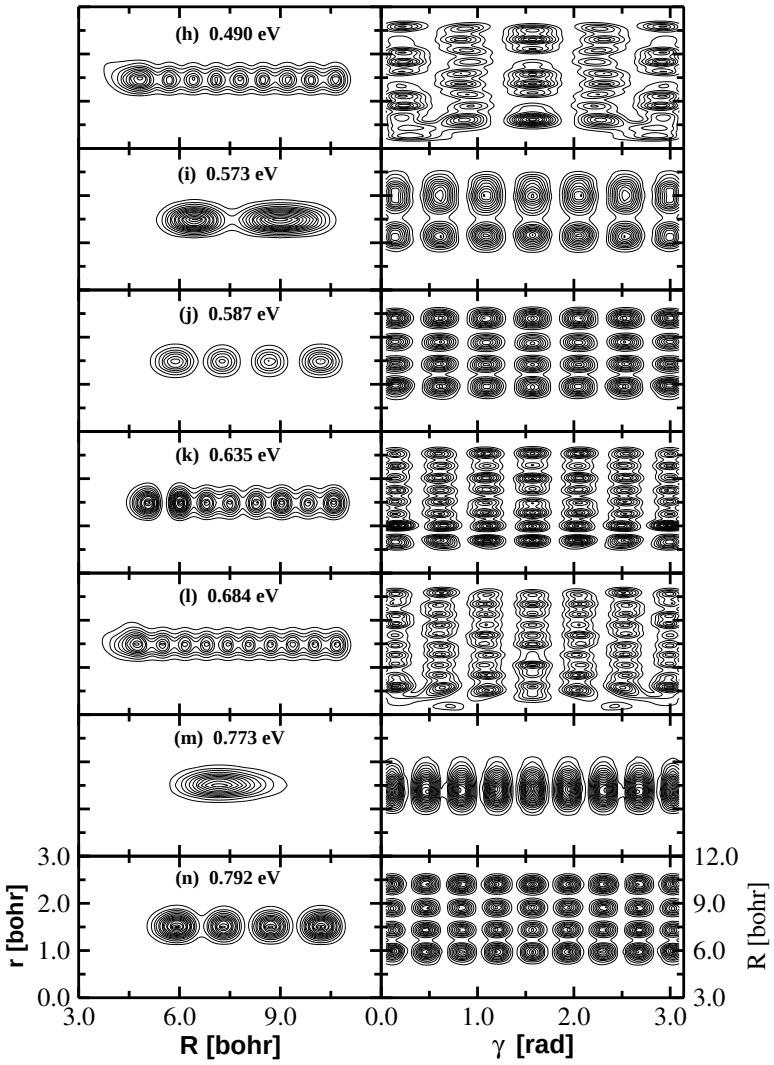

Fig. 4.12 continued.

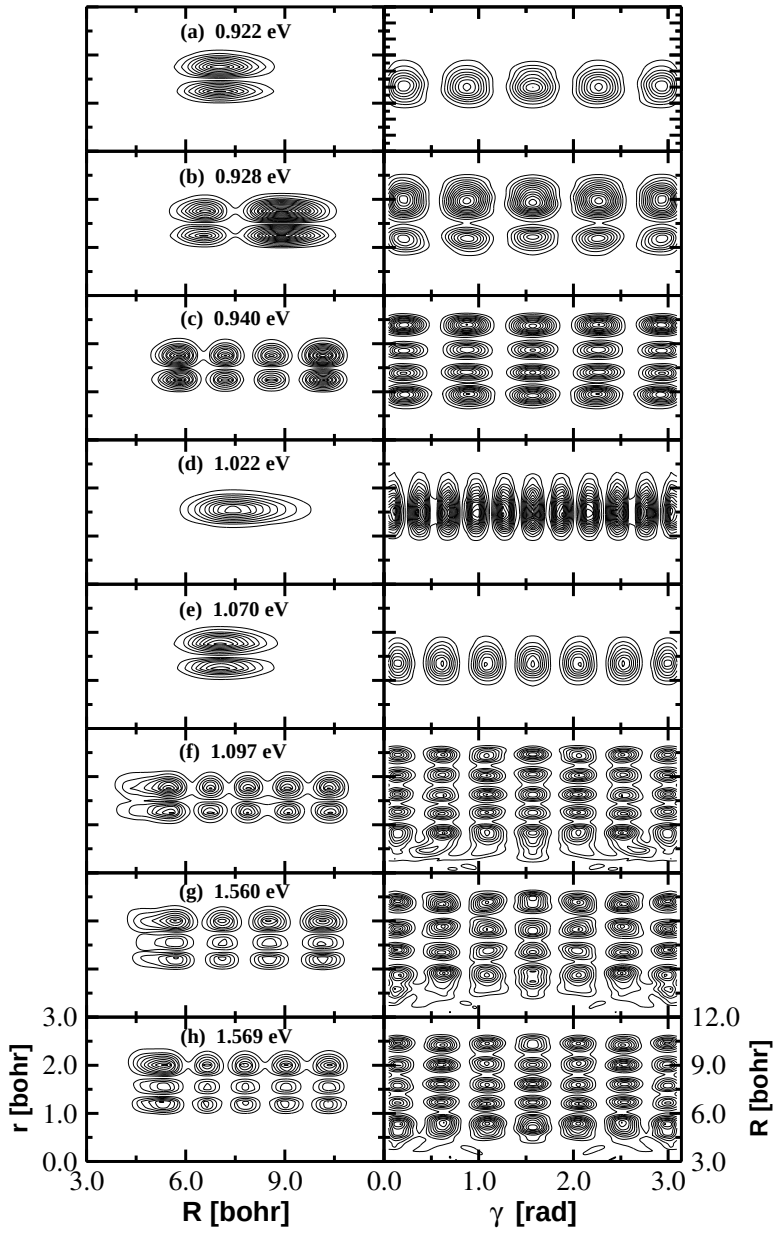

Figure 4.13: Same as Fig. 4.12.

progression of the resonances. Each features of the eigenvalue spectra (cf. Figs. 4.9(a-b)) can be associated with a stationary wave function. All the eigenstates documented in table 4.2 are assigned by inspecting their nodal pattern along R, r and γ. They are identified in terms of three quantum numbers n_R, n_r and n_γ representing the number of nodes along these coordinates, respectively. We note that we show plots of only a few eigenstates here, in order to discuss the details. The eigenfunction in Fig. 4.12(a) has no node along R, r or γ and therefore represents the (0, 0, 0) state according to the (n_R, n_r, n_γ) assignment. It is interesting to see that the probability maximum of this function occurs at a stretched configuration of ClH_2 along R ($6.0 \leq R \leq 7.5$ a_0), indicative of the van der Waals nature of the interaction along this coordinate. A heavy build up of the probability density at $\gamma = \pi/2$ can be seen from the (γ, R) plot. This indicates that the van der Waals minimum occurs at the bent configuration of ClH_2. Furthermore, the wavefunction is highly diffuse along γ. The eigenfunction in Fig. 4.12(b) has one node along R and no nodes along r and γ. It is a (1,0,0) state. The next eigenfunction (Fig. 4.12(c)) has two nodes along γ and is a (0,0,2) state. We note that, even quantum progression is only observed along the angle γ. The latter represents the bending motion of the ClH_2 complex. For each values of n_γ we find an envelope with fine structures in Fig. 4.9. The fine structures within each envelope reveal progression along the R coordinate. This is illustrated by the eigenfunctions in Figs. 4.12(d) and 4.12(e). For each of these two functions n_γ=2, whereas, n_R=2 for the former and n_R=7 for the latter. The next three eigenstates in Figs. 4.12(f-h) have four quantum excitation along γ i.e. n_γ=4. The next four eigenstates (c.f. Figs. 4.12(i-l)) correspond to n_γ=6. The eigenstate in Fig. 4.12(i) is a (1,0,6) state and those in Figs. 4.12(j), 4.12(k) and 4.12(l) are (3,0,6), (7,0,6) and (9,0,6) states, respectively. The eigenstates in

Figs. 4.12(m) and 4.12(n) have eight quantum excitation along γ and represent the (0,0,8) and (3,0,8) states, respectively.

It can be seen that none of the mentioned eigenstates above reveal a progression along r coordinate. The latter represents the vibrational motion of the H_2 moiety. In Figs. 4.13(a-h) we show some representative eigenfunctions obtained from the peaks observed at the high-energy part of the Figs. 4.9(a-b). The eigenstate in Fig. 4.13(a) reveal one quantum excitation along H_2 vibrational coordinate and may be assigned as (0,1,4) state. When compared with the (0,0,4) state in Fig. 4.12(f) one can see that this state is $\sim$ 0.5 eV higher in energy corresponding to the v=0 $\rightarrow$ v=1 vibrational excitation of H_2. The eigenstates in Figs. 4.13(b) and 4.13(c) occurs under the same envelope with the one in Fig. 4.13(a). They all have n_γ =4 and reveals a progression along the R motion. The other eigenstates in Figs. 4.13(d-h) represent (0,0,10), (0,1,6), (4,1,6), (3,2,6) and (4,2,6) states, respectively, according to the (n_R, n_r, n_γ) assignment. We note that, the overall structure of most of the eigenstates described in Figs. 4.12 and 4.13 reveals the feature of a continuum wavefunction when viewed along R and γ coordinates.

4.3.4 The effect of electronic and SO coupling

In this section we will discuss on the effects of the electronic and SO coupling on the spectra discussed above. For the low-energy part of the spectra, these effects have been discussed in Sec. 4.3 dealing with the photodetachment of ClH_2^-. Therefore, we here concentrate on the high-energy part of the spectra. We note that a diabatic electronic representation is utilized throughout in calculating the coupled states spectra. This is primarily to restore an uniformity, because for the 3×3 coupled states problem, an acceptable definition of the adiabatic-

to-diabatic transformation matrix is still a complicated issue. Therefore, the uncoupled diabatic spectra shown above are to be considered when comparing with the coupled state results presented below.

The coupled $^2\Sigma_{1/2}$ diabatic spectra are presented in Figs. 4.14(a-b). These spectra are obtained with the GWP No. 7, and the corresponding uncoupled $^2\Sigma_{1/2}$ diabatic spectrum is shown in Fig. 4.10(b). The spectra in Fig. 4.14(a) and 4.14(b) are obtained by considering the electronic (only) and electronic plus SO coupling, respectively. It can be seen by comparing Fig. 4.14(a) with that of the uncoupled state spectrum of Fig. 4.10(b), that the electronic coupling does not have any noticeable impact on the spectrum. On the other hand, the spectrum becomes more diffuse and structureless with the inclusion of the SO coupling in the dynamics. This reveals that the nonadiabatic effects due to SO coupling is stronger in the Cl(^2P) + H_2 dynamics. This leads to a considerable mixing of the interacting electronic states and an increase of the line density in the spectrum. Due to the appearance of numerous closely spaced lines the spectral envelope appears to be more diffuse and structureless.

4.3.5 Time-dependent dynamics of the adiabatic $^2\Sigma_{1/2}$ quasibound states

In order to investigate the effects of electronic and SO coupling on the quasibound states of the $^2\Sigma_{1/2}$ adiabat more closely, we examine their time-evolutions in the uncoupled and coupled state situations. In Figs. 4.15(a-h) we show the eigenvalue spectrum and the survival probability ($|C(t)|^2$) of four quasibound states corresponding to resonances indicated in the respective panel. The survival probability of the resonance in panel (a) is shown in panel (b), the one of panel (c) is shown in panel (d) and so on. In each panel the solid line indicates the result

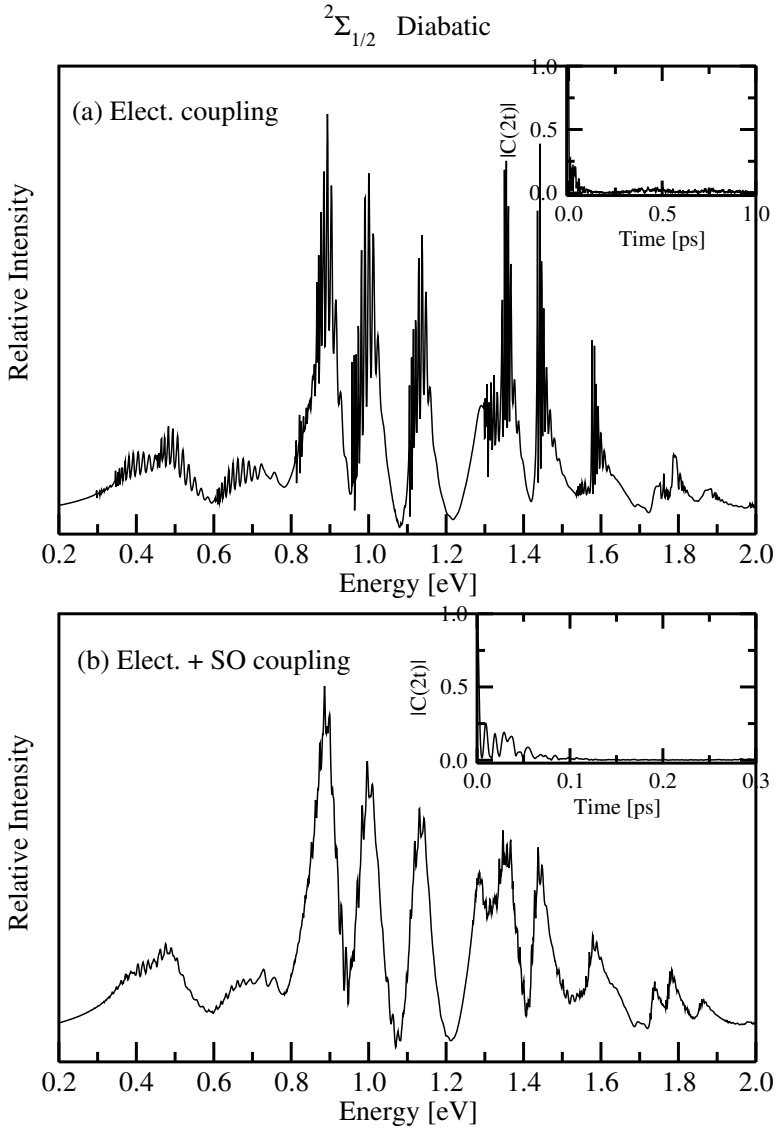

Figure 4.14: Quasibound spectrum of the $^2\Sigma_{1/2}$ diabatic electronic state in the coupled state situation obtained with the GWP No. 7. The spectrum in panel (a) is calculated by considering the Σ-Π electronic coupling only. The spectrum in panel (b) on the other hand is calculated by considering both the electronic and SO coupling. The decay of the absolute value of the corresponding $C(2t)$ is shown as an insert in the respective panels.

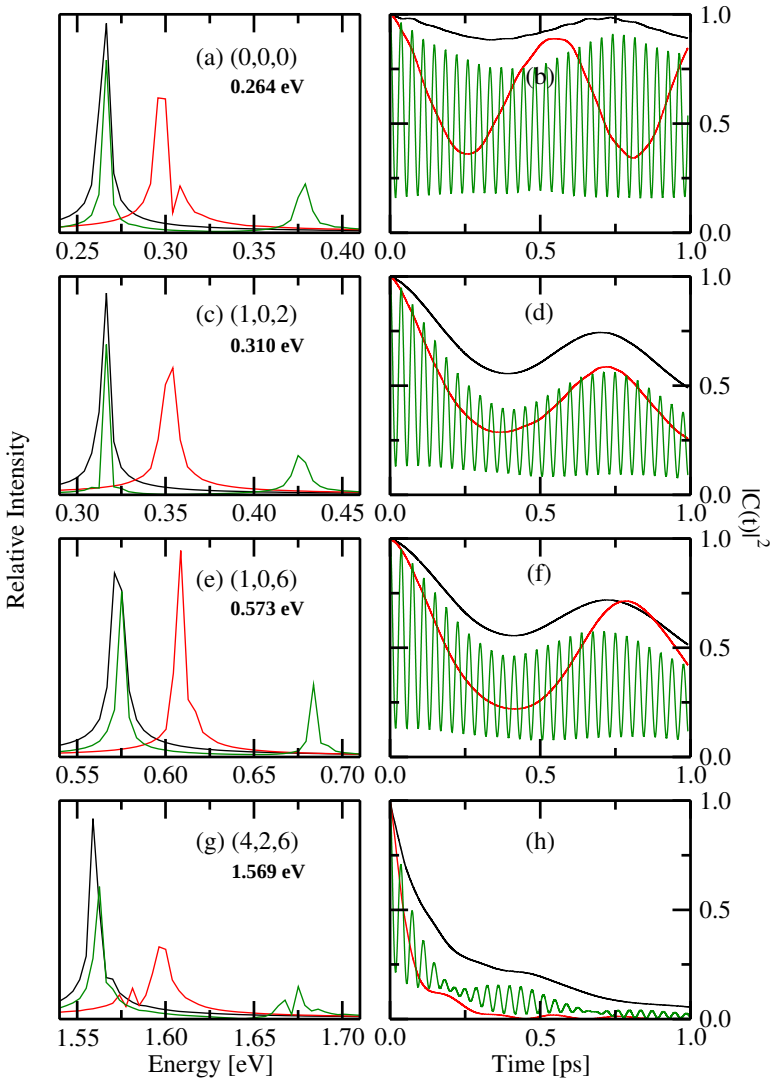

Figure 4.15: Impact of the electronic and electronic plus SO coupling on the quasibound spectrum of the individual eigenstates (indicated in the panel) of the $^2\Sigma_{1/2}$ adiabatic electronic state. The spectra obtained in the uncoupled (black solid line) and coupled [electronic only (red line) and electronic plus SO (green line)] state situations are shown in the panels in the left column of the figure. The time-dependence of the corresponding survival probabilities are plotted in the adjacent panels in the right column of the figure.

obtained in the uncoupled state situation and those obtained with the electronic and electronic plus SO coupling in the coupled state situation are shown by the dashed and dotted lines, respectively. The eigenvalue spectra in Fig. 4.15(a) correspond to the resonance shown in Fig. 4.12(a). It can be seen that the peak maxima (referring to the energy eigenvalue of the resonance) shifts to higher energy by $\sim$ 0.032 eV when electronic coupling is considered in the dynamics. This kind of shift of energy eigenvalue in the coupled state dynamical study has been reported earlier in the literature and is attributed to be arising due to the geometric phase change of the adiabatic electronic wavefunction while encircling the conical intersection in a closed loop [153, 154]. The spectral peak splits into two (green line) when both the electronic and SO coupling included in the dynamics. The two peaks are separated by $\sim$ 0.112 eV in energy which is nearly equal to the magnitude of the SO splitting of the interacting states (cf. Fig. 1).

The survival probability plot of the mentioned resonance shown in panel (b) reveals interesting dynamical features. The initial decay of the resonance is very very slow (cf. the solid black line) in the uncoupled state situation which indicates a long life-time of this quasibound state and therefore revealing a bound state character of this state. The inclusion of the electronic coupling leads to a relatively faster decay (cf. red line) of the same due to a nonadiabatic transition to the $^2\Pi$ electronic state. A nonradiative transition time of $\sim$ 250 fs can be discerned from the plot. In addition to the electronic coupling, when the SO coupling included in the dynamics, nonadiabatic transitions to the component ($^2\Pi_{3/2}$ and $^2\Pi_{1/2}$) states are possible and as a result one finds a rapid oscillatory pattern in the corresponding survival probability curve (cf. green line). The recurrences are $\sim$ 36 fs spaced in time. The latter corresponds to the $\sim$ 0.112 eV spacing of the

observed peaks in Fig. 4.15(a) (cf. green line).

Analogous features of the eigenvalue spectra and the survival probabilities are obtained for the (1,0,2) and (1,0,6) resonances shown in Figs. 4.15(c-d) and 4.15(e-f), respectively. Generally, the bending excitation leads to somewhat slower decay of the resonances which becomes more rapid when ClH_2 is excited along the R coordinate. The results shown in Fig. 4.15(g-h) correspond to the (4,2,6) eigenstate shown in Fig. 4.13(h). In this case, the state reveals much faster decay. The initial fast decay of survival probability relates to a decay time of $\sim$ 230 fs in the uncoupled state situation. This decay time is further reduced in the coupled state situation. Decay time of $\sim$ 70 fs can be estimated from the survival probability curves with electronic and electronic plus SO coupling. An energy shift of $\sim$ 0.035 eV in the eigenvalue of the resonances estimated with electronic coupling remains almost the same in all the spectra shown in Fig. 4.15. Also, the splitting in energy of $\sim$ 0.110 eV of the doublet peak structure when both the electronic and electronic plus SO coupling are considered nearly remains the same.

To this end it is worthwhile to discuss briefly the electronic population dynamics in the coupled state situations mentioned above. It is probably not relevant to discuss this for each of the quasibound states shown above and we typically select the quasibound state of Fig. 4.13(g) in the following discussion. In Figs. 4.16(a-b) we show the time-dependence of the adiabatic and diabatic electronic populations. While the populations shown in Fig. 4.16(a) consider the electronic coupling alone, both the electronic and SO couplings are considered in Fig. 4.16(b). Since, in the latter case the whole investigation is carried out in a diabatic electronic representation, we show the diabatic electronic populations only.

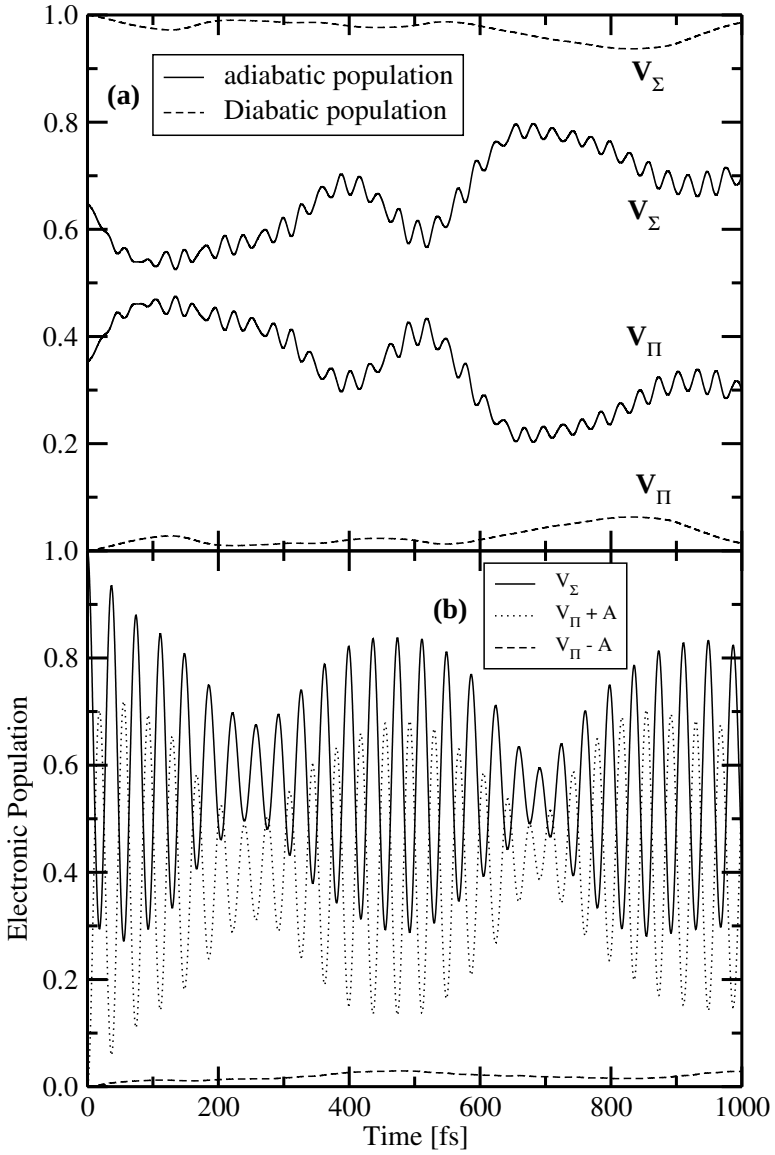

Figure 4.16: Time-dependence of the electronic population in the coupled state dynamics of the eigenstate of Fig. 4.15(g). The adiabatic (solid line) and diabatic (dashed line) electronic populations in panel (a) are obtained with the Σ-Π electronic coupling only. The diabatic electronic populations of the three SO states when both the electronic and SO coupling are included in the dynamical simulation are shown in panel (b).

In Fig. 4.16(a) the adiabatic and the diabatic electronic populations are indicated by the solid and dashed lines, respectively. The initial WP [the (4,2,6) eigenstate] is located on the $^2\Sigma$ diabat and therefore the population of this state is 1.0 (upper dashed curve) and that of the $^2\Pi$ state (lower dashed curve) is 0.0 at t=0. The population of the $^2\Sigma$ diabat decreases slightly and that of the $^2\Pi$ diabat grows to the same extent in time. It is evident from the figure that even for this high energy quasibound state, only a small fraction of the WP transits to the $^2\Pi$ surface. Since, this transition is solely caused by the Σ-Π electronic coupling, the latter seems to be very weak and does not have much impact on the dynamics. This is also revealed in the energy spectrum discussed in Fig. 4.14(a). The initial location of the WP for the population curves in Fig. 4.16(a) corresponds to an admixture of the $^2\Sigma$-$^2\Pi$ adiabatic states. Therefore, a 65% (35%) population of the $^2\Sigma$ ($^2\Pi$) adiabatic states is obtained at $t = 0$. Afterwords, the population exchange between the two surfaces through the Σ-Π conical intersection is clearly revealed by the figure.

The time-dependence of electronic populations of the $^2\Sigma_{1/2}$ and the two components of the $^2\Pi$ diabatic states in presence of the electronic and SO coupling are shown in Fig. 4.16(b). The electronic population of the $^2\Sigma_{1/2}$ diabatic state is shown by the solid line whereas that of the components of the $^2\Pi$ diabatic states are shown by dotted and dashed lines, respectively. In this case since the SO coupling is also activated in addition to the Σ-Π electronic coupling, a considerable population exchange with the component $^2\Pi$ states is also seen. Since the WP is initially located on the $^2\Sigma_{1/2}$ diabat, the population of this state is 1.0 at $t = 0$. It can be seen that the populations of the $^2\Sigma_{1/2}$ and one of the component (with energy $V_{\Pi+A}$) of the $^2\Pi$ diabat fluctuates uniformly in time, indicating the exchange of populations between these states mediated mostly by

the SO interactions. The recurrences in the population curves are $\sim$ 36 fs spaced in time which amounts to an energy spacing of $\sim$ 0.112 eV, nearly corresponding to the SO coupling strength of atomic Cl. The growth in population of the second component (with energy $V_{\Pi-A}$) of the $^2\Pi$ diabat in time is very small, indicating that the nuclear dynamics on the $^2\Sigma_{1/2}$ diabatic state is not very much affected by this state.

4.4 Summary

We have carried out detailed theoretical calculations of the photodetachment spectrum of ClH_2^- and ClD_2^-. A time-dependent WP approach is undertaken for this pourpose. The *ab initio* PESs of the electronic ground state of ClH_2^- reported by Alexander [148] and the ground and excited SO states of ClH_2 reported by Werner and Coworkers [75] are used in our dynamical calculations. The final theoretical results reported here are in good accord with the experiment [64].

The spectra corresponding to the transition to the uncoupled adiabatic SO states reveled progression of bands spaced in energy caused by the Σ-Π and Π-Π SO coupling. The resolved structure of each band presumably arising from the van der Waals progression and transition to the Cl + H_2 continuum states. The coupled state spectrum revels very complex features, in which each band appears due to a transition to all three SO states as well as the continuum states of Cl + H_2. The spacing between the two major peaks in the final theoretical results is found to be $\sim$ 0.102 eV which compares well with the experimental value of $\sim$ 0.111 eV. The overall shape of the final theoretical results and the widths of the two major peaks are in good accord with the experiment. The peak structure in the ClD_2^- detachment spectrum is more diffuse and broad compared to the

ClH_2^- spectrum, also in good accord with the experiment. We mention that the effect of the $^2\Sigma_{1/2}$ - $^2\Pi_{3/2}$ SO coupling is much stronger than the $^2\Pi_{3/2}$ - $^2\Pi_{1/2}$ SO coupling and the Σ-Π vibronic coupling has practically no impact on the spectrum. This is also in accord with the observations made in the reactive scattering calculations where it has been found that the SO excited state of Cl is less reactive than the SO ground state, but in apparent contradiction with the experiment [81, 140].

The existence of the van der Waals well in a reactive system has been demonstrated for the first time in the spectroscopic experiment of Neumark [64] and our quantum dynamical results presented here corroborate to such an observation. This in turn also reveals the spectroscopic accuracy of the reactive potential energy surfaces of Cl + H_2 [75]. A detailed analysis of the fine structures observed in various spectra is presented thereafter. Each envelope in the spectrum corresponds to an even quantum excitation along the bending coordinate. The fine structures under each envelope correspond to an extended progression along the Cl...H_2 dissociation coordinate. The excitation of the H_2 vibration is observed only at high energies. Majority of the quasibound states revealed features of a continuum state.

The effect of the electronic coupling to the $^2\Pi$ state has only minor impact on the overall structure of the quasibound spectrum of the $^2\Sigma$ state. However, the SO coupling has considerable effects on it. The line density in the spectrum increases significantly because of relatively strong nonadiabatic effects due to SO interactions and the spectrum becomes more diffuse and structureless. Investigation of the impact of the electronic and SO couplings on the individual eigenstates of the $^2\Sigma_{1/2}$ adiabat revealed that the electronic coupling alone causes a shift of the energy of the peak maxima by $\sim$ 0.035 eV. This is attributed to be due

to the geometric phase change of the adiabatic electronic wavefunction while encircling the $^2\Sigma$-$^2\Pi$ conical intersections in a closed loop. The electronic plus SO coupling splits each individual states of the uncoupled situation into two. The splitting in energy of ~ 0.112 eV of the resulting two peaks corresponds to the SO coupling of the atomic Cl plus the shift due to the electronic coupling as noted above. Examination of the time-dependent dynamics revealed a faster decay of the eigenstates in the coupled state situation.

Chapter 5

Dissociation dynamics of Cl···HD complex initiated by the photodetachment of Cl^-–HD

5.1 Introduction

Molecular dissociation following photodetachment of its anionic precursor represents a rarely explored class of chemical reactions, particularly, when the latter are guided by nonadiabatic interactions. As discussed in Chapter 4 anion photoelectron spectroscopy [155–157] by and large has been utilized to probe the bound vibronic level structure of the corresponding neutral species, however, the dissociation of the latter can become an important event when its equilibrium geometry differs significantly from that of the anion precursor. More specifically, if the 'transition state' or the repulsive region of the potential energy surface of the neutral species is probed by photodetachment [155]. Experimental measurement of such a process is also tedious and it requires a careful combination of the pho-

toelectron spectroscopy with the photofragment translational spectroscopy. Such a combination allows to record the kinetic energies and recoil angles of the photoelectron and the final photofragments are measured in coincidence [157]. This technique has been applied to study the dissociative photodetachment dynamics of weekly bound cluster anions [158] and van der Waals complexes [159].

The dissociation of Cl···HD followed by photodetachment of Cl^-–HD is examined in this chapter. The low-lying PESs of neutral Cl···HD are coupled by electronic and relativistic SO coupling [75, 90]. The topography and essential characteristics of $Cl(^2P) + H_2$ PESs are discussed in Chapter 1. The same PESs were used for Cl···HD system by replacing one of the H mass by D mass. The lower state of A' symmetry ($^2\Sigma_{1/2}$) correlates with the electronic ground state of the products HCl / DCl ($X^1\Sigma^+$) + H (^2S), whereas, the other two excited states (the components of the $^2\Pi$ state) correlate with the products in their electronic excited state, HCl / DCl ($^3\Pi$) + H(^2S) (e.g. see Fig. 1.1). The product excited state is considerably high in energy, thus the $^2\Pi_{3/2}$ and $^2\Pi_{1/2}$ states remain nonreactive in the adiabatic Born-Oppenheimer picture for low and moderate collision energies. However, they can form products via nonadiabatic transitions to the $^2\Sigma_{1/2}$ state. The two states of $^2A'$ symmetry are electronically coupled with each other and form a conical intersection [90]. Thus, two types of nonadiabatic coupling, (i) Σ-Π electronic coupling and (ii) Σ-Π and Π-Π relativistic SO coupling, govern the nuclear dynamics following photodetachment.

In the theoretical simulations the eigenfunctions of the energy levels of the electronic ground state of Cl^-–HD are vertically promoted to the coupled manifold of Cl···HD electronic states. These are then propagated on this final electronic manifold by numerically solving the time-dependent Schrödinger (TDSE) equation. The anionic wavefunctions are calculated by spectral quantization al-

gorithm [104, 160]. The channel specific dissociation probabilities of Cl···HD are calculated by recording the dissociative flux of the wave packet (WP) in time. We find that the nuclear dynamics is significantly affected by the nonadiabatic interactions. For instance, when the initial wavefunction is prepared on the $^2\Sigma_{1/2}$ electronic state, more WP flux moves to the reactive channels HCl + D or DCl + H in the coupled states situation than in the uncoupled one. The reactivity of the $^2\Pi_{3/2}$ and $^2\Pi_{1/2}$ electronic states via nonadiabatic transition to the $^2\Sigma_{1/2}$ state mostly populates the Cl + HD nonreactive channel of the latter. The dissociation to the reactive channels of the $^2\Sigma_{1/2}$ state in these cases are far less compared to the situation when dynamics is initiated on the $^2\Sigma_{1/2}$ electronic state. The formation of HCl + D is found to be more than DCl + H also for the excited eigen energy levels of Cl^-–HD .

5.2 Methodology and Computational Details

The Cl^-–HD anion is promoted to the reactive PES of neutral Cl···HD upon photodetachment. A Franck-Condon (FC) transition is assumed for this step and the subsequent reactive dynamics of Cl···HD is simulated by means of quantum WP propagation. The final products (in their electronic ground state) may emerge in one of the following three channels *viz.*, (a) HCl + D (R1), (b) DCl + H (R2) and (c) Cl + HD (NR). Here R1 and R2 represents the two reactive channels and 'NR' stands for the non-reactive channel. The channel specific dissociation probabilities are calculated both for the uncoupled and coupled surface situations for the $^2\Sigma_{1/2}$ electronic state. Since, the $^2\Pi_{3/2}$ and $^2\Pi_{1/2}$ electronic states yield products in their electronic ground state via nonadiabatic transitions to the $^2\Sigma_{1/2}$ state, the dynamics of these states are simulated in the coupled surface

situation only. All dynamical calculations are carried out for the lowest value of the total angular momentum; $J = 0$ and 0.5 in the nonrelativistic and relativistic situations, respectively, and the effect of excited vibronic levels of Cl^-–HD on the nuclear dynamics is examined.

The WP propagation in the coupled electronic manifold is carried out in a diabatic electronic representation [26]. However, an adiabatic electronic representation is more realistic and therefore, the adiabatic initial WP pertinent to the Cl^-–HD anion transformed to a diabatic electronic basis prior to its propagation on the Cl···HD electronic states and the time-evolved WP at each time is transformed back to the adiabatic electronic basis again to calculate the dynamical quantities. The nuclear dynamics is simulated here on the three lowest electronic states of Cl···HD including both the electronic and SO couplings among them. The Hamiltonian for the Cl···HD system can be expressed in the same way is discussed in Chapter 2 (c.f. Eq. A.1,2.16 2.17 and 2.27). The calculations are done for the lowest value of J and the Coriolis coupling terms are neglected.

5.2.1 Preparation of initial Wavefunction

The initial wavefunctions corresponding to the anionic precursor are obtained by calculating the eigenenergy levels of its electronic ground state. The ab initio PES reported by Alexander [148] is employed for the latter. The spectral quantization algorithm [160] is utilized to calculate the eigenvalues and eigenfunctions of the bound energy levels supported by this PES. The pseudo-spectrum obtained by initially locating a GWP near the equilibrium geometry of Cl^-–HD is shown in Fig. 5.1. The peaks in Fig. 5.1 correspond to the bound states supported in the potential well ($\sim$ 0.12 eV deep) of Cl^-–HD anion. The energy corresponding to the maximum of each peak in the spectrum is obtained by fitting the latter to

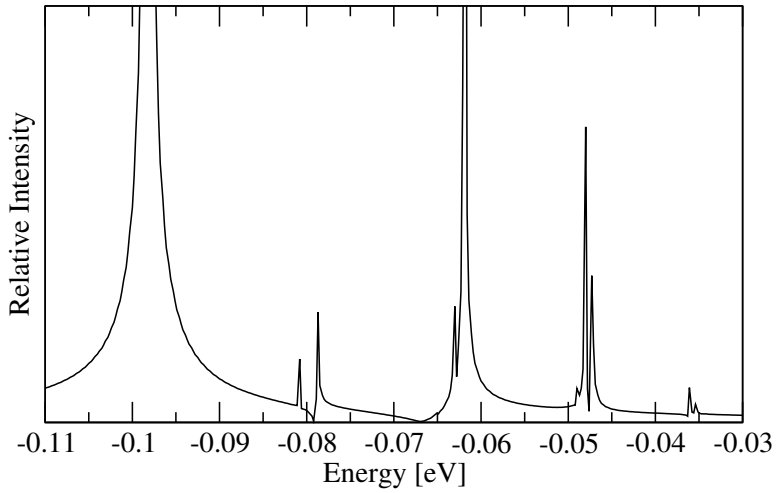

Figure 5.1: The bound energy level spectrum of the electronic ground state of the Cl^-–HD anion obtained by spectral quantization method and locating a stationary GWP near the equlibrium geometry of Cl^-–HD (at $R \sim 6.01\ a_0$, $r \sim 1.402\ a_0$ and $\gamma \sim 0^o$ with width parameters 0.25, 0.25 and 0.2 a_0 along these coordinates, respectively). The intensity in arbitary units is plotted as a function of the energy measured relative to that of equilibrium geometry of the electronic ground state of Cl^-–HD .

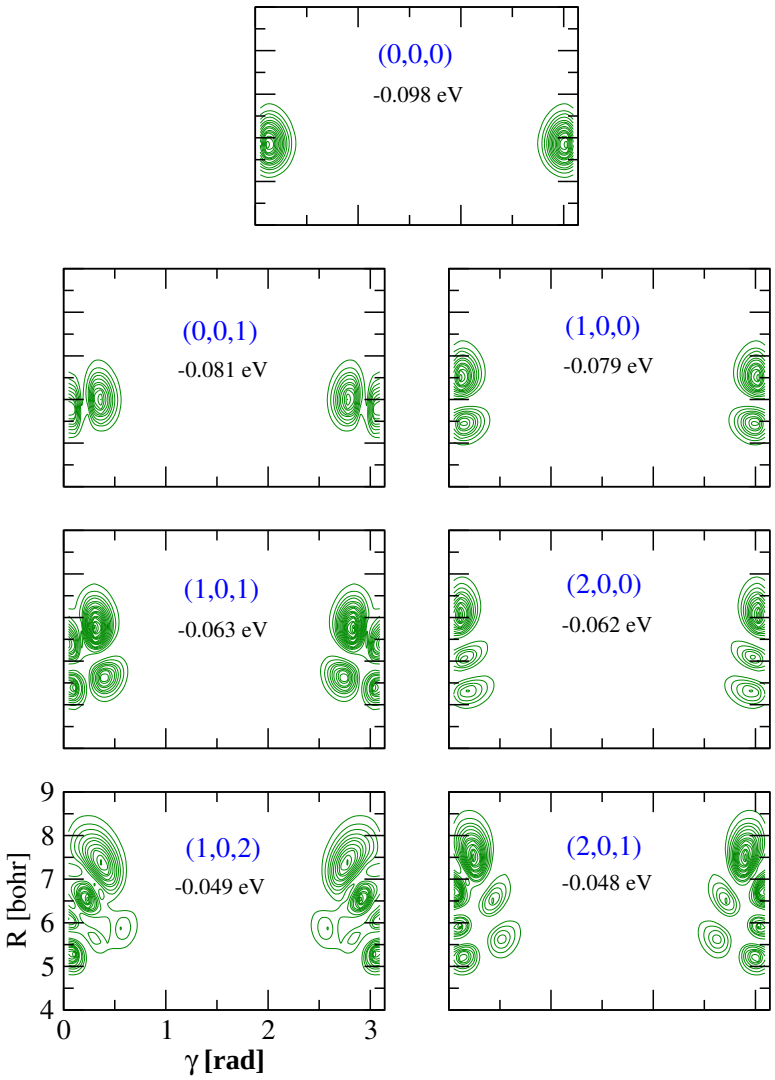

Figure 5.2: The probability density contours of the eigenfunctions of the energy levels of the electronic ground state of the Cl^-–HD anion. These are calculated by the spectral quantization algorithm and plotted in the (γ, R) plane. The eigenfunctions are averaged over r. The energy eigenvalue and the assignment in terms of number of nodes along R, r and γ are given for each eigenstate in the respective panel.

a Lorentzian line-shape function. The eigenfunctions are calculated by equation [4.6] and are averaged over r coordinate and plotted in Figs. 5.2(a-g) in terms of their probability density ($|\Psi|^2$) contours in the (γ, R) plane. These are assigned in terms of the number of nodes along R, r and γ coordinates and these are also indicated in the respective panel. In the Cl^-–HD PES two minima occurring for the linear $Cl^-\cdots$HD and $Cl^-\cdots$DH configurations, respectively, are separated by a barrier of $\sim$ 800 cm^{-1} at the T-shaped geometry [161]. Therefore, both the regions of the PES near $\gamma = 0$ and Π are populated due to quantum mechanical tunneling and can be seen from the wavefunction plots in Figs. 5.2(a-g).

The adiabatic initial wavefunctions of the anion presented above are subjected to FC transition to the adiabatic electronic states of the neutral species. They are then transformed to a diabatic electronic basis by, $\Psi^d = S\Psi^{ad}$, where S is the adiabatic-to-diabatic transformation matrix. The latter represents the eigenvector matrix which diagonalizes $\mathcal{H}^{el} + \mathcal{H}^{so}$. This matrix is numerically diagonalized at each node of the grid constructed here for the propagation of the WP and the transformation of the wavefunction between the adiabatic and diabatic electronic representations is carried out accordingly.

5.2.2 Wave packet propagation and dissociation probability

The initial WP discussed above is propagated in the coupled manifold of the final diabatic electronic states with the aid of the TDSE. The TDSE is numerically solved on a grid consisting of equally spaced points along the Jacobi distances R (128 points in the range 1.0 a_0 to 14.0 a_0) and r (64 points in the range 0.1 a_0 to 8.0 a_0). The grid along γ is chosen as the nodes of a 49-points Gauss-Legendre quadrature [141]. The calculations are carried out for the lowest value of the

total angular momentum ($J = 0.5$ with and $J = 0$ without the SO coupling). The Coriolis coupling terms of the Hamiltonian are not included in the present calculations.

The exponential time evolution operator in the TDSE (see above) at each time step is evaluated by the second-order split-operator method [130]. The fast Fourier transform method [102] and the discrete variable representation method [132] are used to evaluate the action of the radial and angular kinetic energy operators on the wave functions, respectively. In order to avoid the unphysical reflections of the fast moving components of the WP at the grid boundaries a sine-type of damping potential [135] is activated at the last 32 grid points along R and the last 15 grid points along r. The WP is propagated in time with a step size of $\Delta t \sim 0.13$ fs for a total propagation time of ~ 550 fs. The convergence of the results is explicitly checked by varying all the grid parameters noted above.

In order to access the energy distribution, we calculate the time autocorrelation function of the wave packet, $\langle \Psi(0) | \Psi(t) \rangle$, evolving on the neutral electronic states upon photodetachment. A Fourier transform of this autocorrelation function yields the photodetachment spectrum (cross sections), revealing the range of energy covered by the initial wave packet. For illustration, a photodetachment spectrum obtained with (0,0,0) anionic wavefunction evolving on the $^2\Sigma_{1/2}$ adiabatic electronic state of ClHD is shown in Fig. 5.3.

The time-evolved WP at each time t is transformed back to the adiabatic electronic representation by using the hermitian conjugate of the S matrix and its asymptotic components on the $^2\Sigma_{1/2}$ electronic state are analyzed to calculate the dissociation probabilities. Only the components on the $^2\Sigma_{1/2}$ electronic state are of interest here because, as stated above, the components on the $^2\Pi_{3/2}$ and $^2\Pi_{1/2}$ electronic states do not yield products in their electronic ground state.

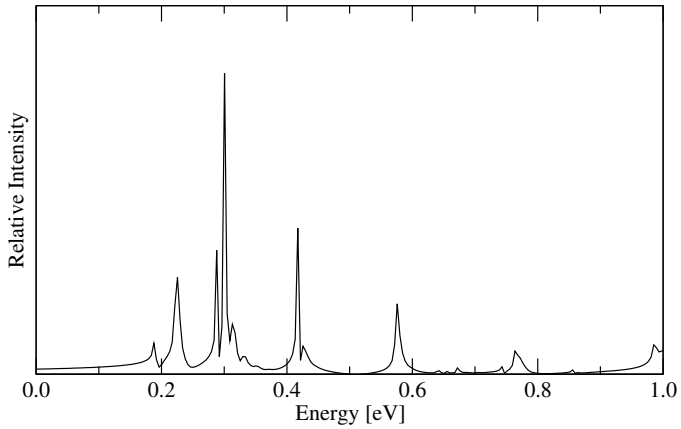

Figure 5.3: The photodetachment spectrum of $ClHD^-$ for a transition of the initial (0,0,0) to the uncoupled $^2\Sigma_{1/2}$ adiabatic SO states of $Cl(^2P)$ + HD. The intensity in arbitrary units is plotted as a function of the energy of the final electronic state E. The zero of the energy scale corresponds to the asymptotically separated Cl + HD on the $^2\Sigma_{1/2}$ state.

However, we note that the NR components on the latter states are examined also in order to check the convergence of the dissociation probability results. The initial state-selected and time-resolved dissociation probabilities are obtained by integrating the WP flux at a dividing surface at, $r = r_d$ (located far out in the desired channel) as

$$P_i(t) = \langle \Phi(R, r, \gamma, t) | \hat{F} | \Phi(R, r, \gamma, t) \rangle |_{r=r_d} \tag{5.1}$$

where $P_i(t)$ is the dissociation probability starting form an initial state i of Cl^-–HD and averaged over all final states of the dissociative fragments of Cl···HD . The flux operator $\hat{F}$ in terms of a specific channel coordinate (say, r) is given by

$$\hat{F} = -\frac{i\hbar}{2\mu} \left[\frac{\partial}{\partial r} \delta(r - r_d) + \delta(r - r_d) \frac{\partial}{\partial r} \right]. \tag{5.2}$$

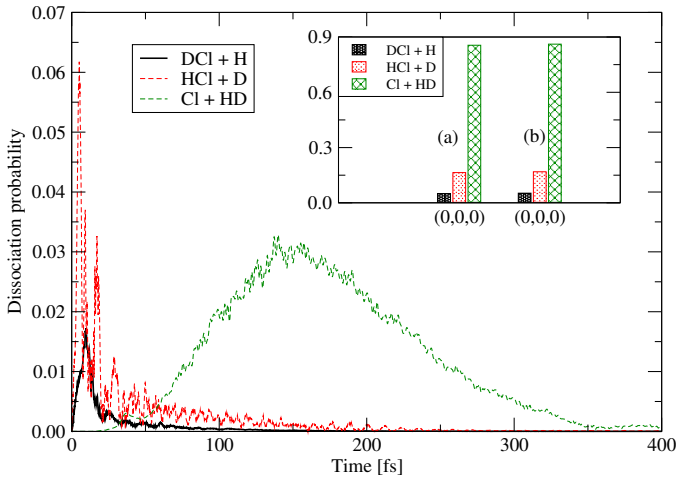

Figure 5.4: Time-dependent dissociation probabilities of Cl···HD to the DCl + H (solid line), HCl + D (dotted line) and Cl + HD (dashed line) channels of the $^2\Sigma_{1/2}$ electronic state. The Cl···HD species is prepared by photodetaching Cl^-–HD from the (0,0,0) level of its electronic ground state. This initial wavefunction is evolved on the uncoupled $^2\Sigma_{1/2}$ electronic state of the neutral to calculate the dissociation probabilities. The total dissociation probabilities (integrated over time) of the three channels obtained by using the initial wavefunction calculated by (a) a relaxation scheme and (b) the spectral quantization method are shown in the inset.

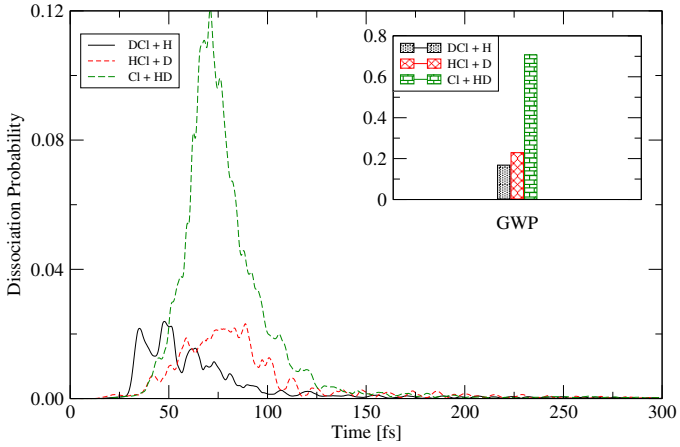

Figure 5.5: Same as Fig. 5.4 with a initial GWP

With this, the dissociation probability in Eq. [5.1] assumes the form

$$P_i(t) = \frac{\hbar}{\mu}\mathrm{Im}\left[\langle\Phi(R, r_d, \gamma, t)|\frac{\partial\Phi(R, r_d, \gamma, t)}{\partial r}\rangle\right]_{r=r_d}. \tag{5.3}$$

The quantity in the right-hand side is integrated over the whole range of R and γ to obtain the dissociation probability at each time t which is further integrated over t to calculate the total dissociation probability. Here we note that the distinction between the two reactive channels (R1 and R2) in the product asymptote is made by comparing the internuclear distances of the product HCl and DCl molecules. The reactive flux, [Eq. (5.2)], in which the HCl distance is smaller than the DCl distance is considered to represent the (R1) channel and the rest is considered to represent the (R2) channel.

5.3 Results and Discussion

In order to clearly revel the effects of nonadiabatic coupling on the Cl···HD dissociation dynamics, we first consider the FC transition of the (0,0,0) wavefunction of Cl^-–HD (cf., Fig. 5.2(a)) to the uncoupled $^2\Sigma_{1/2}$ electronic state of the neutral Cl···HD . The equilibrium geometry of the Cl^-–HD anion is significantly stretched along R ($\sim 6\ a_0$). Therefore, the FC transition promotes this anionic wavefunction to the van der Waals well region of the reagent asymptote of the reactive Cl···HD PES. The resulting time-dependent dissociation probabilities for the R1, R2 and NR channels are plotted in Fig. 5.4 and are indicated by different line types in the panel. The total dissociation probabilities (integrated over time) are shown as a bar diagram in the inset. In the latter, the results from the initial wavefunctions calculated by the spectral quantization scheme (as discussed above) and also by a relaxation scheme [149] using the Lanczos propagator

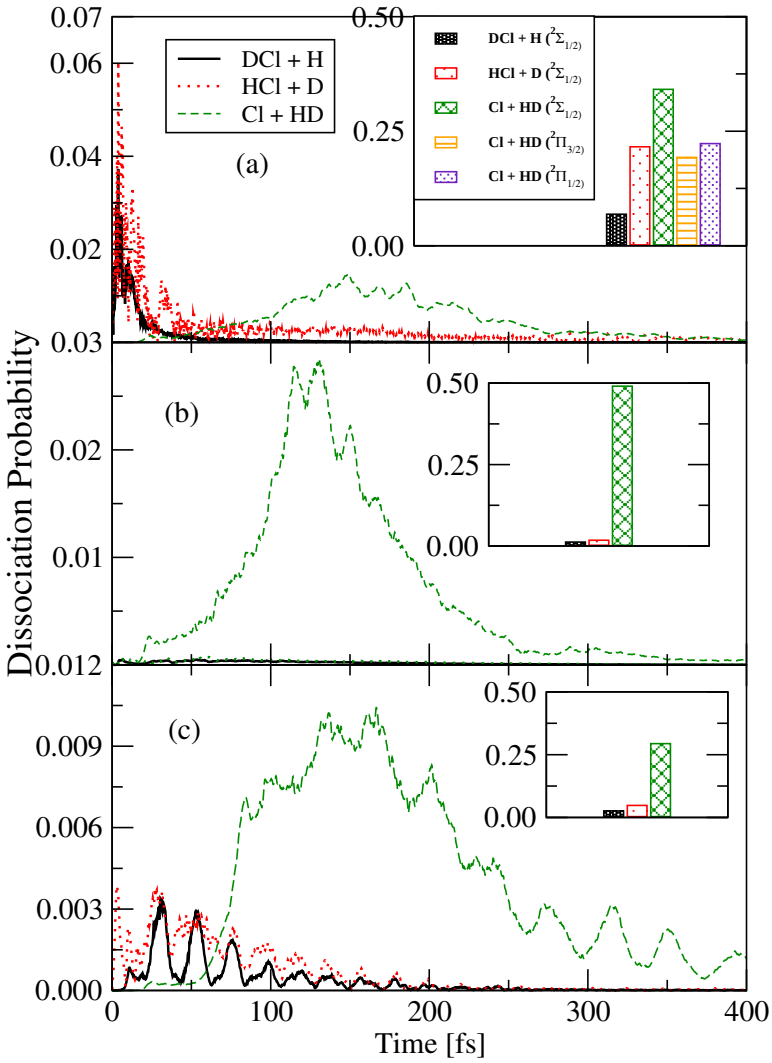

Figure 5.6: Same as in Fig. 5.4, obtained for the transition of the (0,0,0) wavefunction of the Cl^-–HD anion to the (a) $^2\Sigma_{1/2}$, (b) $^2\Pi_{3/2}$ and (c) $^2\Pi_{1/2}$ adiabatic electronic state of Cl···HD . The nuclear dynamics in each case is simulated in the coupled (both electronic and SO) manifold of electronic states of the latter. The total dissociation probabilities to the non-reactive channels of the excited $^2\Pi_{3/2}$ and $^2\Pi_{1/2}$ states are also included in the inset of panel (a)

are shown (indicated by a and b, respectively, in the inset). The identity of the two results revel the accuracy of the initial wavefunctions calculated here by the spectral quantization method. It can be seen from Fig. 5.4 that dissociation to the Cl + HD (NR) channel is dominated followed by the HCl + D (R1) channel on the uncoupled $^2\Sigma_{1/2}$ electronic state. Also the R1 channel dominates over the DCl + H (R2) channel in the dynamics.

5.3.1 The effect of electronic and SO coupling

The nuclear dynamics followed by the initial FC transition of the above (0,0,0) anionic wavefunction separately to the $^2\Sigma_{1/2}$, $^2\Pi_{3/2}$ and $^2\Pi_{1/2}$ adiabatic electronic states of the neutral Cl···HD in the coupled states situation is considered next. Both the electronic and relativistic SO coupling are activated in the dynamical simulations. The results are presented in Figs. 5.6(a-c), respectively. The adiabatic initial anionic wavefunction is transformed to diabatic electronic basis and propagated in the coupled manifold of the electronic states (cf., Hamiltonian in Eq. A.1) of neutral Cl···HD . In Fig. 5.6(a), the anionic wavefunction is initially promoted to the $^2\Sigma_{1/2}$ electronic state of the neutral. It can be seen form Fig. 5.6(a) that the reactive R1 channel still dominates over the R2 channel of the $^2\Sigma_{1/2}$ adiabatic electronic state and the dissociation to its NR channel is significantly less than what was observed in the uncoupled surface situation (cf., Fig. 5.4). It can be seen also that dissociation to both the reactive channel also increases in the coupled surface situation. Therefore, the nonadiabatic coupling enhances the reactive dissociation and reduces the nonreactive dissociation of Cl···HD . We note here that the sum of total dissociation probabilities on the $^2\Sigma_{1/2}$ state shown in the inset of Fig. 5.6(a) is less than 1.0 and is only $\sim$ 0.69. The remaining of the WP dissociates in the NR channel of the $^2\Pi_{3/2}$ and

$^2\Pi_{1/2}$ electronic states and are also indicated in the inset.

The reactivity of the $^2\Pi_{3/2}$ electronic state via nonadiabatic transitions to the $^2\Sigma_{1/2}$ electronic state is shown in Fig. 5.6(b). The (0,0,0) anionic wavefunction in this case is promoted to the $^2\Pi_{3/2}$ adiabatic electronic state of the neutral initially, and evolved in the coupled diabatic electronic manifold of the latter. In this case, as can be seen from the inset, the dissociation to the NR channel of the $^2\Sigma_{1/2}$ electronic state dominates. The dissociation to the reactive R1 channel and R2 channels is practically insignificant. The remaining of the WP dissociates to the NR channel of $^2\Pi_{3/2}$ and $^2\Pi_{1/2}$ electronic states. Therefore, it can be concluded that the nonadiabatic transition of the WP (prepared initially on the $^2\Pi_{3/2}$ state) to the $^2\Sigma_{1/2}$ state leads to the dissociation predominately via the NR channel of the latter. The same scenario as in the case of Fig. 5.6(b) persists for an initial transition of the (0,0,0) anionic wavefunction to the $^2\Pi_{1/2}$ electronic state of Cl···HD and is depicted in Fig. 5.6(c). However, in this case the dissociation probabilities to the reactive R1 and R2 channels of the $^2\Sigma_{1/2}$ state are somewhat larger than those observed in Fig. 5.6(b). Here also the remaining of the WP dissociates to the NR channels of the $^2\Pi_{3/2}$ and $^2\Pi_{1/2}$ electronic states. The results presented in Figs. 5.6(a-c) reveal that the products are formed in their electronic ground state with better yield when the dynamics is initiated on the $^2\Sigma_{1/2}$ electronic state of Cl···HD .

In order to better understand the above quantum dynamical results, we show in Figs. 5.7(a-c) the time-dependence of the adiabatic electronic populations in the coupled state dynamics of Cl···HD . The results of the initial FC transition of Cl^-–HD to the adiabatic $^2\Sigma_{1/2}$, $^2\Pi_{3/2}$ and $^2\Pi_{1/2}$ electronic states of Cl···HD are shown in the panel *a*, *b* and *c*, respectively. These adiabatic initial wavefunctions are evolved in the coupled manifold of the diabatic electronic states of Cl···HD and

adiabatic electronic populations are calculated at each time t. In each panel the electronic populations of the three states are indicated by different line types. These represent fractional populations. Since the initial wavefunction in Fig. 5.7(a) is initially located on the $^2\Sigma_{1/2}$ adiabatic electronic state its population is 1.0 at $t = 0$. The populations of the $^2\Pi_{3/2}$ and $^2\Pi_{1/2}$ are therefore zero initially. At later times the WP on the $^2\Sigma_{1/2}$ electronic state reaches the Σ-Π curve crossing regions and population transfer to the $^2\Pi_{3/2}$ and $^2\Pi_{1/2}$ adiabatic electronic states takes place. This is indicated by a decrease in the $^2\Sigma_{1/2}$ and a growth in the $^2\Pi_{3/2}$ and $^2\Pi_{1/2}$ electronic populations. The population of the $^2\Sigma_{1/2}$ electronic state sharply decreases to $\sim$ 58 % within $\sim$ 20 fs followed by quasiperiodic recurrences. It can be seen from Fig. 5.7(a) that somewhat more population transfer takes place to the $^2\Pi_{1/2}$ electronic state when compared to that to the $^2\Pi_{3/2}$ electronic state. For instance, $\sim$ 30 % of the WP moves to the $^2\Pi_{1/2}$ and only $\sim$ 12 % to the $^2\Pi_{3/2}$ electronic state at $\sim$ 20 fs. The oscillations in the population curves indicates the transfer of the WP back and forth through the curve crossings of different electronic states.

The population curves for an initial transition of the anion to the $^2\Pi_{3/2}$ state of the neutral are plotted in Fig. 5.7(b). In this case the decay of the $^2\Pi_{3/2}$ electronic population is not as large as that observed for the $^2\Sigma_{1/2}$ state in panel *a*. The population transfer to the $^2\Sigma_{1/2}$ state (solid line) is more than that to the $^2\Pi_{1/2}$ state (dashed line). However, it seems that the major fraction of the WP dissociates to the NR channel of the $^2\Pi_{3/2}$ electronic state leading to Cl + HD.

The scenario for an initial transition of the anion to the $^2\Pi_{1/2}$ electronic state of the neutral is depicted in Fig. 5.7(c). In contrast to the dynamics on the $^2\Pi_{3/2}$ electronic state, the nuclear motion on the $^2\Pi_{1/2}$ electronic state is much perturbed by the nonadiabatic interactions. As a result, relatively more

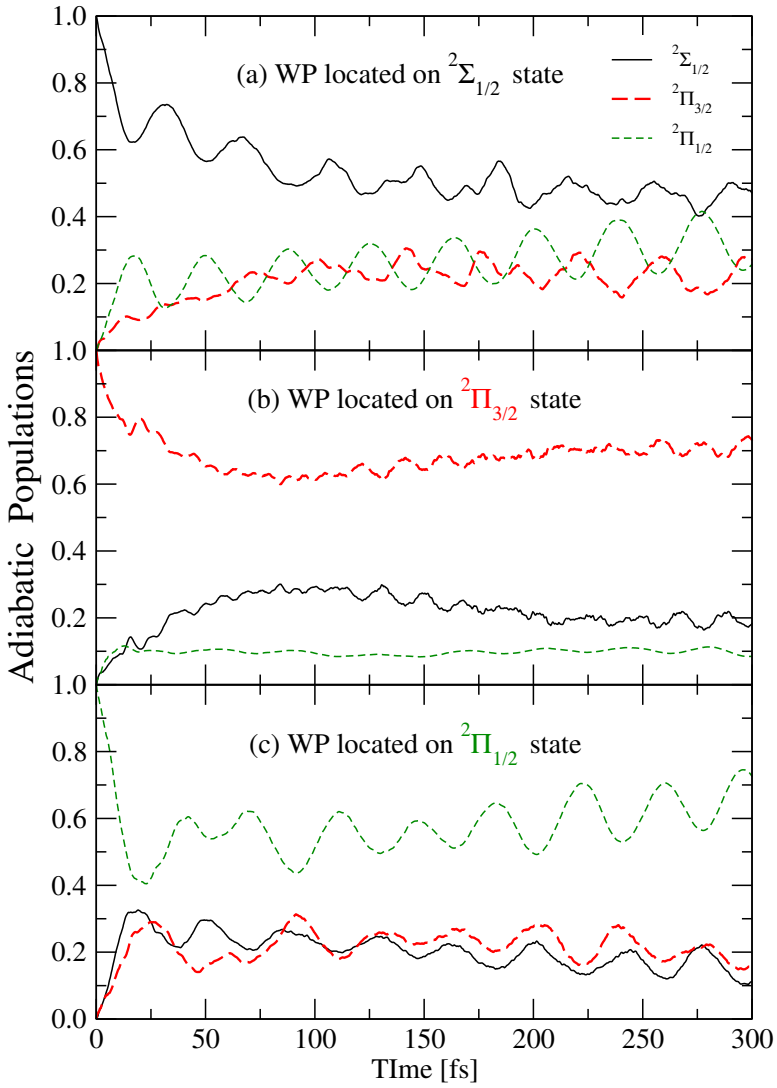

Figure 5.7: Time dependence of the adiabatic electronic populations in the coupled state dynamics of Fig. 5.6. The initial WP in panel *a*, *b* and *c* corresponds to that of panel *a*, *b* and *c*, respectively, of Fig. 5.6. The populations of the $^2\Sigma_{1/2}$, $^2\Pi_{3/2}$ and $^2\Pi_{1/2}$ adiabatic electronic states in each panel are shown by the solid, dotted and dashed lines.

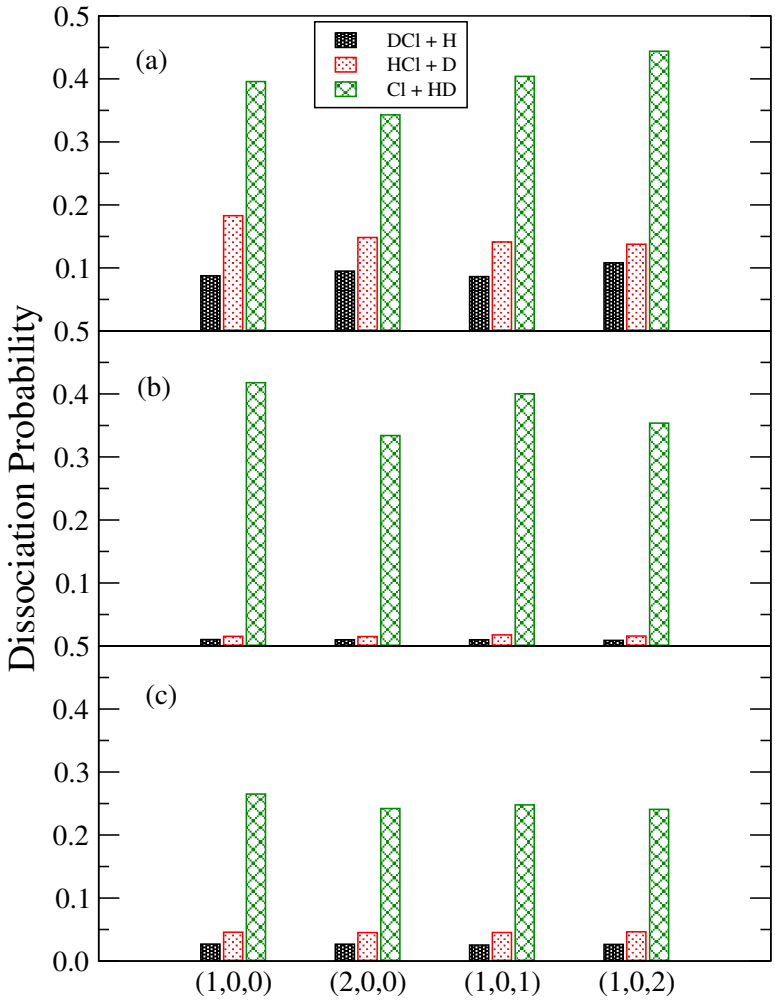

Figure 5.8: The time-integrated total dissociation probabilities of internally excited eigenlevels of Cl^-–HD to the HCl + D, DCl + H and Cl + HD channels of the $^2\Sigma_{1/2}$ electronic state of Cl···HD . The results obtained from the initial FC transition of the anion to the $^2\Sigma_{1/2}$, $^2\Pi_{3/2}$ and $^2\Pi_{1/2}$ electronic state of the neutral are shown in panel *a*, *b* and *c*, respectively.

fraction of the WP (as compared to panel *b*) moves to the $^2\Sigma_{1/2}$ and $^2\Pi_{3/2}$ electronic states. This also accounts for a relatively increased reactive dissociation of Cl···HD on the $^2\Sigma_{1/2}$ electronic state (cf. Fig 5.6(b) vs. Fig 5.6(c)) for this initial condition.

In Figs. 5.8(a-c) we show the dissociative photodetachment dynamics of the excited vibrational levels of the ground electronic state of Cl^-–HD . We plot the time-accumulated dissociation probabilities for these initial wavefunctions promoted to the $^2\Sigma_{1/2}$, $^2\Pi_{3/2}$ and $^2\Pi_{1/2}$ adiabatic electronic states of Cl···HD , respectively, in panel *a*, *b* and *c*. It can be seen that the dissociation to the DCl + H channel increases and to the HCl + D channel decreases upon internal excitation. However, no significant change in the dissociation probabilities can be observed for the initial transition to the $^2\Pi_{3/2}$ and $^2\Pi_{1/2}$ electronic states of Cl···HD . In all cases the NR channel dominates and HCl + D formation is preferred over DCl + H formation.

5.4 Summary

We presented a brief theoretical account of the dissociative photodetachment dynamics of Cl^-–HD anion in this chapter. Photodetachment of Cl^-–HD anion prepares the neutral Cl···HD species in the van der Waals well region of the reagent (Cl + HD) asymptote of its reactive PES. The latter represents a manifold of three electronic states coupled by the electronic and relativistic SO interactions. The dissociation of Cl···HD complex occurs on its lowest $^2\Sigma_{1/2}$ electronic states and the products emerge in their electronic ground state in three different R1, R2 and NR channels. The $^2\Pi_{3/2}$ and $^2\Pi_{1/2}$ electronic state of Cl···HD can form the dissociative fragments in their electronic ground state only by non Born-Oppenheimer transition to the $^2\Sigma_{1/2}$ state.

The eigenfunctions of the vibronic levels of Cl^-–HD anion are calculated and are vertically promoted to the coupled manifold of electronic states of Cl···HD . The dissociation of the latter subsequently monitored by a time-dependent WP propagation approach. The nonadiabatic coupling is observed to enhance the reactivity of the $^2\Sigma_{1/2}$ electronic state. Generally, for all initial transitions to the $^2\Sigma_{1/2}$, $^2\Pi_{3/2}$ or $^2\Pi_{1/2}$ electronic states of Cl···HD and for internally excited initial wavefunctions of the anion the reactive HCl + D channel dominates over the DCl + H channel. The dissociation to the NR channel is always more than the rest. The effect of the nonadiabatic coupling on the nuclear dynamics on the $^2\Pi_{1/2}$ electronic state appears to be significantly more that that on the $^2\Sigma_{1/2}$ and $^2\Pi_{3/2}$ electronic states of Cl···HD . Finally, we mention that the photodetachment recording on Cl^-–HD anion has been carried out and it will be worthwhile to extend these measurements with the aid of photofragment translational spectroscopy in order to validate the accuracy of the PESs and the theoretical findings of this present chapter.

Chapter 6

Future Directions

We have presented a theoretical account of the reactive scattering dynamics occurring on three electronic states of $Cl(^2P)$ + H_2 (HD) reaction. The effect of electronic and SO coupling are studied with the aid of time-dependent WP approach. Our findings reveal a decrease of reaction probability with the inclusion of coupling. The quantum dynamical simulations are carried out by a time-dependent WP approach within the CS approximations. Calculations of initial state-selected energy resolved reaction probabilities, integral reaction cross sections and thermal rate constants are carried out both in the uncoupled- and coupled-state situations. We report the detailed theoretical calculations of the photodetachment spectrum of ClH_2^- (ClD_2^-) along with a detailed theoretical account of the quasibound states corresponding to resonances in the $Cl(^2P)$ + H_2 reaction dynamics. Finally, We have presented a brief theoretical account of the dissociation dynamics of the Cl^-–HD anion. A brief theoretical description of the photoelectron spectrum of F_2O is also presented in the appendix.

In addition to the electronic and SO coupling, the Coriolis coupling terms in the Hamiltonian may also have an important role in the dynamics. The latter

has been found to be crucial for some reactions occurring on a single electronic state [189]. Such a coupling is shown to have relatively minor role in the F + H_2 reaction dynamics. An estimate of the effect of the Coriolis terms for Cl(^2P) + H_2 and Cl(^2P) + HD reaction would be valuable in order to assess the interplay of three different coupling mechanisms on their reaction dynamics. Such a study is presently under progress.

As discussed in cheaper 2 and 3, in a reactive scattering study, ideally the reaction should be initiated in an adiabatic electronic representation. However, in the present study, only a diabatic electronic representation is utilized in the coupled three-state model when electronic and SO coupling is included in the dynamics. A detailed study of the Cl(^2P) + H_2 (HD) reaction dynamics starting from the reaction in the adiabatic electronic representation will be important to validate this concept and may help us to understand the differences between the observed experimental results.

According to the molecular beam experimental results by Liu and coworkers [62, 63], the SO excited Cl*($^2P_{1/2}$) state seems to be more reactive than the SO ground state Cl*($^2P_{1/2}$), which is an apparent contradiction to the theoretical wisdom and still remains unresolved. It will be worthwhile to study the state-to-state reaction dynamics of this reaction including the electronic and SO coupling to put some light on this unusual experimental observation.

Bibliography

[1] M. Born and E. Oppenheimer, Ann. Phys. **84**, 457 (1927).

[2] M. Born and K. Huang, in *The Dynamical Theory of Cryatal Lattices* (Oxford University Press, 1954).

[3] *State-Selected and State-to-State Ion-Molecule Reaction Dynamics, Part 1 and 2* edited by M. Baer and C.-Y. Ng. (Willey and Sons: New York, 1991: Vol. 82).

[4] X. Hu and K. Schulten, Phys. Today, **50**, 28 (1997).

[5] J. Michl and V. Bonacic-Koutecky, in *Electronic aspects of organic photochemistry* (Willey: New York 1990).

[6] G. A. Worth and L. S. Cederbaum, Ann. Rev. Phys. Chem. **55**, 127 (2004).

[7] E. Teller, J. Chem. Phys. **41**, 109 (1937).

[8] G. Herzberg and H. C. Longuet-Higgins, Discuss. Faraday Soc. **35**, 77 (1963).

[9] T. Carrington, Discuss. Faraday Soc. **53**, 27 (1972); Acc. Chem. Res. **7**, 20 (1974).

[10] H. Köppel, W. Domcke and L. S. Cederbaum, Adv. Chem. Phys. **57**, 59 (1984).

[11] D. R. Yarkony, Rev. Mod. Phys. **68**, 985 (1996); Acc. Chem. Res. **31**, 511 (1998); J. Chem. Phys. **105**, 6277 (2001).

[12] W. Domcke, D. R. Yarkony, H. Köppel, Eds. *Conical Intersections: Electronic Structure, Dynamics and Spectroscopy*, (World Scientific, Singapore 2004).

[13] F. Bernardi, M. Olivucci and M. Robb, Isr. J. Chem. **33**, 265 (1993); Chem. Soc. Rev. **25**, 321 (1996).

[14] Chemical Physics **259**, 121-350, 2000 (special issue on conical intersections)

[15] *Spin Orbit coupling in Molecules* by W. G. Richards and H. P. Trivedi *et al.* . (Oxford: Clarendon Press, 1981).

[16] *Spin-orbit Coupling Effects in Two-dimensional Electron and Hole Systems* by R. Winkler (Springer-Verlag GmbH, 2003).

[17] H. Jahn and E. Teller, Proc. Roy. Soc. London, Ser. A. **161**, 220 (1937).

[18] I. B. Bersuker, *The Jahn-Teller Effect and Vibronic Interactions in Modern Chemistry* (Plenum Press, New York, 1984)

[19] R. Englman, *The Jahn-Teller Effect in Molecules and Crystals*, (Wiley, New York, 1972).

[20] I. B. Bersuker, Chem. Rev. **101**, 1067 (2001).

[21] M. Z. Zgierski and M. Pawlikowski, J. Chem. Phys. **70**, 3444 (1979).

[22] H. Köppel, L. S. Cederbaum, and W. Domcke, J. Chem. Phys. **89**, 2023 (1988).

[23] Köppel, L. S. Cederbaum and W. Domcke, J. Chem. Phys. **111**, 10452 (1988).

[24] E. Renner, Z. Phys. **92**, 172 (1934).

[25] Ch. Jungen and A. Merer, J. Mol. Phys. **40**, 1 (1980).

[26] W. Lichten, Phys. Rev. **164**, 131 (1967); F. T. Smith, *ibid.* **179**, 111 (1969); T. F. O'Malley, Adv. At. Mol. Phys. **7**, 223 (1971); T. Pacher, L. S. Cederbaum, and H. Köppel, Adv. Chem. Phys. **84**, 293 (1993).

[27] F. T. Smith, "Diabatic and Adiabatic Representations for Atomic Collision Problems", Phys. Rev. **179**, 111 (1969).

[28] T. Pacher, L. S. Cederbaum, H. Köppel, "Adiabatic and quasidiabatic states in a gauge theoretical framework", Adv. Chem. Phys. **84**, 293 (1993) and references therein.

[29] M. Bear, Chem. Phys. Lett. **35**, 112 (1975); Chem. Phys. **15**, 49 (1976); Adv. Chem. Phys. **82**, 73 (1992).

[30] T. Pacher, L. S. Cederbaum, H. Köppel, Adv. Chem. Phys., **84**, 293 (1993).

[31] A. Thiel, and H. Köppel, J. Chem. Phys., **110**, 9371 (1999).

[32] H. Köppel, J. Gronki, and S. Mahapatra, J. Chem. Phys., **115**, 23771 (2001).

[33] S. Mahapatra, H. Köppel and L. S. Cederbaum, J. Phys. Chem. A **105**, 2321 (2001).

[34] H. Köppel, "Conical Intersections: Electronic Structure, Dynamics and Spectroscopy", In DOMCKE et al. [12], p. 429 (2004).

[35] E. J. Heller, J. Chem. Phys. **68**, 2066, 3891 (1978); Acc. Chem. Res. **14**, 368 (1981).

[36] S. Mahapatra, N. Chakrabarti and N. Sathyamurthy, Int. Rev. Phys. Chem. **18**, 235 (1999).

[37] N. Balakrishnan, C. Kalyanaraman, and N. Sathyamurthy, Phys. Rep. **280**, 79 (1997); M. Beck, A. Jäckle, G. A. Worth, and H. -D. Meyer, Phys. Rep. **324**, 1 (2000); G. Nyman and H. -G. Yu, Rep. Prog. Phys. **63** , 1001 (2000).

[38] D. E. Manolopolous, J. Chem. Soc. Faraday Trans. **93**, 673 (1997).

[39] D. E. Manolopolous, K. Stark, H.-J. Werner, D. W. Arnold, S. E. Bradforth and D. M. Neumark, Science, **262**, 1852 (1993).

[40] J. F. Castillo, B. Hartke, H.-J. Werner, F. J. Aoiz, L. Ba nares and B. Martinez-Haya, J. Chem. Phys. **109**, 7224 (1993).

[41] J. F. Castillo, D. E. Manolopolous, K. Stark and H.-J. Werner, J. Chem. Phys. **104**, 6531 (1996).

[42] M. Baer, M. Faubel, B. Martinez-Haya, L. Y. Rusin, U, Tappe and J. P. Toennies, J. Chem. Phys. **104**, 2743 (1996).

[43] P. Honvault and J.-M. Launay. Chem. Phys. Lett. **287**, 270 (1998); **303**, 657 (1999).

[44] J. F. Castillo and D. E. Manolopolous, Faraday Discuss. Chem. Soc. **110**, 119 (1998).

[45] R. T. Skodje, D. Skouteris, D. E. Manolopolous, S.-H. Lee, F. Dong and K. Liu, J. Chem. Phys. **112**, 4536 (2000).

[46] F. J. Aoiz, L. Ba nares, B. Martinez-Haya, J. F. Castillo and D. E. Manolopolous, J. Phys. Chem. A **101**, 6403 (1997).

[47] M. H. Alexander, H. -J. Werner, and D. E. Manolopoulos, J. Chem. Phys. **109**, 5710 (1998); M. H. Alexander, D. E. Manolopoulos, and H. -J. Werner, J. Chem. Phys. **113**, 11084 (2000).

[48] K. Stark and H.-J. Werner, J. Chem. Phys. **104**, 6515 (1996).

[49] M. Faubel, L. Rusin, S. Schlemmer, F. Sonderman, U. Tappe and J. P. Toennies, J. Chem. Phys. **101**, 2106 (1994).

[50] F. Dong, S.-H. Lee and L. Liu, J. Chem. Phys. **113**, 3633 (2000).

[51] D. M. Neumark, A. M. Wodtke, G. N. Robinson, C. C. Heyden, Y. T. Lee, J. Chem. Phys. **82**, 3045 (1985).

[52] M. Faubel *et al.* J. Chem. Phys. **101**, 2106 (1994).

[53] T. C. Allison, S. L. Mielke, D. W. Schwenke, G. C. Lynch, M. S. Gordon, and D. G. Truhlar, in Gas-phase reaction systems: experiments and and models 100 years after Max Bodenstein, eds. H. -R. Volp, J. Wolfrum, R. Rannacher, and J. Warnatz (Springer, Heidelberg, 1996), p. 111.

[54] A. Wheeler, B. Topley and H. Eyring, J. Chem. Phys. **4**, 178 (1936).

[55] R. E. Weston Jr. J. Phys. Chem. **83**, 61 (1979).

[56] J. Bigeleisen, F. S. Klein, R. E. Weston, and M. Wolfsberg, J. Chem. Phys. **30**, 1340 (1959).

[57] C. A. Taatjes, Chem. Phys. Lett. **306**, 33 (1999).

[58] M. Alagia, N. Balucani, L. Cartechini *et al.* , Phys. Chem. Chem. Phys. **2**, 599 (2000).

[59] S. A. Kandel, A. J. Alexander, Z. H. Kim, and R. N. Zare, F. J. Aoiz, L. Bañares, and J. F. Castillo and V. Sáez Rábanos, J. Chem. Phys. **112**, 670 (2000).

[60] D. Skouteris, D. E. Manolopoulos, W. Bian, H. -J. Werner, L. -H. Lai, and K. Liu, Science **286**, 1713 (1999).

[61] U. Manthe, W. Bain, and H. -J. Werner, Chem. Phys. Lett. **313**, 647 (1999).

[62] K. Liu, Annu. Rev. Phys. Chem. **52**, 139 (2001) ; Int. Rev. Phys. Chem. **20**, 189 (2001).

[63] S. -H. Lee and K. Liu, J. Chem. Phys. **111**, 6253 (1999); S. -H. Lee, L. -H. Lai, K. Liu, and H. Chang, *ibid.* **110**, 8229 (1999); F. Dong, S. -H. Lee, and K. Liu, *ibid.* **115**, 1197 (2001).

[64] M. J. Ferguson, G. Meloni, H. Gomez, D. M. Neumark, J. Chem. Phys. **117**, 8181 (2002).

[65] A. Osterwalder, M. J. Nee, J. Zhou and D. M. Neumark, J. Chem. Phys. **121**, 6317 (2004).

[66] T. Takayanagi and Y. Kurosaki, J. Chem. Phys. **113**, 7158 (2000); **119**, 7838 (2003).

[67] W.-L. Quan, P.-Y. Tang and B.-Y. Tang, Int. J. Quant. Chem. **107**, 657 (2007).

[68] S. L. Mielke, G. J. Tawa, D. G. Truhlar and D. W. Schwenke, Chem. Phys. Lett. **234**, 57 (1995).

[69] S. L. Mielke, D. G. Truhlar and D. W. Schwenke, J. Phys. Chem. **99**, 16210 (1995).

[70] P. M. Aker, G. J. Germann and J. J. Valentini, J. Phys. Chem. **90**, 4795 (1989); **90**, 4809 (1989); **96**, 2756 (1992).

[71] C. S. Maierle, G. C. Schatz, M. S. Gordon *et al.* . J. Chem. Soc. Faraday Trans. **93**, 709 (1997).

[72] T. W. J. Whiteley, A. J. Dobbyn, J. N. L. Connor and G. C. Schatz, Phys. Chem. Chem. Phys. **2**, 549 (2000).

[73] G. C. Schatz, M. Hankel, T. W. J. Whiteley, and J. N. L. Connor, J. Phys. Chem. A **107**, 7287 (2003)

[74] A. I. Chichinin, J. Phys. Chem. Ref. Data **35**, 869 (2006).

[75] G. Capecchi and H.-J. Werner, Phys. Chem. Chem. Phys. **6**, 4975 (2004).

[76] J. C. Tully, J. Chem. Phys. **60**, 3042 (1974).

[77] S. A. Nizkorodov, W. W. Harper, W. B. Chapman, W. B. Blackmon and D. J. Nesbitt, J. Chem. Phys. **111**, 8404 (1999); S. A. Nizkorodov, W. W. Harper, and D. J. Nesbitt, Faraday Discuss. **113**, 107 (1999); W. W. Harper, S. A. Nizkorodov, and D. J. Nesbitt, J. Chem. Phys. **116**, 5622 (2002).

[78] F. Ausfelder, H. Kelso, and K. G. Mckendrick, Phys. Chem. Chem. Phys. **4**, 473 (2002); F. Ausfelder, K. G. Mckendrick, Prog. React. Kinet. Mech. **25**, 299 (2000); M. Brouard, P. O'keffe, and C. Vallance, J. Phys. Chem. A

106, 3629 (2002); M. Brouard, and C. Vallance, Phys. Chem. Chem. Phys. **3**, 3602 (2001); A. I. Chichinin, J. Chem. Phys. **112**, 3772 (2000).

[79] G. C. Schatz, J. Chem. Phys. **99**, 7522 (1995).

[80] M. H. Alexander, G. Chapecchi, and H. -J. Werner, Science **296**, 715 (2002).

[81] N. Balucani, D. Skouteris, L. Cartechini, G. Capozza, E. Segoloni, P. Casavecchia, M. H. Alexander, G. Chapecchi, and H. -J. Werner, Phys. Rev. Lett. **91**, 013201 (2003).

[82] S. Sato, J. Chem. Phys. **23**, 2465 (1955).

[83] M. J. Stwrn, A. Persky, F. S. Klein, J. Chem. Phys. **58**, 5697 (1973); Phys. Lett. **121**, 475 (1985);B. C. Garrett, D. G. Trhular, and A. W. Magnuson, J. Chem. Phys. **74**, 1029 (1981); I. Last, M. Bear, J. Chem. Phys. **75**, 288 (1981).

[84] D. W. Schwenke, S. C. Tucker, R. Steckler, F. B. Brown, G. C. Lynch, D. G. Truhlar, and B. C. Garrett, J. Chem. Phys. **90**, 3110 (1989).

[85] J. M. Launay and S. B. Padkjar, Chem. Phys. Lett. **181**, 95 (1991).

[86] S. E. Branchett, S. B. Padkjar and J. M. Launay, Chem. Phys. Lett. **208**, 523 (1993).

[87] T. C. Allison, G. C. Lynch, D. G. Truhlar, and M. S. Gordon, J. Phys. Chem. **100**, 13575 (1996).

[88] M. Alagia, N. Balucani, L. Cartechini, P. Casavecchia, E. H. van Kleef, G. G. Volpi, F. J. Aoiz, L. Bañares, D. W. Schwenke, T. C. Allison, S. L. Mielke, and D. G. Truhlar, Science **273**, 1519 (1996).

[89] S. L. Mielke, T. C. Allison, D. G. Trhular, and D. W. Schwenke, J. Chem. Phys. **100**, 13588 (1996).

[90] W. Bian and H.-J. Werner, J. Chem. Phys. **112**, 220 (2000).

[91] A. M. Arthurs and A. Dalgarno, Proc. R. Soc. Lond. A **256**, 540 (1960).

[92] C. F. Curtiss and F. T. Adler, J. Chem. Phys. **20**, 249 (1952); C. F. Curtiss, J. Chem. Phys. **21**, 2045 (1953); **49**, 1952 (1968).

[93] R. T. Pack, J. Chem. Phys. **60**, 633 (1974).

[94] H.-J. Werner, P. J. Knowles *et al. . MOLPRO version 2002.6, a package of* ab initio *programs, 2002*, see http://www.molpro.net/.

[95] M. H. Alexander, G. Capecchi and H.-J. Werner, Faraday Discuss. **127**, 59 (2004).

[96] U. Manthe, G. Capecchi and H.-J. Werner, Phys. Chem. Chem. Phys. **6**, 5026 (2004).

[97] G. A. Worth, M. H. Beck, A. Jäckle, and H. -D. Meyer, The MCTDH Package, Version 8.2, (2000), University of Heidelberg, Germany. H. -D. Meyer, Version 8.3, (2002). See http://www.pci.uni-heidelberg.de/tc/usr/mctdh/

[98] D. Kosloff and R. Kosloff, Comput. Phys. Commun. **30**, 333 (1983); J. Comput. Phys. **52**, 35 (1983).

[99] R. Kosloff, J. Phys. Chem. **92**, 2087 (1988); Ann. Rev. Phys. Chem. **45**, 145 (1994), and references therein.

[100] R. Kosloff, in *Numerical Grid Methods and Their Applications to Scrödinger's Equation*, edited by C. Cerjan (NATO ASI Ser. C**412**, Kluweru Academic Publishers, Dordrecht, The Netherlands, 1993), pp. 175-193.

[101] R. Kosloff, in *Time Dependent Methods for Quantum Dynamics*, NATO ASI Ser. B**229**, Plenum Press, New York, 1992.

[102] D. Kosloff and R. Kosloff, J. Comput. Phys. **52**, 35 (1983); Comput. Phys. Commum. **30**, 333 (1983).

[103] J. A. Fleck, Jr.. J. R. Morris and M. D. Feit, Appl. Phys. **10**, 129 (1976).

[104] M.D. Feit, J. A. Fleck, Jr., and A. Steiger, J. Comput. Phys. **47**, 412 (1982); M.D. Feit and J. A. Fleck, Jr. J. Chem. Phys. **78**, 301 (1983); J. Chem. Phys. **80**, 2578 (1984).

[105] D. Neuhauser, J. Chem. Phys. **103**, 8513 (1995); D. Neuhauser and M. Baer, J. Chem. Phys. **90**, 4351 (1981); D. Neuhauser, M. Baer, R. S. Judson and D. J. Kouri, J. Chem. Phys. **90**, 5882 (1990).

[106] J. W. Cooley and J. W. Tuckey, Math. Computation, **19**, 297 (1965).

[107] D. O. Harris, G. G. Engerholm, and W. D. Gwinn, J. Chem. Phys. **43**, 1515 (1965).

[108] A. S. Dickinson and P. R. Certain, J. Chem. Phys. **49**, 4209 (1968).

[109] G. C. Corey, J. W. Tromp and D. Lemoine, in Ref. [100], pp. 187-213.

[110] J. V. Lill, G. A. Parker, and J. C. Light, Chem. Phys. Lett. **89**, 483 (1982); J. C. Light, I. P. Hamilton, and J. V. Lill, J. Chem. Phys. **82**, 1400 (1985); J. P. Hamilton and J. C. Light, J. Chem. Phys. **84**, 306 (1986).

[111] R. M. Whitnell and J. C. Light, J. Chem. Phys. **90**, 1774 (1989).

[112] Z. Bačić and J. C. Light, Ann. Rev. Phys. Chem. **40**, 469 (1989).

[113] F. Rebentrost and W. A. Lester Jr., J. Chem. Phys. **63**, 3737 (1975); **64**, 3879 (1976); **64**, 4223 (1977).

[114] G. C. Schatz, P. McCabe, J. N. L Connor, Faraday Discuss. 110 (1998) 139; T. W. J. Whiteley, A. J. Dobbyn, J. N. L Connor, G. C. Schatz, Phys. Chem. Chem. Phys. 2 (2000) 549; G. C. Schatz, M. Hankel, T. W. J. Whiteley, J. N. L Connor, J. Phys. Chem. A, 107 (2003) 7278.

[115] P. McGuire and D. J. Kouri, J. Chem. Phys. **60**, 2488 (1974).

[116] A. Jäckle, M.-C. Heitz, and H.-D. Meyer, J. Chem. Phys. **110**, 241 (1999).

[117] S. Sukiasyan and H.-D. Meyer, J. Chem. Phys. **116**, 10641 (2002).

[118] A. Aguado, M. Paniagua, M. Lara, and O. Roncero, J. Chem. Phys. **107**, 10085 (1997).

[119] S. K. Gray and G. G. Balint-Kurti, J. Chem. Phys. **108**, 950 (1998); S. K. Gray, C. Petrongolo, K. Drukker, and G. C. Schatz, J. Phys. Chem. A **103**, 9448 (1999); S. K. Gray, G. G. Balint-Kurti, G. C. Schatz, J. J. Lin, X. Liu, S. Harich, and X. Yang, J. Chem. Phys. **113**, 7330 (2000), and references therein.

[120] D. H. Zhang and J. Z. H. Zhang, J. Chem. Phys. **103**, 6512 (1995); D. H. Zhang and S.-Y. Lee, J. Chem. Phys. **110**, 4435 (1999).

[121] U. Manthe and H. Köppel, J. Chem. Phys. **93**, 345 (1990); **93**, 1685 (1990).

[122] D. T. Colbert and W. H. Miller, J. Chem. Phys. **96**, 1982 (1992).

[123] C. C.-Tannoudji, B. Diu, and F. Laloë, *Quantum Mechanics* (John Wiley & Sons, New York, Hermann, Vol. I, 1977).

[124] H. Tal-Ezer and R. Kosloff, J. Chem. Phys. **81**, 3967 (1984).

[125] V. A. Mandelshtam and H. S. Taylor, J. Chem. Phys. **103**, 2903 (1995).

[126] A. Askar and A. S. Cakmak, J. Chem. Phys. **68**, 2794 (1978).

[127] S. K. Gray and D. E. Manolopoulos, J. Chem. Phys. **104**, 7099 (1996).

[128] S. K. Gray and G. G. Balint-Kurti, J. Chem. Phys. **108**, 950 (1998).

[129] T. J. Park and J. C. Light, J. Chem. Phys. **85**, 5870 (1986).

[130] M. D. Feit, J. A. Fleck, Jr., and A. Steiger, J. Comput. Phys. **47**, 412 (1982).

[131] E. Merzbacher, *Quantum Mechanics*, (Wiley, New York, 1970).

[132] G. C. Corey and D. Lemoine, J. Chem. Phys. **97**, 4115 (1992); A. R. Offer and G. G. Balint-Kurti, J. Chem. Phys. **101**, 10416 (1994).

[133] F. Le Quéré and C. Leforestier, J. Chem. Phys. **92**, 247 (1990); C. Leforestier, J. Chem. Phys. **94**, 6388 (1991).

[134] D. Neuhauser and M. Baer, J. Phys. Chem. **93**, 2872 (1989); J. Chem. Phys. **90**, 4351 (1989); J. Chem. Phys. **91**, 4651 (1989). D. Neuhauser, M. Baer, R. S. Judson, and D. J. Kouri, Comput. Phys. Commun. **63**, 460 (1991).

[135] S. Mahapatra and N. Sathyamurthy, J. Chem. Soc. Faraday Trans. **93**, 773 (1997).

[136] T. J. Park and J. C. Light, J. Chem. Phys. **88**, 4897 (1988); W. H. Miller, J. Phys. Chem. **102**, 793 (1998) and references therein.

[137] D. Neuhauser and M. Baer, J. Chem. Phys. **91**, 4651 (1989); D. Neuhauser, M. Baer, R. S. Judson, and D. J. Kouri, J. Chem. Phys. **93**, 312 (1990).

[138] F. J. Aoiz, L. Bañares, and J. F. Castillo, J. Chem. Phys. **111**, 4013 (1999).

[139] S. K. Gray, C. Petrongolo, K. Drukker, and G. C. Schatz, J. Phys. Chem. A **103**, 9448 (1999); K. Drukker and G. C. Schatz, J. Chem. Phys. **111**, 2451 (1999); S. K. Gray, G. G. Balint-Kurti, G. C. Schatz, J. J. Lin, X. Liu, S. Harich, and X. Yang, J. Chem. Phys. **113**, 7330 (2000).

[140] G. C. Schatz, P. McCabe, and J. N. L Connor, Faraday Discuss. **110**, 139 (1998); T. W. J. Whiteley, A. J. Dobbyn, J. N. L Connor, and G. C. Schatz, Phys. Chem. Chem. Phys. **2**, 549 (2000); G. C. Schatz, M. Hankel, T. W. J. Whiteley, and J. N. L Connor, J. Phys. Chem. A, **107**, 7278 (2003).

[141] W. H. Press, B. P. Flannery, S. A. Teukolsky, and W. T. Vatterling, *Numerical Recipes: The Art of Scientific Computing* (Cambridge University Press, Cambridge, England, 1986).

[142] D. Kita and D. H. Stedman, J. Chem. Soc. Faraday Trans. 2, **78**, 1249 (1982).

[143] J. A. Lee, J. V. Michael W. A. Payne and L. J. Stief, J. Chem. Soc. Faraday Trans. 1, **73**, 1530 (1977).

[144] S. S. Kumaran, K. P. Lim and J. V. Michael, J. Chem. Phys. **101**, 9487 (1994).

[145] A. A. Westnberg and N. de Haas, J. Chem. Phys. **48**, 4405 (1968).

[146] D. E. Manolopoulos, K. Stark, H. -J. Werner, D. W. Arnold, S. E. Bradforth and D. M. Neumark, Science **262**, 1852 (1993).

[147] D. A. Wild, R. L. Wilson, P. S. Weiser, E. J. Bieske, J. Chem. Phys. **113**, 824 (2001).

[148] M. H. Alexander, J. Chem. Phys. **118**, 9637 (2003).

[149] R. Kosloff and H. Tal-Ezer, Chem. Phys. Lett. **127**, 223 (1986).

[150] S. Mahapatra, H. Köppel, Phys. Rev. Lett. **81**, 3316 (1998).

[151] G. M. Krishanan, S. Mahapatra, J. Chem. Phys. **115**, 6951 (2001).

[152] D. E. Manolopolous, M. Alexander, Phys. Chem. Chem. Phys. **6**, 4984 (2004).

[153] S. Mahapatra, H. Köppel, J. Chem. Phys. **109**, 1721 (1998).

[154] B. Lepetit, Z. Peng, A. Kuppermann, Chem. Phys. Lett. **166**, 572 (1990).

[155] A. Stolow, A. E. Bragg, D. M. Neumark, Chem. Rev. **104**, 1719 (2004); D. M. Neumark, Annu. Rev. Phys. Chem. **52**, 255 (2001); Science, **272**, 1446 (1997); Acc. Chem. Res. **26**, 33 (1993).

[156] P. G. Wenthold, C. Lineberger, Acc. Chem. Res. **32**, 597 (1999).

[157] R. E. Continetti, Int. Rev. Phys. Chem. **17**, 227 (1998); Annu. Rev. Phys. Chem. **52**, 165 (2001).

[158] H.-J. Deyerl, T. G. Clements, A. K. Luong, R. E. Continetti, J. Chem. Phys. **115**, 6931 (2001). K. A. Hanold, M. C. Garner, R. E. Continetti, Phys. Rev. Lett. **77**, 3335 (1996); T. G. Clements, H.-J. Deyerl, R. E. Continetti, J. Phys. Chem. A **106**, 279 (2002); Z. Lu, R. E. Continetti, J. Phys. Chem. A **108**, 9962 (2004).

[159] T. G. Clements, R. E. Continetti, J. S. Francisco, J. Chem. Phys. **117**, 6478 (2002).

[160] R. T. Skodje, R. Sadeghi, H. Köppel, J. L. Krause, J. Chem. Phys. **101**, 1725 (1994).

[161] A. A. Buchachenko, T. A. Grinev, J. Kłos, E. J. Bieske, M. M. Szcześniak, G. Chałasiński, J. Chem. Phys. **119**, 12931 (2003).

[162] M. J. Molina, F. S. Rowland, Nature (London), **249**, 810 (1974); V. Vaida, S. Solomon, E. C. Richard, E. Ruhl, A. Jefferson, *ibid.* **342**, 405 (1989); F. S. Rowland, Annu. Rev. Phys. Chem. **42**, 731 (1991) and references therein.

[163] V. Vaida, J. D. Simon, Science, **268**, 1443 (1995); H. F. Davis, Y. T. Lee, J. Phys. Chem. **96**, 5681 (1992); J. Chem. Phys. **105**, 8142 (1996); P. J. Reid, Acc. Chem. Res. **34**, 691 (2001); M. K. Gilles, M. L. Polak, W. C. Lineberger, J. Chem. Phys. **96** 8102 (1996); X.-B. Wang, L.-S. Wang, J. Chem. Phys. **113**, 10928 (2001).

[164] F. Motte-Tollet, J. Delwiche, J. Heinesch, M.-J. Hubin-Franskin, J. M. Gingell, N. C. Jones, N. J. Mason, G. Marston, Chem. Phys. Lett. **284**, 452 (1998).

[165] K. A. Peterson, H.-J. Werner, J. Chem. Phys. **96**, 8948 (1992); **99**, 302 (1993); **105**, 9823 (1996); K. A. Peterson, *ibid.* **109**, 8864 (1998).

[166] D.-C. Wang, E. P. F. Lee, F.-T. Chau, D. K. W. Mok, J. M. Dyke, J. Phys. Chem. A **104**, 4936 (2000); D. K. W. Mok, E. P. F. Lee, F.-T. Chau, D.-C. Wang, J. M. Dyke, J. Chem. Phys. **113**, 5791 (2000).

[167] S. Mahapatra, G. M. Krishnan, J. Chem. Phys. **115**, 6951 (2001).

[168] G. M. Krishnan, S. Mahapatra, J. Chem. Phys. **118**, 8715 (2003); S. Mahapatra, Th. Ritschel, Chem. Phys. **289**, 291 (2003).

[169] S. Mahapatra, J. Chem. Phys. **116**, 8817 (2002).

[170] S. Mahapatra, Int. Rev. Phys. Chem. **23**, 483 (2004).

[171] A. B. Conford, D. C. Frost, F. G. Herring, C. A. McDowell, J. Chem. Phys. **55**, 2820 (1971).

[172] C. R. Brundle, M. B. Robin, N. A. Kuebler, H. Basch, J. Am. Chem. Soc. **94**, 1451 (1972).

[173] W. von Niessen, *J. Electron Spectrosc. Relat. Phenom.*, **17**, 197 (1979); K. E. Valenta, K. Vasudevan, F. Grein, J. Chem. Phys. **72**, 2148 (1980); S. R. Langhoff, D. P. Chong, Chem. Phys. Lett. **86**, 487 (1982); P. Decleva, A. Lisini, Chem. Phys. **106**, 39 (1986); C.-H. Hu, D. P. Chong, M. E. Casida, J. Electron Spectrosc. Relat. Phenom. **85**, 39 (1997).

[174] D.-C. Wang, F.-T. Chau, D. K.-W. Mok, E. P. F. Lee, L. Beeching, J. S. Ogden, J. M. Dyke, J. Chem. Phys. **114**, 10682 (2001).

[175] P. Tomasello, M. Ehara, H. Nakatsuji, J. Chem. Phys. **116**, 2425 (2002); *ibid.* **118**, 5811 (2003).

[176] J. Cullum, R. Willoughby, *Lanczos Algorithms for Large Symmetric Eigenvalue Problems* (Birkhäuser, Boston, 1985), Vols. I and II.

[177] S. Mahapatra, *"Vibronic coupling and nonadiabatic molecular dynamics", in: Reviews in Modern Quantum Chemistry: A Celebration of the Contributions of Robert Parr*, Ed., K. D. Sen, (World Scientific, Singapore, 2002) pp. 359-400.

[178] R. T. Pack, G. A. Parker, J. Chem. Phys. **87**, 3888 (1987).

[179] E. B. Jr. Wilson, J. C. Decius, P. C. Cross, *Molecular Vibrations* (McGraw-Hill, New York, 1955).

[180] L. Pierce, N. DiCianni, R. Jackson, J. Chem. Phys. **38**, 730 (1963).

[181] T. H. Jr. Dunning, J. Chem. Phys. **90**, 1007 (1989).

[182] M. J. Frisch, *et al.* Gaussian 03, Revision B. 05, Gaussian, Inc., Pittsburgh PA, 1998.

[183] W. Domcke, H. Köppel, L. S. Cederbaum, *Mol. Phys.*, **1981**, 43, 851.

[184] A. J. C. Varandas, H.-G. Yu, Chem. Phys. Lett. **259**, 336 (1996); S. Mahapatra, H. Köppel, J. Chem. Phys. **109**, 1721 (1998).

[185] W. Domcke, G. Stock, Adv. Chem. Phys. **100**, 1 (1997).

[186] H. Köppel, W. Domcke, *Encyclopedia of Computational Chemistry*, Ed,. Schleyer, P. v. R. (Wiley, New York, 1998).

[187] M. R. Wall, D. Neuhauser, J. Chem. Phys. **102**, 8011 (1995); V. A. Mandelshtum, H. S. Taylor, Phys. Rev. Lett. **78**, 3274 (1997); J. Chem. Phys. **107**, 6756 (1997).

[188] U. Manthe, H.-D. Meyer, L. S. Cederbaum, J. Chem. Phys. **97**, 3199 (1992); V. Engel, Chem. Phys. Lett. **189**, 76 (1992).

[189] E. M. Goldfield, A. J. H. M. Meijer, J. Chem. Phys. **113**, 11055 (2000); T. E. Carroll, E. M. Goldfield, J. Phys. Chem. A, **105**, 2251 (2001); S. Sukiasyan, H. -D. Meyer, J. Chem. Phys. **116**, 10641 (2002).

Appendix A

Appendix

A.1 Electronic nonadiabatic transition in the photoelectron spectroscopy of F_2O

Spectroscopy and dissociation dynamics of halogen oxides have attracted increasing attention in the literature because of their relevance in the photochemistry of the stratosphere and they apparently involved directly or indirectly in the depletion of ozone layer [162]. The molecules of oxygen and chlorine have been studied extensively both theoretically and experimentally [163–170]. In contrast, the photophysics and photochemistry of difluorine oxide, F_2O, has received only scant attention in the literature [171–173]. The photoelectron spectra of halogen dioxide and dihalogen oxides are found to be particularly appealing because they bear signatures of nonadiabatic interactions in the final excited electronic states [167–170]. The photoelectron spectra usually have poor energy resolution, however, they have often been used to estimate the extent of nonadiabatic interactions and thereby facilitating the development of theoretical models to examine

the nuclear dynamics in the excited electronic states.

F_2O is a nonlinear triatomic molecule with a C_{2v} geometry at its equilibrium configuration. The ultraviolet photoelectron spectrum of F_2O was first recorded by Conford and coworkers [171] and then by Brundle and coworkers [172]. The observed bands were assigned based on the semi empirical electronic structure data. Both these experiments assigned the first four electronic states of F_2O^+ in the order $^2B_1$, $^2A_1$, $^2B_2$ and $^2A_2$. An alternative assignment was also proposed by Brundle and coworkers [172], in which the overlapping second and the third photoelectron bands were assigned to the $^2A_1$, $^2B_2$ and $^2A_2$ electronic states. Theoretical calculations of the ionization energies of the low-lying electronic states of F_2O^+ appeared thereafter. However, the energetic ordering of the three cationic states ($^2A_1$, $^2B_2$ and $^2A_2$) still remained controversial. Recently Wang. *et al.* [174] have reported high level *ab initio* calculation on the near equilibrium C_{2v} potential energy surfaces (PESs) of the ground electronic state of F_2O and the ground and the low-laying excited states of F_2O^+ . The three excited electronic states of the latter are shown to be $^2B_2$, $^2A_1$ and $^2A_2$ in the order of ascending energy. This energetic ordering was reconfirmed latter by Tomasello *et al.* [175] by symmetry-adapted-cluster-configuration-interaction calculations. Wang *et al.* [174] also reported the harmonic and anharmonic Franck-Condon (FC) simulation of the photoelectron bands employing the C_{2v} PESs and have shown that the results are generally in good agreement with the experiment. None of the theoretical studies to date have considered any nonadiabatic interactions in the excited electronic states and their impact on the photoelectron spectrum of F_2O.

We in the following, revisit the photoelectron bands of F_2O and theoretically study them with the aid of a time-dependent wave packet (WP) as well as a Lanczos based time-independent quantum mechanical approach [10, 37, 99, 176,

177]. We consider the relevant nonadiabatic interactions in the excited electronic states of F_2O^+ and modeled them in our theoretical approach. The PESs reported by Wang *et al.* [174] for the C_{2v} geometry of F_2O and F_2O^+ are extended to the C_s configurations in this study assuming a harmonic vibration along the asymmetric stretching mode. The electronic nonadiabatic interactions between the $\widetilde{A}\,^2B_2$ and $\widetilde{B}\,^2A_1$ excited electronic states of F_2O^+ are modeled by devising a diabatic electronic Hamiltonian within a linear vibronic coupling approach [10]. The linear vibronic coupling parameter is calculated by an *ab initio* method and conical intersections [10, 12] between the two electronic states are established. The SO interactions between the near degenerate $\widetilde{B}\,^2A_1$ and $\widetilde{C}\,^2A_2$ electronic states of F_2O^+ is not considered in this study primarily because of relatively weak SO coupling due to F atom. We have considered $\sim 10\%$ contribution of the $\widetilde{C}\,^2A_2$ band to the composite overlapping second and third photoelectron bands. The importance of the nonadiabatic interactions between the $\widetilde{A}\,^2B_2$ and $\widetilde{B}\,^2A_1$ electronic states is further examined by monitoring the nonradiative decay of the electronic population in the coupled electronic manifold.

We also calculated the first photoelectron band of F_2O and find that it compares well with the experimental results at low energy resolution. The peaks in the spectrum are ~ 0.13 eV spaced in energy which corresponds to a progression along the symmetric stretching mode of F_2O^+. Major contribution to the intensity of overlapping second photoelectron band comes from the interacting $\widetilde{A}\,^2B_2$ and $\widetilde{B}\,^2A_1$ electronic states and a minor contribution is considered from the $\widetilde{C}\,^2A_2$ electronic state. The theoretical results compare well with the experimental recording [174].

A.2 Theoretical Framework

A.2.1 The vibronic Hamiltonian

The first photoelectron band of F_2O pertinent to a transition to the $\widetilde{X}\ ^2B_1$ electronic state of F_2O^+ is essentially described by the nuclear motion on the Born-Oppenheimer PES of the latter. This is because the ground electronic state of F_2O^+ is energetically well separated ($\sim$ 4.56 eV at the equilibrium configuration) from its first excited electronic state. The second, third and the fourth photoelectron bands, on the other hand, are highly overlapping and are proposed here to be due to the nonadiabatic interactions among the three low-lying near degenerate excited electronic states ($\widetilde{A}\ ^2B_2$, $\widetilde{B}\ ^2A_1$ and $\widetilde{C}\ ^2A_2$) of F_2O^+. To describe the associated nonadiabatic interactions we resort to a diabatic electronic representation [10] in which the coupling between the states is described by smoothly varying off-diagonal elements of the electronic Hamiltonian. In absence of any relativistic effects, the representative Hamiltonian to describe the first four photoelectron bands of F_2O is given by

$$\begin{aligned} \mathcal{H} &= \mathcal{H}^{Nu} + \mathcal{H}^{el} \\ &= T_N \begin{pmatrix} 1 & 0 & 0 & 0 \\ 0 & 1 & 0 & 0 \\ 0 & 0 & 1 & 0 \\ 0 & 0 & 0 & 1 \end{pmatrix} + \begin{pmatrix} \mathcal{U}_{11} & 0 & 0 & 0 \\ 0 & \mathcal{U}_{22} & \mathcal{U}_{23} & 0 \\ 0 & \mathcal{U}_{32} & \mathcal{U}_{33} & 0 \\ 0 & 0 & 0 & \mathcal{U}_{44} \end{pmatrix}, \end{aligned} \tag{A.1}$$

where $\mathcal{H}^{Nu}$ and $\mathcal{H}^{el}$ represents the nuclear and the electronic part of the Hamiltonian matrix, respectively, T_N is the nuclear kinetic energy operator and $\mathcal{U}_{ii}$ describe the potential energies of the electronic states of F_2O^+ (i=1, 2, 3 and 4 refer to the $\widetilde{X}\ ^2B_1$, $\widetilde{A}\ ^2B_2$, $\widetilde{B}\ ^2A_1$ and $\widetilde{C}\ ^2A_2$ electronic states, respectively).

The quantity $\mathcal{U}_{23} = \mathcal{U}_{32}$ represents the nonadiabatic coupling potential between the $\widetilde{A}\ ^2B_2$ and $\widetilde{B}\ ^2A_1$ electronic states.

F_2O is a bent molecule and has a C_{2v} minimum in the neutral ground electronic state and the cationic ground and excited electronic states. In order to exploit this symmetry explicitly in the nuclear dynamical simulations we express the elements of the above Hamiltonian matrix in terms of the symmetry-adapted ordinary Jacobi coordinates pertinent to the C_{2v} point group in the body-fixed frame. In the following, we refer to r as the distance between the two terminal F atoms, R as the distance between the O atom to the center-of-mass of the two F atoms and γ as the angle between $\vec{r}$ and $\vec{R}$. The nuclear kinetic energy operator for the total angular momentum J=0 can be represented as:

$$T_N = -\frac{\hbar^2}{2\mu}\frac{\partial^2}{\partial r_d^2} - \frac{\hbar^2}{2\mu'}\frac{\partial^2}{\partial r_v^2} - \frac{\hbar^2}{2I}\frac{1}{\sin\gamma}\frac{\partial}{\partial\gamma}\left(\sin\gamma\frac{\partial}{\partial\gamma}\right), \tag{A.2}$$

where,

$$\mu = \frac{2m_F m_0}{m_O + 2m_F} \quad and \quad \mu' = \frac{m_F}{2}.$$

The quantity m_F and m_0 denote the masses of the fluorine and oxygen atom and I denotes the three-body moment of inertia.

The use of this symmetry adapted Jacobi coordinates for the present example is advantageous over hyperspherical coordinates [178] because it leads to a block-diagonal structure of the Hamiltonian based on the vibronic symmetries. This consideration simplifies the numerical computation significantly by reducing the grid size by a factor of two, when the $\widetilde{A}\ ^2B_2$ -$\widetilde{B}\ ^2A_1$ coupled electronic manifold is considered.

A.2.2 Details of the *ab initio* electronic potential energy surfaces and the vibronic coupling parameter

The elements of the electronic Hamiltonian matrix $\mathcal{H}^{el}$ of Eq. (A.1) have been determined in the following way. For the dependence of the potential energy surfaces $\mathcal{U}_{11}$, $\mathcal{U}_{22}$, $\mathcal{U}_{33}$ and $\mathcal{U}_{44}$ on the symmetric stretch coordinate, $S_1 = (\Delta r_1 + \Delta r_2)/\sqrt{2}$ (Δr_1 and Δr_2 are the displacements in FO bond lengths) and bending coordinates, $S_2 = \Delta\theta + \alpha\Delta\theta^2 + \beta\Delta\theta^3$, ($\Delta\theta$ being the displacements in FOF bond angle; α and β are related by an expression, $\beta = [1 + 3\alpha(\pi\text{-}\theta_{eqm})^2]/[\text{-}2(\pi\text{-}\theta_{eqm}]$, by restricting the energy gradient in S_2 to zero when the molecule is linear, θ_{eqm} is the equilibrium value of the FOF angle), *i.e.* for C_{2v} geometries, the MRCI potential energy functions derived from the large scale CASSCF/RCCSD(T)/cc-pVQZ calculations by Wang *et al.* [174] is used. These authors have fitted the potential energies to a polynomial of the form

$$V = \sum_{ij} C_{ij}(\Delta S_1)^i(\Delta S_2)^j + V_{eqm} \tag{A.3}$$

The above function for the ground electronic state of F_2O and F_2O^+ is described by sixteen coefficients and by fourteen coefficients for the excited electronic states of F_2O^+. The quantity V_{eqm} is the potential energy at the equilibrium configuration in the respective electronic state. The details of the *ab initio* calculations can be found in Ref. [174]. The dependence of these PESs on the asymmetric stretch coordinate, $S_3 = (\Delta r_1 \text{ - } \Delta r_2)/\sqrt{2}$, is approximated by a Harmonic potential, $V(S_3) = \kappa_u S_3^2/2 = \omega_u Q_u^2/2$. The quantity κ_u is the force constant along the asymmetric stretching vibration (u symmetry) and ω_u is the harmonic vibrational frequency. The quantity Q_u represents the dimensionless normal coordinate of the asymmetric stretching vibration (see the details below). The harmonic ap-

proximation along the asymmetric stretching motion is employed because the mentioned photoelectron bands of the F_2O apparently do not show any noticeable excitation along this vibration.

We devote some space here to introduce the dimensionless normal coordinates. These are denoted as Q_{g1}, Q_{g2} and Q_u for the symmetric stretching, bending and asymmetric stretching vibrational motions of F_2O in its ground electronic state pertinent to the C_{2v} symmetry point group. The vibrational motion in this state is treated as harmonic. The mass-weighted normal coordinates of F_2O are then calculated by the GF-matrix method of Wilson *et al.* [179] using the experimentally derived force field of Pierce *et al.* [180]. They are then transformed to the dimensionless normal coordinates by multiplying with $(\omega_i/\hbar)^{1/2}$ (ω_i is the frequency of the i^{th} vibrational mode). The frequencies of the asymmetric stretching vibration of the neutral and the cationic electronic states used to describe the PESs employed in this study are 0.1137 eV, 0.1670 eV, 0.1678 eV, 0.2246 eV 0.0714 eV for the ground electronic states of F_2O and the $\mathcal{U}_{11}$, $\mathcal{U}_{22}$, $\mathcal{U}_{33}$ and $\mathcal{U}_{44}$ electronic states of F_2O^+ reported by Wang *et al.* [174]. The diabatic coupling potential between $\mathcal{U}_{22}$ and $\mathcal{U}_{33}$ is assumed to be linearly varying function of Q_u, $\mathcal{U}_{23} = \mathcal{U}_{32} = \lambda Q_u$, λ being the linear vibronic coupling parameter. We note that the present model treats all the higher order couplings in the Hamiltonian along the symmetric stretch and bending coordinates whereas a linear coupling scheme is applied to the asymmetric stretch coordinate only.

The interstate linear vibronic coupling parameter λ is derived from the difference of the adiabatic potential energies of the $\widetilde{A}\ ^2B_2$ and $\widetilde{B}\ ^2A_1$ electronic states, calculated for the various C_s geometries of F_2O^+. The two are related

via [10]

$$\lambda = \frac{1}{2} Q_u^{-1} \left\{ [V_2(Q_u) - V_1(Q_u)]^2 - [V_2(\boldsymbol{Q_0}) - V_1(\boldsymbol{Q_0})]^2 \right\}^{1/2}, \qquad \text{(A.4)}$$

where V_1 and V_2 are the adiabatic potential energies of the $\widetilde{A}\,^2B_2$ and $\widetilde{B}\,^2A_1$ electronic states, respectively, for the distorted nuclear configuration Q_u. The latter is chosen in the vicinity of $\boldsymbol{Q_0}$ (equilibrium configuration of the ground electronic state of F_2O), $Q_u = \boldsymbol{Q}_0 \pm \delta$, with δ being the small shift applied to change the symmetry point group from C_{2v} at $\boldsymbol{Q_0}$ to C_s at Q_u.

In order to calculate λ we perform *ab initio* calculations for the adiabatic potentials V_2 and V_1 for different values of Q_u around the equilibrium geometries of the neutral and cationic electronic states. We have also optimized the equilibrium geometry of the ground electronic state of F_2O employing the correlation consistent polarized valence triple-ζ (cc-pVTZ) Gaussian basis sets of Dunning [181]. The electronic structure calculations are performed using the GAUSSIAN [182] program package. The effect of electron correlation is treated by the second order Møller-Plesset perturbation theory (MP2). This yields r (O-F bond length)= 1.40 Åand θ (F-O-F angle) = 103.17° for the optimized ground state equilibrium geometry of F_2O to be compared with the corresponding values derived from microwave spectroscopy, r = 1.4053 Åand θ = 103.07° [174]. We performed direct calculations of the vertical ionization energies of F_2O using the outer-valence Green's function (OVGF) method employing the same cc-pVTZ basis set and equated them to the adiabatic potential energies V_1 and V_2. The Green's function calculations are carried out for the following combinations of r and ϕ and for the displacement Δr= 0.0, 0.01, 0.1 and 0.2 Å: (i) r = 1.4001 Å, ϕ = 103.17° (MP2/cc-pVTZ equilibrium geometry of F_2O ground state), (ii)

$r = 1.4053$ Å, $\phi = 103.07°$ (experimental equilibrium geometry of F_2O ground state), (iii) $r = 1.2715$ Å, $\phi = 107.99°$ (MP2/cc-pVTZ equilibrium geometry of the $\widetilde{X}\ ^2B_1$ state of F_2O^+), (iv) $r = 1.331$Å, $\phi = 107.3°$ (IFCA (harmonic) equilibrium geometry of the $\widetilde{X}\ ^2B_1$ state of F_2O^+), (v) $r = 1.323$ Å, $\phi = 107.30°$ (IFCA (anharmonic) equilibrium geometry of the $\widetilde{X}\ ^2B_1$ state of F_2O^+) (vi) $r = 1.4437$ Å, $\phi = 82.28°$ (CCSD(T)/aug-cc-pVTZ equilibrium geometry of the $\widetilde{A}\ ^2B_2$ state of F_2O^+), (vii) $r = 1.3689$ Å, $\phi = 118.57°$ (CCSD(T)/aug-cc-pVTZ equilibrium geometry of the $\widetilde{B}\ ^2A_1$ state of F_2O^+). The displacements are then transformed into dimensionless normal coordinates and λ is calculated using the calculated OVGF data and Eq. (A.4). Such an analysis yields 0.05 eV $\leq \lambda \leq$ 0.28 eV, with an average value of $\lambda \sim 0.18$ eV.

A.3 Calculation of the Photoelectron spectrum and Electronic Populations

The photoionization process is described by Fermi's Golden rule. The excitation function is given by

$$P(E) = \sum_v |\langle \Psi_v | \hat{T} | \Psi_0 \rangle|^2 \delta(E - E_v + E_0), \tag{A.5}$$

where $|\Psi_0\rangle$ is the initial state; the vibrational and electronic ground state of the neutral F_2O with energy E_0, which is assumed to be vibronically decoupled from all other states. $|\Psi_v\rangle$ is the final vibronic state of the radical cation F_2O^+ with energy E_v. The operator $\hat{T}$ is the transition operator, which describes the interaction of the electron with the external radiation with energy E. In the present

application the initial and final states can be expressed as

$$|\Psi_0\rangle = |\phi^0\rangle|\chi_0^0\rangle,$$
$$|\Psi_v\rangle = \sum_n |\phi^n\rangle|\chi_v^n\rangle, \tag{A.6}$$

where $|\phi\rangle$ and $|\chi\rangle$ refer to the (diabatic) electronic and vibrational parts of the wavefunction, respectively. The superscripts 0 and n refer to the electronic ground state of F_2O and excited n^{th} electronic state of F_2O^+, respectively. Using Eq. (A.6) the spectral intensity can be rewritten within the Condon approximation as [10]

$$P(E) = \sum_v |\tau^n \langle\chi_v^n|\chi_0^0\rangle|^2 \delta(E - E_v + E_0), \tag{A.7}$$

with

$$\tau^n = \langle\phi^n|\hat{T}|\phi^0\rangle, \tag{A.8}$$

being the transition operator matrix elements of the final electronic state n. In rewriting Eq. (A.7), the matrix elements of the transition operator are considered to be weakly varying function of the nuclear coordinates. These elements are not calculated in the present study and are treated as constants (or adjusted empirically by examining the experimental data), in accordance with the applicability of the generalized Condon approximation in the diabatic electronic basis [183].

To calculate the photoelectron spectrum using a time-dependent formalism the Fourier transform representation of the Dirac delta function is used in the Golden rule formula in Eq. (A.7). The resulting expression can then be reduced to the Fourier transformation of the time autocorrelation function of the WP [10,35]. When the interacting electronic states possess different spatial symmetries, a vibronic symmetry exists and the vibronic secular matrix becomes block diagonal

upon a suitable ordering of basis states. The Golden rule expression is then rearranges to

$$P(E) \sim 2\mathrm{Re} \int_0^\infty e^{iEt/\hbar} C^k(t) dt, \tag{A.9}$$

where the index k goes over to the component (diabatic) electronic states, $C^k(t) = \langle \chi^k(t=0) | e^{-i\mathcal{H}t/\hbar} | \chi^k(t=0) \rangle$. The integral in Eq. (A.9) equals to i ($=\sqrt{-1}$) times the expectation value of the casual Green's function in the initial WP representation [see for example, Ref [10]]. Therefore, the imaginary part of this expectation value finally contributes to $P(E)$. The autocorrelation function is evaluated by solving the time-dependent Schrödinger equation numerically on a grid. For an explicitly time-independent Hamiltonian the solution reads

$$\chi^k(t) = \exp\left[-i\mathcal{H}t/\hbar\right] \chi^k(t=0). \tag{A.10}$$

We solve Eq. (A.10) numerically on a grid in the r_d, r_v and γ space in order to calculate the wavefunction at time t from that at time $t = 0$. A 128×64 spatial grid is used in the $r_d \times r_v$ plane with 1.0 $a_0 \leq r_d \leq 4.556$ a_0 and 1.0 $a_0 \leq r_v \leq 6.985$ a_0. The grid along the Jacobi angle γ is chosen as the nodes of a 48-point Gauss-Legendre quadrature (GLQ). The action of the exponential operator on $|\chi^k(t = 0)\rangle$ is carried out by dividing the total propagation time t into N steps of length Δt. The exponential operator at each Δt is then approximated by a second-order split-operator method [103,104], adapted to the present coupled state problem as discussed in the literature [184]. This is used in conjunction with the fast Fourier transform method to evaluate the exponential containing the radial kinetic energy operator [102] and with the discrete variable representation method to evaluate the exponential containing the rotational kinetic energy operator ($\boldsymbol{j}^2/2I$) on the wave function [132]. The latter is accomplished by transforming the grid wave

function to the angular momentum basis (finite basis representation), multiplying it by the diagonal value of the operator ($e^{-ij(j+1)\Delta t\hbar/4I}$), and then transforming it back to the grid representation. The WP is evolved for a total of 1.103 ps with a time step Δt=0.1347 fs. The last 16 points of the grid along r_d and 8 points along r_v were covered with a damping function [135] in order to avoid any unphysical reflexion or wraparound of the high energy components of the WP which reach the finite-sized grid boundaries at longer time.

The initial vibrational wave function $|\chi_0^0\rangle$ pertinent to the ground electronic state of F_2O is calculated by a Lanczos based relaxation method [149]. The *ab initio* potential energy surface for the ground electronic state of F_2O reported by Wang *et al.* [174] for the C_{2v} configurations is extended to the C_s geometries assuming a harmonic vibration along the asymmetric stretching mode, is used for the relaxation calculations. The time propagation is carried out by the short iterative Lanczos method [149] with variable time steps. This yields a zero point energy of 0.097 eV for the neutral F_2O. The ground vibrational wavefunction of the neutral obtained by this method is referred to as anharmonic in the rest of this paper. This initial wave function is then subjected to a FC transition and propagated with the final state Hamiltonian (as discussed above). At each time step the autocorrelation function is recorded and the spectral intensity is finally calculated using Eq. (A.9).

The time-dependence of the diabatic as well as adiabatic electronic populations are of immense importance in understanding the nonradiative decay dynamics of the optically prepared state mediated by the conical intersections [10, 185]. These are calculated by defining adiabatic projectors in the diabatic electronic representation [10, 121].

In the following, we also report the results obtained by diagonalizing the vi-

bronic Hamiltonian using the Lanczos algorithm [176] within a time-independent quantum mechanical framework. A similar grid as stated above is used for the purpose. In this method the initial wavefunction is written as a direct product harmonic oscillator function along the Q_{g1}, Q_{g2} and Q_u vibrational modes of F_2O. In this case the intensity of the vibronic lines is shown to be the square of the first component of the Lanczos eigenvectors [186]. In case of the anharmonic initial wavefunction (discussed above), this formalism can not be used and a filter diagonalization approach will be most effective [187]. This is beyond the scope of the present study and will be considered in future study.

A.4 Results and Discussion

We show the photoelectron bands of F_2O calculated with the Hamiltonian of Eq. (A.1) and compare the theoretical results with the available experimental data [171, 172, 174] in this section. The structure of the Hamiltonian matrix in Eq. (A.1) reveals that the nuclear dynamics can be treated independently on the $\mathcal{U}_{11}$, coupled $\mathcal{U}_{22}$ - $\mathcal{U}_{33}$ and $\mathcal{U}_{44}$ electronic states. In order to reveal explicitly the impact of the nonadiabatic coupling on the nuclear dynamics in the $\mathcal{U}_{22}$ - $\mathcal{U}_{33}$ electronic states, we perform companion calculations for the photoelectron transitions to the uncoupled $\mathcal{U}_{22}$ and $\mathcal{U}_{33}$ electronic states also and the results are compared with those obtained in the coupled state simulations.

Since we start from an initial bound-state wave function, we calculate, $C(t) = \langle \chi^{k\star}(t/2) | \chi^k(t/2) \rangle$, which halves the total propagation time T needed to achieve the energy resolution, $\Delta \mathrm{E} = 2\pi\hbar/T$, in the photoelectron spectrum [188]. To reproduce the broadening of the spectrum due to limited energy resolution in the experiment and also due to three-body rotation, we damp the autocorre-

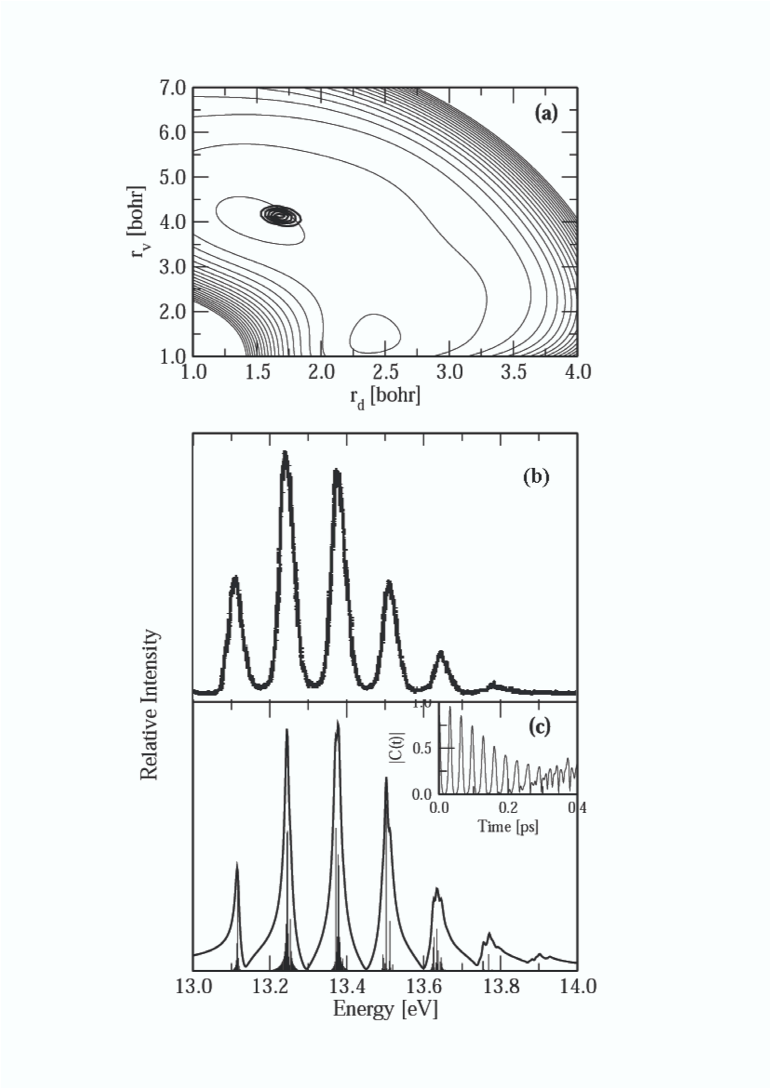

Figure A.1: The contour line diagram of the potential energy surface of the $\widetilde{X}\ ^2B_1$ electronic state of F_2O^+ in the r_d-r_v plane (panel *a*). The potential energies are obtained from Ref. [174]. The energy is measured relative to the minimum of the ground electronic state of F_2O. The minimum contour occurs at 0.5 eV and the spacing between the successive contour lines is 0.1 eV. The theoretical results on the first photoelectron band obtained by propagating the initial anharmonic wavefunction of the F_2O ground vibrational level of the ground electronic state (shown as dark solid contour lines in panel *a*) on the above electronic state is shown in panel *c* along with the available experimental results [174] in panel *b*. The variation of the absolute value of the time autocorrelation function is shown as an insert in panel *c*. Intensity in arbitrary units is plotted as a function of the ionization energy.

lation function with an exponential function, $f(t) = \exp(-t/\tau)$, before Fourier transformation. This is equivalent to convoluting a stick energy spectrum with a Lorentzian function with full width at the half maximum (FWHM) $\Gamma = 2\hbar/\tau$; τ being the relaxation time. In the following this width is chosen to best match the observed broadening of the experimental band.

A.4.1 The first photoelectron band

The potential energy surface of the $\widetilde{X}\ ^2B_1$ electronic state of F_2O^+ in the r_d-r_v plane is shown as a contour line diagram in Fig. A.1(a). Superimposed on it is the anharmonic initial wavefunction of the ground vibrational level of the ground electronic state of F_2O. It can be seen that the FC transition promotes the latter very near to the equilibrium geometry of the final state.

The theoretical results on the first photoelectron band is shown in Fig. A.1(c) along with the experimental results in panel (b). The WP is time evolved for a total of 1.1 ps. The variation of the absolute value of the time autocorrelation function is shown as an insert in panel (c). The autocorrelation function revels strong quasiperiodic recurrences in time, the average spacing between the successive recurrences is $\sim$ 32 fs which results into a spacing of $\sim$ 0.13 eV in the energy domain. The latter can be observed by inspecting the energy spectrum in Fig. A.1(c). The average splitting between the dominant peaks is $\sim$ 0.13 eV ($\sim$ 1048 cm^{-1}) to be compared with the experimental value of the symmetric stretch frequency ($\sim$ 1030 cm^{-1}) of F_2O^+ in the $\widetilde{X}\ ^2B_1$ electronic state [174]. This band do not reveal any progression along the bending mode at the resolution of the experiment. This fact is considered in the FC simulation of this band by Wang *et al.* [174] and their anharmonic model yielded results in good accord with the experiment. The present time-dependent WP results are also in very good

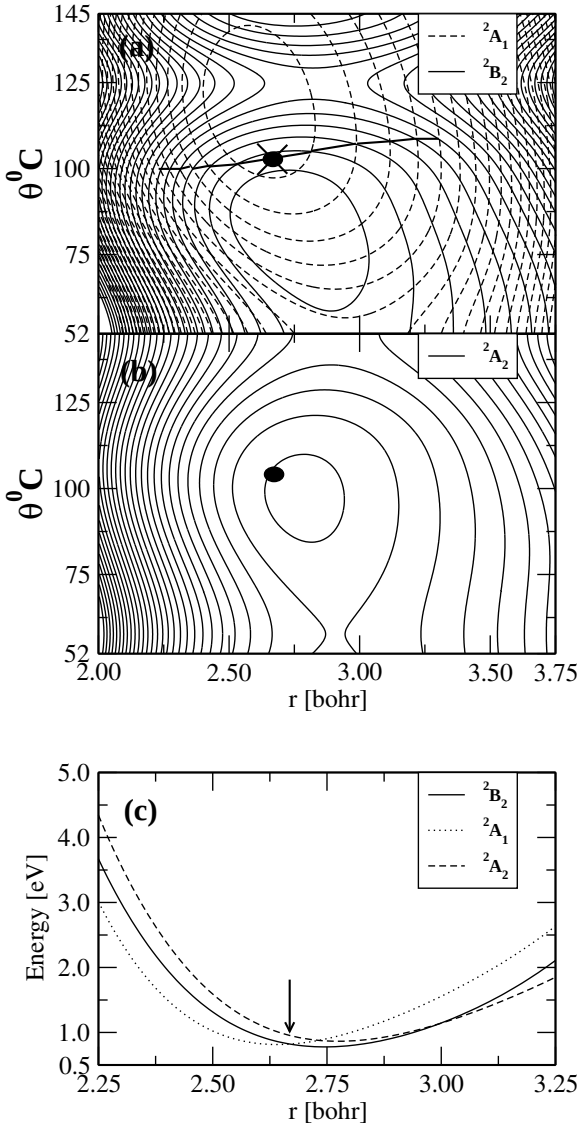

Figure A.2: Contour line drawing of the $\widetilde{A}\ ^2B_2$ -$\widetilde{B}\ ^2A_1$ and $\widetilde{C}\ ^2A_2$ (panel *a* and *b*) potential energy surfaces for C_{2v} geometries of F_2O^+. The spacing between the successive contour lines in 0.5 eV and the lowest energy contour occurs at 0.5 eV, 1.0 eV and $\sim$ 0.83 eV for the $\widetilde{A}\ ^2B_2$, $\widetilde{B}\ ^2A_1$ and $\widetilde{C}\ ^2A_2$ ionic states, respectively. The zero of the energy scale corresponds to the minimum of the $\widetilde{A}\ ^2B_2$ state of F_2O^+. The seam of conical intersections between the $\widetilde{A}\ ^2B_2$ and $\widetilde{B}\ ^2A_1$ electronic states is shown by the solid line in panel *a* and the cross on it indicates the energetic minimum of this seam. The heavy dots in panel *a* and *b* indicate the center of the FC zone in the photoionization to the respective state. One dimensional cuts of the $\widetilde{A}\ ^2B_2$, $\widetilde{B}\ ^2A_1$ and $\widetilde{C}\ ^2A_2$ electronic states through the minimum of the intersection seam of panel *a*, are plotted along the O-F bond distance and shown in panel *c*. The arrow in the panel points to the minimum of the seam of conical intersection between the $\widetilde{A}\ ^2B_2$ and $\widetilde{B}\ ^2A_1$ electronic states.

agreement at low energy resolution. The time autocorrelation function in Fig. A.1(c) is damped with a τ value of $\sim$ 263 fs (Γ = 5 meV) to generate the spectral envelope. The Fourier transformation of the autocorrelation function without damping is also included in the figure. It can be seen that each peak in the broad envelope splits under high resolution and we find even quantum progression along the bending vibrational mode of F_2O^+ corresponding to a frequency value $\sim$ 0.07 eV. The experimental value of the adiabatic ionization energy of the above band is $\sim$ 13.11 eV, this is reproduced well in the theoretical results.

A.4.2 The overlapping second, third and fourth photoelectron bands and the nonadiabatic effects

The $\widetilde{A}\ ^2B_2$ electronic state of F_2O^+ is energetically lower at the equilibrium configuration than the $\widetilde{B}\ ^2A_1$ state. The latter is in turn energetically lower than the $\widetilde{C}\ ^2A_2$ state at the equilibrium geometry. The minimum of the $\widetilde{A}\ ^2B_2$ state is $\sim$ 0.036 eV lower than that of the $\widetilde{B}\ ^2A_1$ state which is $\sim$ 0.05 eV lower than the $\widetilde{C}\ ^2A_2$ state. Therefore, it is clear that these states are very close in energy and the photoelectron bands arising from these three ionic states will be highly overlapping. In addition, the $\widetilde{A}\ ^2B_2$ and $\widetilde{B}\ ^2A_1$ ionic states can couple via the asymmetric stretching vibrational mode at sufficiently low energy.

The contour line diagram of the $\widetilde{A}\ ^2B_2$, $\widetilde{B}\ ^2A_1$ and $\widetilde{C}\ ^2A_2$ ionic states are shown in Figs. A.2(a-b), plotted in the (r-θ) plane to illustrate their topography for the C_{2v} geometrical arrangements of the nuclei. The potential energies are obtained from the *ab initio* potential energy function of Wang *et al.* [174]. The energies are measured relative to the minimum of the $\widetilde{A}\ ^2B_2$ electronic state. The $\widetilde{A}\ ^2B_2$ and $\widetilde{B}\ ^2A_1$ electronic states can cross each other at the C_{2v} geometrical arrangements in the space of the totally symmetric vibrational modes and from

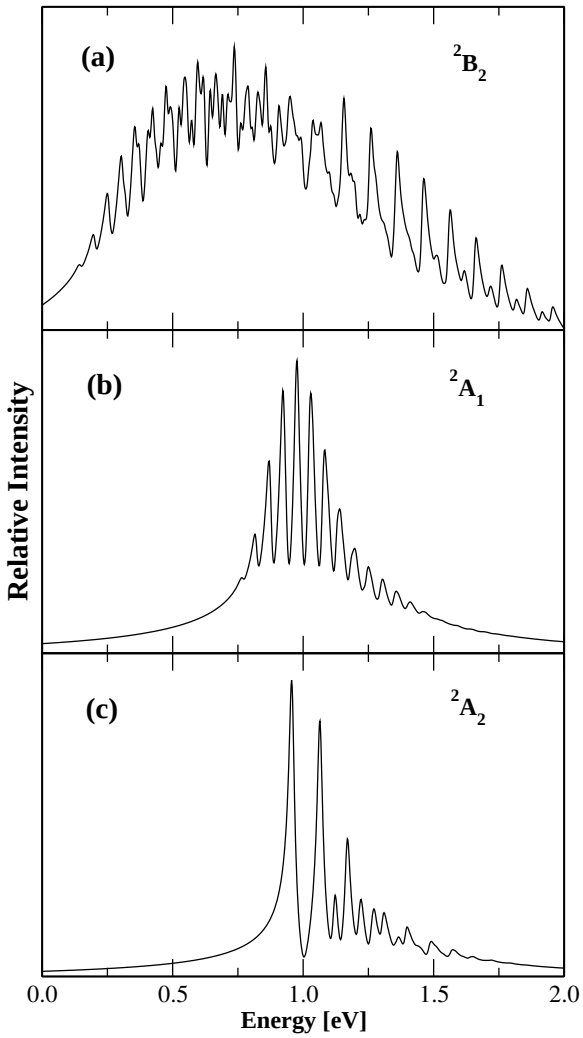

Figure A.3: The photoelectron spectrum for the uncoupled (a) $\widetilde{A}\ ^2B_2$, (b) $\widetilde{B}\ ^2A_1$ and (c) $\widetilde{C}\ ^2A_2$ electronic states of F_2O^+. The spectral intensity (in arbitrary units) is plotted as a function of the energy of the final electronic state. The spectra are obtained with the anharmonic initial wavefunction (cf. Fig. A.1(a)) of F_2O. The zero of the energy scale corresponds to the minimum of the $\widetilde{A}\ ^2B_2$ electronic state.

conical intersections. The seam of conical intersections of these states is shown by the solid line in Fig. A.2(a) and the cross on it indicate its energetic minimum occurring at $\sim$ 0.83 eV. The center of the FC zone in this coupled electronic manifold is shown by the dot in Fig. A.2(a) and also in Fig. A.2(b). It can be seen that the photoionization process prepares the WP almost on the intersection seam. Therefore, the latter is expected to be immediately perturbed by the associated nonadiabatic coupling effects. One dimensional cuts of the above electronic states through the minimum of the seam of the intersections of Fig. A.2(a) are plotted along the O-F distance in Fig. A.2(c). The minimum of the seam of intersections occurs at $r \sim 2.67\ a_0$ and $\theta \sim 102.69°$, and this minimum is relatively closer to the minimum of the $\widetilde{B}\ ^2A_1$ state occurring at $r \sim 2.62$ a_0 and $\theta \sim 119.5°$ [174]. Therefore, the effect of the nonadiabatic coupling on the nuclear dynamics of the latter state is expected to be stronger. The near degeneracy of the $\widetilde{C}\ ^2A_2$ state and $\widetilde{A}\ ^2B_2$ -$\widetilde{B}\ ^2A_1$ electronic states is also revealed in the figure.

In Figs. A.3(a-c) we show the photoelectron bands for the uncoupled $\widetilde{A}\ ^2B_2$, $\widetilde{B}\ ^2A_1$ and $\widetilde{C}\ ^2A_2$ electronic states of F_2O^+, respectively. The spectra are obtained by propagating the anharmonic initial wavefunction of F_2O ground state on the above cationic states. The time autocorrelation function in each case is damped with $\tau \sim 8.5$ fs to generate the broad band envelopes in Figs. A.3(a-c). We note that, we also carried out the time-independent matrix diagonalization calculations in order to unambiguously identify the progressions in the above three spectra. In this case however, a harmonic initial wavefunction is used. The theoretical data reveal an average spacing of $\sim$ 0.062 eV ($\sim$ 500 cm^{-1}) between the intense lines in the $\widetilde{A}\ ^2B_2$ band. This can be attributed to the progression along the bending vibrational mode of F_2O^+. We also note that the time-dependent

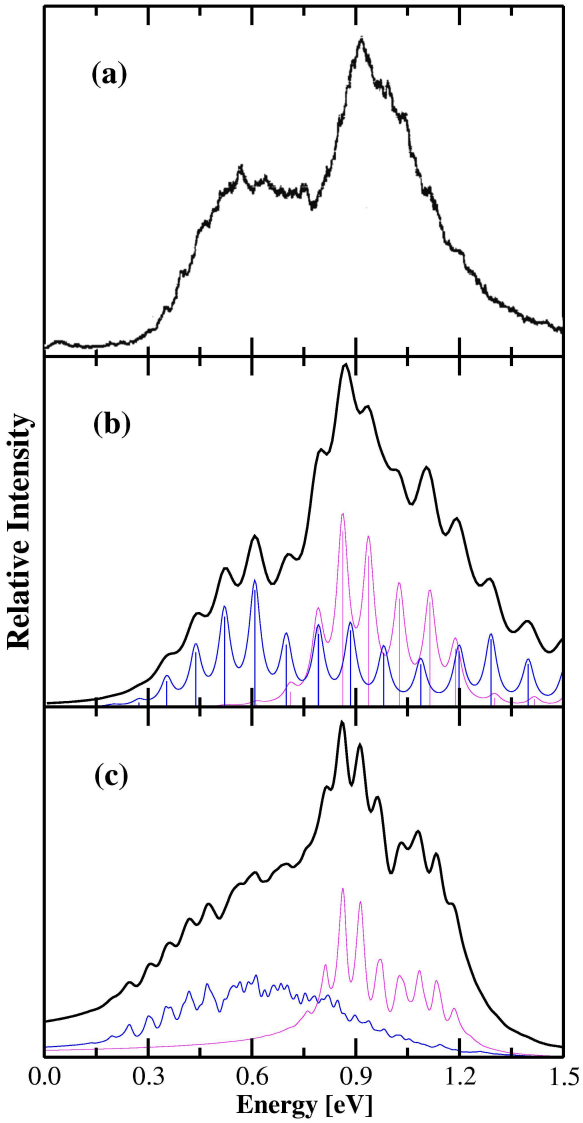

Figure A.4: The composite photoelectron spectrum of F_2O corresponding to a transition to the three excited electronic states $\widetilde{A}\,^2B_2$, $\widetilde{B}\,^2A_1$ and $\widetilde{C}\,^2A_2$ of F_2O^+. The relative intensity in arbitrary units is plotted as a function of the energy of the final vibronic state. The experimental spectrum reproduced from Ref. [174] is shown in panel *a*. The composite theoretical photoelectron spectrum obtained by the Lanczos diagonalization method and using a harmonic initial wave function of the F_2O ground state is shown in panel *b* as dark solid lines. Similarly, in panel *c*, the composite theoretical band obtained by propagating the anharmonic initial wave function is shown. The two spectra due to the $\widetilde{A}\,^2B_2$ (thick solid lines) and $\widetilde{B}\,^2A_1$ (thin solid lines) electronic states obtained in the coupled state situation are included in panels *b* and *c* under the theoretical composite band. The stick energy spectra obtained by the Lanczos diagonalization method are also included in panel *b*.

results in Fig. A.3(a) may also have finite background contributions arising from the direct dissociative component of the WP. A similar average energy spacing of ~ 0.063 eV corresponding to a progression along the bending vibrational mode is also found in the $\widetilde{B}\ ^2A_1$ band (cf. Fig. A.3(b)). Similar extended progression along the bending vibrational mode is observed in the corresponding photoelectron bands of Cl_2O [169]. The dominant lines in the $\widetilde{C}\ ^2A_2$ band in Fig. A.3(c), on the otherhand, are ~ 0.13 eV (~ 1048 cm^{-1}) spaced in energy which corresponds to the frequency of the symmetric stretching mode.

The final theoretical results (panel *b* and *c*) along with the experimental results (panel *a*) [174] are shown in Fig. A.4. First of all, the experimental band is highly diffuse and ionization to all three cationic electronic states contributes to the intensity of this band. Our theoretical results represent the full contribution from the $\widetilde{A}\ ^2B_2$ -$\widetilde{B}\ ^2A_1$ electronic manifold and $\sim 10\%$ contribution from the $\widetilde{C}\ ^2A_2$ electronic state to the overall spectral intensity. The composite photoelectron bands are shown by the thick solid lines in panel *b* and *c*. They are obtained by adding three spectra pertinent to the transitions to the above three cationic states. The results in panel *b* are obtained by the Lanczos diagonalization method using a harmonic initial wavefunction of the F_2O ground electronic state constructed in terms of dimensionless normal coordinates. The results in panel *c* on the other hand, are obtained by propagating the anharmonic initial WP on the final electronic states. The two spectra due to the $\widetilde{A}\ ^2B_2$ (thick solid lines) and $\widetilde{B}\ ^2A_1$ (thin solid lines) electronic states obtained in the coupled state situation are included in each panel under the theoretical composite band. In addition, the stick energy spectra obtained by the Lanczos diagonalization method are included in panel *b*. The composite theoretical envelopes are obtained by introducing a broadening by convoluting with a Lorentzian function with $\Gamma = 40$ meV. It can be

clearly seen that the $\widetilde{A}\,^2B_2$ state contributes to the low-energy maximum and the $\widetilde{B}\,^2A_1$ and $\widetilde{C}\,^2A_2$ states to the high-energy maximum of the observed bimodal intensity distribution in the experimental recording. The peaks in the coupled state spectra of the $\widetilde{A}\,^2B_2$ and $\widetilde{B}\,^2A_1$ electronic states are somewhat broader than that obtained in the uncoupled state situation (cf. Figs A.3(a) and 3(b), respectively). The band origin in the coupled state situation shifts by ~ 0.05 eV and ~ 0.001 eV to the higher energy compared to those in the uncoupled state situation for $\widetilde{A}\,^2B_2$ and $\widetilde{B}\,^2A_1$ electronic states, respectively. The broadening of the spectral peaks in the coupled state situation (in comparison to the uncoupled state results in Fig. A.3(a-b)) results from the nonadiabatic interactions between the two states.

The composite theoretical photoelectron bands in panels *b* and *c* contained $\sim$ 10% contribution from the $\widetilde{C}\,^2A_2$ state spectrum (cf. Fig. A.3(c)). We note that the heights of the two maxima in the theoretical band is adjusted empirically to fit with the experimental results. Such an adjustment was necessary as constant values of the transition dipole moment are assumed in the theoretical study. It is worth mentioning here that the nonadiabatic coupling strength in F_2O^+ is approximately two times larger than that found in Cl_2O^+ [169]. This is the reason that the experimental photoelectron band of Cl_2O has more resolved structures than F_2O. The increased value of the nonadiabatic coupling definitely contributes to the broadening of the bands, however, the resolution in the experimental recording also to be taken into account for the observed broadening.

The adiabatic ionization positions can not be identified unambiguously in the experimental recording, because of the highly overlapping nature of the composite band. Wang *et al.* [174] have predicted and adiabatic ionization energy of $\sim$ 15.71 eV for this composite band. In our calculation the first peak in the

$\widetilde{A}\ ^2B_2$ spectrum observed at $\sim$ 15.79 eV in the coupled state situation, when energy is measured relative to the minimum of this state. The minimum of the $\widetilde{A}\ ^2B_2$ state of F_2O^+ is $\sim$ 17.70 eV above to that of the ground electronic state of F_2O [174]. Therefore, the present theoretical results overestimates the adiabatic ionization position of the band and can be further improved by refining the energy at the global minimum of these electronic states. To this end we note that the agreement between the theoretical and experimental results are satisfactory within the mentioned approximations made in the theoretical treatment. The theoretical results may be further improved by carrying out full dimensional calculations of the potential energy surfaces, the electronic and relativistic spin-orbit coupling surfaces and the relevant transition dipole moment surfaces. This is beyond the scope of the present investigations and may be considered in a future study.

To this end we comment on the importance of the present full quantum dynamical treatment versus a similar approximate treatment within the harmonic picture. Our observations reveal that the anharmonicity of the initial state does not significantly alter the results as we start from its ground vibrational and rotational level. However, the anharmonicity of the final electronic state (particularly in the coupled state situation) is definitely more crucial for the observed asymmetry of the photoelectron band. Also, the broad and diffuse nature of the observed band implies a portion of the WP samples the dissociative region of the final electronic states (cf. Figs. A.6). The latter can not be described properly by a harmonic model. Therefore, it is very important to consider realistic *ab initio* model of the final electronic states and perform a full quantum dynamical treatment of the nuclear dynamics.

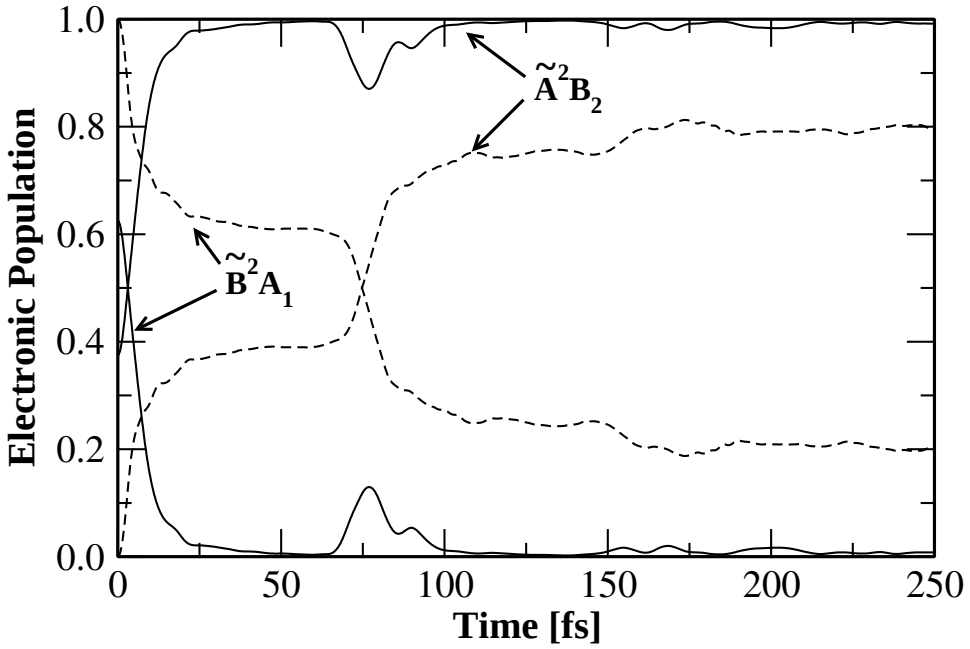

Figure A.5: The time dependence of the adiabatic (solid lines) and diabatic (dashed lines) electronic populations in the coupled state dynamics of the $\widetilde{A}\ ^2B_2$ -$\widetilde{B}\ ^2A_1$ electronic states corresponding to an initial FC transition to the $\widetilde{B}\ ^2A_1$ electronic state of F_2O^+.

A.4.3 Time-dependent dynamics in the $\widetilde{A}\,^2B_2$ -$\widetilde{B}\,^2A_1$ electronic states of F_2O^+

In order to enunciate the impact of nonadiabatic coupling on the WP dynamics we now report on the time dependence of the adiabatic and diabatic electronic populations in the $\widetilde{A}\,^2B_2$ -$\widetilde{B}\,^2A_1$ coupled electronic states of F_2O^+. These populations are calculated by defining adiabatic projectors in the diabatic electronic representation [**?**, 10]. The minimum of the $\widetilde{B}\,^2A_1$ electronic state is closer to the seam of conical intersections (cf. Fig. A.2(a)) and therefore, the dynamics of the initially prepared WP on this state is more strongly influenced by the nonadiabatic coupling compared to that on the $\widetilde{A}\,^2B_2$ state. An initial location of the WP on the latter diabatic state corresponds to 63% : 37% population of the component adiabatic states at t=0. In this case only $\sim$ 6% of the population moves to the $\widetilde{B}\,^2A_1$ diabatic state and the population dynamics does not reveal any characteristic feature and therefore, we do not show it here.

The population dynamics of the WP initially prepared on the $\widetilde{B}\,^2A_1$ diabatic electronic state, on the other hand, reveals interesting features and is shown in Fig. A.5. The adiabatic and diabatic electronic populations are shown by the solid and dashed lines, respectively. Since the WP is initially located on the $\widetilde{B}\,^2A_1$ diabatic electronic state, the population of this state is zero at t=0. This initial location also corresponds to 63% : 37% population of the component adiabatic states like in the $\widetilde{A}\,^2B_2$ case above. It can be seen that the $\widetilde{B}\,^2A_1$ diabatic electronic population starting from 1.0 at t=0 decays to $\sim$ 0.2 at longer times. The initial decay of the population relates to a decay time of $\sim$ 30 fs for this state. The population decays to $\sim$ 0.63 at $\sim$ 25 fs, therefore, within this time about 37% of the population moves to the $\widetilde{A}\,^2B_2$ diabatic state, population of this state

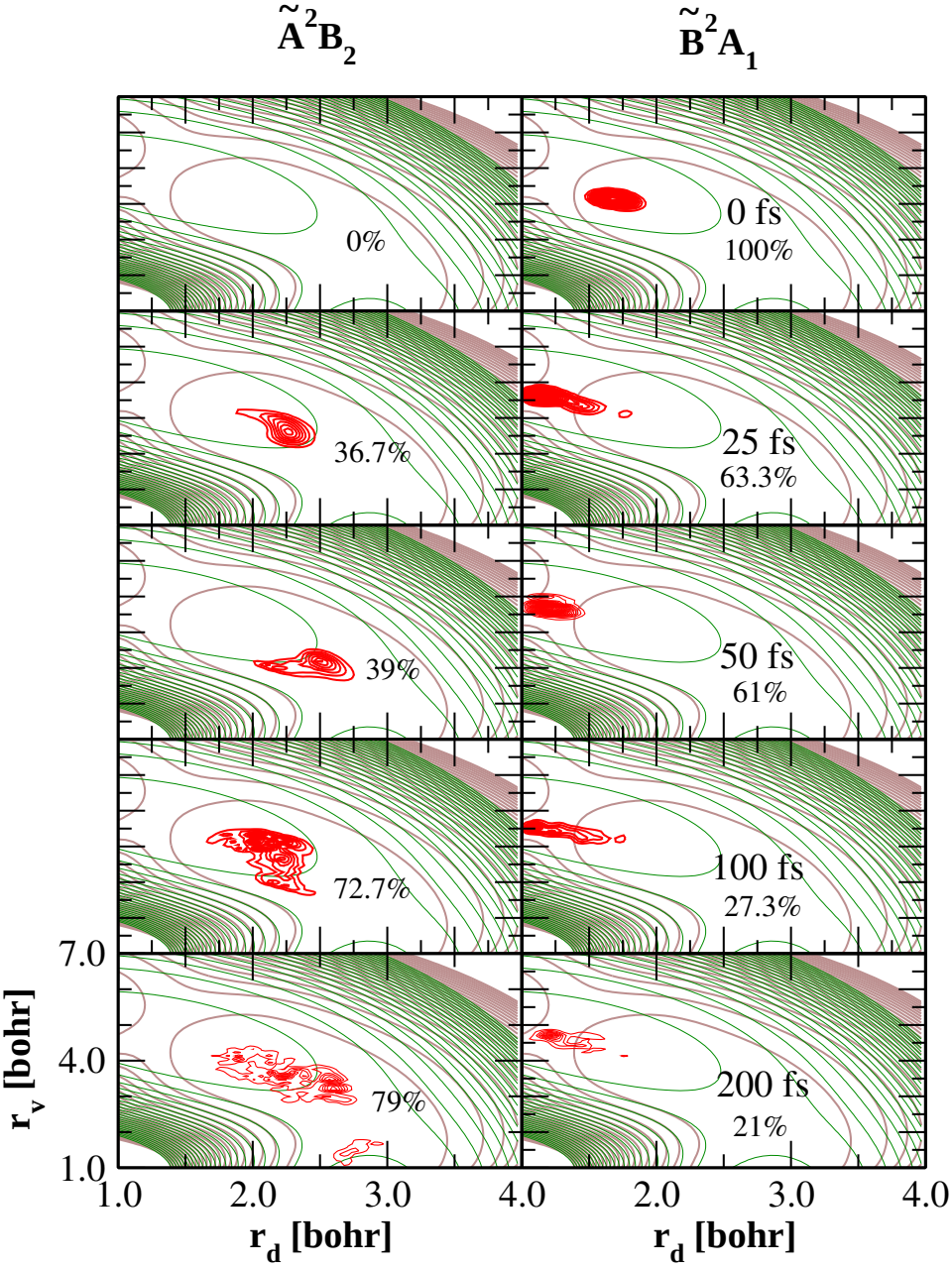

Figure A.6: Probability density ($|\chi^k|^2$) of the diabatic WP averaged over the angular coordinate and superimposed on the potential energy contours in the (r_d-r_v) plane for γ=$\pi/2$ in the coupled state dynamics of Fig. A.5. The WP components on the $\widetilde{A}\,^2B_2$ and $\widetilde{B}\,^2A_1$ electronic states at a given time (indicated in each panel) are shown in the left and right panels, respectively.

starts from zero at t=0. The population of both these states does not vary noticeably afterwards until $\sim$ 70 fs, when a second sharp drop in the $\widetilde{B}\ ^2A_1$ diabatic population takes place. Within about $\sim$ 100 fs $\sim$ 73% of the population reaches to the $\widetilde{A}\ ^2B_2$ diabatic state. The population of the two component adiabatic states reaches $\sim$ 100% : 0.0% at longer times. The weak recurrences seen in the adiabatic electronic populations are damped in the diabatic ones.

In order to better understand the above population dynamics we show snapshots of the wave packet evolving on the coupled $\widetilde{A}\ ^2B_2$ -$\widetilde{B}\ ^2A_1$ diabatic electronic states at different times in Figs. A.6. The contours of the probability density ($|\chi^k|^2$) of the WP averaged over the angular coordinate is superimposed on the potential energy contours for γ=$\pi/2$ in the r_d-r_v plane. It can be seen that the WP at t=0 is located very near to the equilibrium geometry of the $\widetilde{B}\ ^2A_1$ electronic state. The latter is found to be closer to the seam of $\widetilde{A}\ ^2B_2$ -$\widetilde{B}\ ^2A_1$ conical intersections (cf. Fig. A.2(a)). Because of this, the internal conversion to the $\widetilde{A}\ ^2B_2$ state takes place within a very short time. It can be seen that $\sim$ 37% of the WP moves to this state within $\sim$ 25 fs. The portion of the WP in the $\widetilde{A}\ ^2B_2$ state approaches towards the energetic minimum of this state (cf. snapshots at $\sim$ 50 fs) after arrival and mostly remain there at longer times. It appears that once the WP reaches the $\widetilde{A}\ ^2B_2$ state most of it does not recross the intersection seam and move to the $\widetilde{B}\ ^2A_1$ electronic state again. This is also indicated by the absence of quasiperiodic recurrences in the time dependence of the electronic populations (cf. Fig. A.6). At longer time ($\sim$ 200 fs) $\sim$ 79% of the WP moves to the $\widetilde{A}\ ^2B_2$ electronic state.

A.5 Summary

We have presented a theoretical account on the photoelectron spectroscopy of F_2O and compared our findings with the available experimental results. Particularly, the effects due to possible nonadiabatic interactions between the $\widetilde{A}\ ^2B_2$ and $\widetilde{B}\ ^2A_1$ electronic states of F_2O^+ on the photoelectron bands are examined in detail. The theoretical approach is based on the relevant *ab initio* potential energy surfaces of the system and time-independent and time-dependent quantum dynamical methods.

In this study the near equilibrium C_{2v} PESs reported by Wang *et al.* [174] for the F_2O ground and the low-lying excited electronic states of F_2O^+ are extended to the C_s geometries assuming a harmonic contribution from the asymmetric stretching vibrational mode. This is motivated by the fact that the excitation along this vibrational mode is not observed in the experimental data [174].

Analysis of the first photoelectron band revealed dominant progression along the symmetric stretch vibration. Weak excitations of the even quantum of bending vibration are also observed under high energy resolution. The broad band spectral envelope compares well with the experimental results. The second, third and fourth photoelectron bands are highly overlapping and are due to ionizations to the near degenerate $\widetilde{A}\ ^2B_2$, $\widetilde{B}\ ^2A_1$ and $\widetilde{C}\ ^2A_2$ electronic states of F_2O^+, respectively. The nonadiabatic interactions between the $\widetilde{A}\ ^2B_2$ and $\widetilde{B}\ ^2A_1$ ionic states are modeled here within a linear coupling scheme. These two ionic states can be coupled via the asymmetric stretching vibration. Conical intersections between these two states are established. The strength of the coupling parameter is derived from the *ab initio* electronic structure results. This resulted in the estimate 0.05 eV $\leq \lambda \leq$ 0.28 eV, with 0.18 eV as an average value of this quantity. The photoelectron bands due to $\widetilde{A}\ ^2B_2$ and $\widetilde{B}\ ^2A_1$ ionic states reveal extended

progression along the bending vibrational mode. The nonadiabatic interactions between these states contribute largely to the observed diffuse structure of the experimental band. The photoelectron band due to the $\widetilde{C}\ ^2A_2$ ionic state reveals dominant progression along the symmetric stretching vibration. The relativistic spin-orbit interactions of this state with the $\widetilde{B}\ ^2A_1$ ionic state is not considered in this study. We assumed $\sim 10\%$ contribution due to this state in the overall composite theoretical results presented here. The theoretical results are in good accord with the observed experimental results. Experimental results at higher energy resolutions are desirable to further refine the present theoretical model.

List of Publications

1. "A time-dependent wave packet study of the vibronic and spin-orbit interactions in the dynamics of $Cl(^2P) + H_2 \rightarrow HCl\ (X^1\Sigma_g^+) + H\ (^2S)$ reaction ", **S. Ghosal** and S. Mahapatra, J. Chem. Phys. **121**, 5740 (2004).

2. "Theoretical study of the Photodetachment spectrum of ClH_2^- ", **S. Ghosal** and S. Mahapatra, Chem. Phys. Lett. **394**, 207 (2004).

3. "A quantum wave packet dynamical study of the electronic and spin-orbit coupling effects on the resonances in $Cl(^2P) + H_2$ scattering ", **S. Ghosal** and S. Mahapatra, J. Phys. Chem. A **109**, 1530 (2005).

4. "A theoretical study of the electronic nonadiabatic transitions in the photoelectron spectroscopy of F_2O ", G. M. Krishanan, **S. Ghosal** and S. Mahapatra, J. Phys. Chem. A **110**, 1022 (2006).

5. "Nonadiabatic dissociation dynamics of Cl$\cdots$HD van der Waals complex initiated by electron detachment of $Cl^- \cdots HD$ ", **S. Ghosal** and S. Mahapatra, J. Photochem. Photobio. A - in press 2007.

6. "Nonadiabatic quantum wave packet dynamics of the $Cl(^2P)$ + HD reaction ", **S. Ghosal** and S. Mahapatra, (manuscript under preparation).

Posters/Paper/Oral Presentations in Symposia

1. Poster presented in "Trends in Theoretical Chemistry (TTC 2002)", January 17-19, 2003, Indian Association for the Cultivation of Science, Kolkata.

2. Poster presented in "6th National Symposium on Chemistry (VI NSC)", February 6-8, 2004, Indian Institute of Technology Kanpur, Kanpur.

3. Poster presented in "Symposium in Theoretical Chemistry (TCS 2004)", December 9-12, 2004, Bhabha Atomic Research Centre, Mumbai.

4. Poster presented in "Discussion Meeting for Advances in Spectroscopy (DMAS 2004)", February 21-24, 2005, Indian Institute of Science, Bangalore.

5. Poster presented in "Current Developments in Atomic, Molecular and Optical Physics with Applications (CDAMOP 2006)", March 21-23, 2006, Delhi University, New Delhi.

6. Poster presented in "Theoretical Chemistry Symposium (TCS 2006)", December 11-13, 2006, Bharathidasan University, Thiruchirappalli.

7. Poster presented in "Asian Spectroscopy Conference (ASC 2007)", January 29-2 February, 2007, Indian Institute of Science, Bangalore.

8. Posters presented in "Chemfest 2004, 2005, 2006 and 2007", School of Chemistry, University of Hyderabad, Hyderabad.

9. Paper presented in the Proceedings of the 2^{nd} international conference on Current Developments in Atomic, Molecular and Optical Physics with applications, "Time-dependent wave packet dynamics of the atom-diatom reactive scattering ", R. Padmanaban, **S. Ghosal**, B Jayachander Rao, and S. Mahapatra, Edited by Man Mohan (2006) - in press

10. Oral presentation in "Chemfest 2006",
    March 4, 2006, School of Chemistry, University of Hyderabad, Hyderabad.

Acknowledgments

My last remaining task is to acknowledge all those people who have helped me to complete this thesis.

I have been very fortunate with my supervisor Prof. Susanta Mahapatra. I met him quite unexpectedly and I must confess at this moment that I could not have found someone better for getting me through such a graduate experience. His unquenchable curiosity, hard work and love for the subject are probably the most valuable lessons I have learned from my PhD. I express my profound respect and deep sense of gratitude for his guidance and constant encouragements.

I would like to thank the former and present Deans, School of Chemistry and all other faculty members, non-teaching staffs of the school for their cooperation and assistance on various occasions. Special thanks to Prof. E. D. Jemmis for taking the initiative to provide a high-class computational facility in this campus under the University of Potential Excellence (UPE) and high performance computational facility (HPCF) programs. Financial assistance from the University of Grants Commission (UGC) is gratefully acknowledged. I also acknowledge the Volkswagen Foundation, Germany for the financial support in the beginning of my PhD carrier.

I thank my dear colleagues Dr. Padmanaban, Gireesh, Venkatesh and Jayachander for many stimulating discussions and help in various problems. I especially thank Padmanaban for his help in the initial days of my research. The work described in the Appendix was initiated by Gireesh, I convey him special thanks for this. I also thank my juniors Rajesh, Siva, Rakesh, Tanmoy and Susanta for maintaining a cheerful atmosphere in lab.

I must take this opportunity to thank all my teachers, especially Tamalda,

Pranabda, Bidhanda, Indrada and many more, whose inspiration and motivation has made it possible to finish my journey all the way from school to complete my PhD thesis.

Being away from home for so many days was a painful experience in the beginning. I must thank Mrs. Gitashree Mahapatra (madam) for providing me a homely feeling in several occasions. It is wonderful to see cute Anusha's dance on the stage and Anish to grow old enough to run in the ground! I also thank Somnathda for his generous invitations for homely dinners, his wife and son Megh to make me feel home in many weekends.

During my life as a PhD student I have been lucky enough to be surrounded by wonderful friends. I thank you **all** for helping me to get through the difficult times, for all the emotional support, entertainment, and the caring you have provided. Special thanks to the Spandan group: Abhik, Moloy, Saikat, Aniruddha, Taptakanchan, Arindam, Rahul and Abhinandan for allowing me to sing the songs of my sole.

Lastly, and most importantly, I thank all the members of my family for their unconditional support and encouragement. But for some people mere thanks is not enough. I dedicate this thesis to the most important people to me: My parents, kaku, chotoma, my sisters and my brother, Bibek. Unfortunately, My grand parents are not here to share this moment with me, but I am sure they keep an eye on me from heaven.

Subhas Ghosal